TWO-PHASE ANNULAR FLOW IN VERTICAL PIPES

BY

ERNEST ADAZE

A Thesis Presented to the
DEANSHIP OF GRADUATE STUDIES

KING FAHD UNIVERSITY OF PETROLEUM & MINERALS
DHAHRAN, SAUDI ARABIA

In Partial Fulfillment of the
Requirements for the Degree of

MASTER OF SCIENCE

In

MECHANICAL ENGINEERING

DECEMBER 2017

KING FAHD UNIVERSITY OF PETROLEUM & MINERALS
DHAHRAN- 31261, SAUDI ARABIA
DEANSHIP OF GRADUATE STUDIES

This thesis, written by **ERNEST ADAZE** under the direction of his thesis advisor and approved by his thesis committee, has been presented and accepted by the Dean of Graduate Studies, in partial fulfillment of the requirements for the degree of **MASTER OF SCIENCE IN MECHANICAL ENGINEERING.**

Hassan Badr
Dr. Hassan M. Badr
(Advisor)

Dr. Abdelsalam M. H. Alsarkhi
(Member)

R.B. Mansour
Dr. Rached B. Mansour
(Member)

Dr. Zuhair Gasem
Department Chairman

عن
Dr. Salam A. Zummo
Dean of Graduate Studies

01/02/2018
Date

To my parents, siblings and all my friends.

ACKNOWLEDGMENTS

My sincerest gratitude goes to the Almighty God for His divine protection, love and guidance throughout my stay at King Fahd University of Petroleum and Minerals (KFUPM). All praise be unto His Holy Name.

Special thanks to my thesis advisor, Dr. Hassan M. Badr whose door was always opened to me whenever I encountered a problem, being it academic or personal. You were more than an advisor to me; a great father. I promise to make you proud in the next stage of my life. God continue to bless you and your family.

To my thesis committee members, Dr. Abdelsalam Alsarkhi and Dr. Rached Ben Mansour, I say a very big thank you to you for your passionate participation and contribution in this thesis. I really appreciate Dr. Alsarkhi for the time you spent with me during the summer vacation, increasing my understanding of multiphase flows and providing me with the necessary data to validate my model, and to Dr. Rached for increasing my knowledge in Computational Fluid Dynamics (CFD). I will forever remain grateful to you all.

A big thank you to the officials at the Ministry of Higher Education in the Kingdom of Saudi Arabia for granting me the opportunity to undertake my MS

study in Mechanical Engineering through the Deanship of Graduate Studies and the Department of Mechanical Engineering in one of the great universities in the world.

My appreciation to all my colleague graduate students, especially Mr. Ibrahim Balarabe Mansir, Mr. Haxia Li and Mr. Aliyu Mansur whom I spent nights at the computational laboratory with, trying so hard to get some of the models right. You all made the use of the computational software interesting.

To the Ghanaian community, especially Dr. Ben Issaka, Mr. Najmudeen Sibaweihi, Mr. Musah Ahmed Rufai Muhyedeen, Mr. Ankah Nestor, Mr. Malik Karim, Mr. Kamarudeen Wahid Mende, Mr. Richard Osei-Aning, Mr. Mathew Amoh, Mr. Farouk Awal, Mr. Ibrahim Swini, Mr. Ramadan Abubakar Rashid, Mr. Ishak Mohammed, Mr. Rashid Bawah, Mr. Samuel Opoku Agyemang and Mr. Lionel Fogang, I say thank you for the support and encouragement.

I specially thank my parents, siblings and loved ones for their unconditional love, support and prayers throughout my entire masters degree (MS) programme. You made this achievement possible.

God bless you all and remember you for good.

TABLE OF CONTENTS

LIST OF TABLES

LIST OF FIGURES

THESIS ABSTRACT

NAME: Ernest Adaze
TITLE OF STUDY: Two-Phase Annular Flow in Vertical Pipes
MAJOR FIELD: Mechanical Engineering
DATE OF DEGREE: December 2017

Two-phase gas-liquid flow in vertical pipes has been one of the important research areas because of the related industrial applications in power plants, nuclear reactors, steam generators, gas well exploration and others. The variety of two-phase flow patterns in pipes of different inclinations makes it difficult for obtaining analytical or numerical solutions that are applicable to a wide range of gas void fractions (GVF). Among the problems usually encountered in gas production is the presence of a small percentage of liquid forming an annular flow pattern in which the liquid occupies the pipe wall region while the gas flows at higher speed in the pipe core region carrying some entrained liquid droplets. In this flow field, the gas phase is driven by the pressure gradient along the pipe while the liquid is driven by the shear force acting at the liquid-gas interface. When the gas velocity decreases, the liquid film will start falling down causing a problem known as "liquid loading". This is a two-phase phenomenon where, the energy needed to transport the liquid phase (entrained droplets and liquid film) out of the gas well is insufficient and as such causes the liquid to fall and accumulate at the bottom of the gas well. This problem, when allowed to prolong, might "kill" the gas well and cease production. This thesis aims at applying CFD techniques to predict the beginning of liquid film reversal in a vertical pipe of diameter 76.2 mm by performing a 2D axisymmetric numerical simulations using ANSYS Fluent® version 16.1 commercial software to predict the onset of film reversal so as to allow necessary measures be taken to mitigate the problem. The geometry and mesh were however developed in Gambit software. The mesh was made very fine at the liquid film region close to the pipe wall and coarser toward the pipe centre with a transition rate of 15% and an aspect ratio of less than 4. The governing equations were solved using the hybrid model (Eulerian Multi-Fluid VOF). Other models considered in the current study include: continuum surface force for the effects of surface tension, standard $k - \varepsilon$ turbulence model with enhanced wall treatment for turbulence effects, modified HRIC scheme for tracking the interface between the phases and Schiller and Naumann's model for the drag modeling. All the transport and conservations equations were discretized accurately using the finite-volume method and solutions were considered to be converged when all the residuals were less than 10^{-3} with mass imbalances less than 5%. Simulations are made using air and water at 1 atm as the main working fluids in a 3-m long pipe. The pressure gradients and critical superficial gas velocities predicted by this model agreed well when compared with experimental results. The critical superficial gas velocities are found to decrease with the superficial liquid inlet velocity. In addition, the shear stress is found to fluctuate with high amplitudes in the vicinity of the pipe wall where the liquid phase dominates and gradually reduces towards the pipe centerline. Slip between the phases can be ignored in the gas core regions where high gas velocities exist. Detailed information regarding the formation of roller waves was, however, limited due to the adoption of the 2D computational domain. It is therefore recommended that a 3D domain be utilized to improve the visualization and understanding of the roll and disturbance wave formations in the flow domain.

ملخص الرسالة

الاسم الكامل: ارنست اداز

عنوان الرسالة: السريان ثنائي الطور في الأنابيب الرأسية

التخصص: الهندسة الميكانيكية

تاريخ الدرجة العلمية: ديسمبر 2017

يعتبر سريان الموائع (السوائل والغازات) في الأنابيب الرأسية غاية في الأهمية نسبة لإرتباطة العميق بمختلف التطبيقات الصناعية كمحطات القدرة و المفاعلات النووية ومولدات الغاز والصناعات البترولية. أنماط السريان داخل الأنابيب تختلف بأختلاف زوايا ميلان الأنابيب التي تؤدي إلي تعقيد الحل التحليلي والعددي المطبق على كسور فراغ الغازي. من ضمن المشاكل المتعلقة بإنتاج الغاز ظهور دوامات دائرية صغيرة من الطور السائل تغطي الجدار الداخلي للأنبوب بالتزامن مع سريان الغاز بالسرعة القصوي في منتصف الأنبوب حاملا معه قطرات من السائل. في هذا النوع من السريان متعدد الأطوار, سريان الغاز مدفوع بواسطة فرق الضغط بينما سريان السائل محكوم بتغير قوى القص المؤثرة على منطقة التداخل بين السائل والغاز. إنخفاض سرعة الغاز تؤدي إلي هبوط طبقة السائل إلي أسفل الأنبوب وينتج عنها مشكلة تراكم السائل. هذة الظاهرة تحدث في السريان متعدد الأطوار عندما تكون الطاقة المتطلبة لنقل الطور السائل غير كافية وتؤدي إلي تراكم السائل في قاع بئر الغاز, و تؤثر بشكل مباشر على بئر الغاز و قد تؤدي إلي وقف الإنتاج. في هذة الأطروحة, تم إستخدام ديناميكا الموائع الحسابية (CFD) للتنبؤ ببداية إرتداد طبقة السائل في الأنبوب الرأسي ذو القطر 76.2 ملم عن طريق الحل العددي ثنائي الأبعاد المتماثل حول المحور الرأسي للأنبوب بإستخدام برنامج (ANSYS Fluent). تم تصميم شبكة ومجال الحل بواسطة برنامج قامبيت. صممت شبكة الحل بالقرب من جدار الحل الأنبوب دقيقية جدا وتقل الدقة بإتجاه منتصف الأنبوب بمعدل 15% وبنسبة متزنة أقل من 4. ووجد الحل للمعادلات الحاكمة عن طريق نموزج حل هجين. النمازج الأخري التي تم إعتبارها في هذه الدراسة هي قوى السطح المستمر لأثار التوتر السطحي و معيار $k - \varepsilon$ للسريان المضطرب مع تعديل الجدار لتخفيف أثار الإضطراب ونموزج HRIC لتعقب التداخل بين أطوار السريان ونموزج Schiller-Naumann لنمزجة الأعاقة. جميع معادلات حفظ وتحويل الطاقة فصلت بدقة بإستخدام طريقة الحجم المحدود وتم أعتبار تقارب الحل عندما تكون قيمة المتبقي أقل من 0.001 و إختلال توازن الكتلة أقل من 5%. تمت النمزجة بإستخدام الماء والهواء عند ضغط جوي يساوي واحد جو التي تسري داخل أنبوب بطول ثلاثة أمتار. تم حساب تغير الضغط والسرعة السطحية الحرجة للغاز. أظهرت النتائج تماثل كبير مع نتائج التجارب المعملية. وجد أن سرعة الغاز السطحي تنخفض مع إنخفاض سرعة دخول السائل للأنبوب. بالإضافة إلي ذلك, وجد أن قوى القص تتغير بقيمة عالية مع محيط الجدار الداخلي للأنبوب نسبة لوجود الطور السائل بشكل أكبر والذي ينخفض تدريجيا بإتجاه مركز الأنبوب. الإنزلاق بين أطوار المائع (السائل/ الغاز) يمكن

تجاهله خاصة في مناطق الغاز الاساسية عند سريان الغاز بالسرعة العالية. المعلومات التفصيلية المتوفرة عن تكون الموجات الدوامية قليلة نسبة لإستخدام المجال الحسابي ثنائي الأبعاد, لذلك يوصى بإستخدام المجال الحسابي ثلاثي الأبعاد لتحسين الحل وتعميق فهم موجات الإضطراب المتكونة في مجال السريان.

CHAPTER 1

INTRODUCTION

1.1 Background of Multiphase Flows

Multiphase flows is a term describing the flow of two or more immiscible fluids in a flow passage (e.g. oil and water flow in a pipeline) or two phases of the same fluid (e.g. water and steam in boiler tubes). The presence of solid particles in a given fluid may also be considered as a third phase. The occurrence of multiphase flow in many industrial applications created the need for a thorough understanding of the structure of such flow and also for developing methodologies for prediction of its main characteristics. In this type of flow, the interface that exists between the phases is highly induced by the motion of the participating phases. Multiphase flow frequently occurs in chemical, nuclear, mining and petroleum industries. For example, in oil production facilities, the crude oil produced from oil wells is normally accompanied with water, gases and sand forming a four-phase flow. The structure of such flow depends on the percentage and properties of each phase, the geometry of the flow passage and the flow rate.

1.2 Classification of Multiphase Flows

Multiphase flows can generally be classified under two main headings, namely, phase combinations and interfacial structure (flow regime or flow pattern). Under phase combinations, the number of the participating phases or components is used to describe the type of multiphase flow phenomenon. Hence, the flow can be described as two-phase (e.g. liquid-gas, solid-gas, solid-liquid, etc.), three-phase (e.g. solid-liquid-gas) or four-phase flow (e.g. oil-water-gas-solid).The interfacial structure developed as a result of the different flow rates of the participating phases in the flow can be used to classify the type of multiphase flow phenomena. As a result of the different flow rates of the phases involved, there exist interfaces between the phases which lead to the internal phase distributions known as flow regimes or flow patterns. Under this category, multiphase flow can be classified as dispersed flow (bubbly flow), intermittent flow (slug) or annular flow. Figure 1.1 gives a summary of multiphase flow classification. This study focuses on two-phase flow and as such much more details about this type of flow will be considered in the subsequent sections.

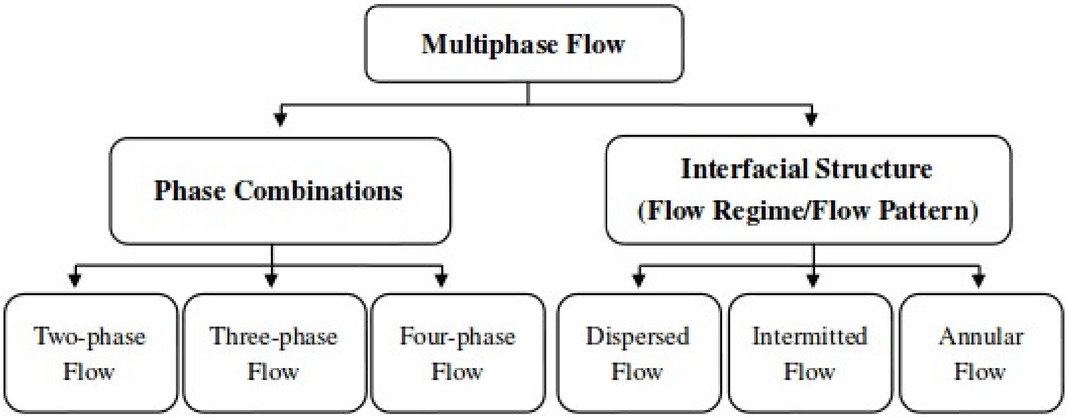

Figure 1.1: Classification of multiphase flows

1.3 Types of Two-Phase Flows

Two-Phase Flow (gas-liquid) in vertical pipes has been one of the interests of industrial applications such as power plants, nuclear reactors, boilers, gas production and others. There are several flow regimes or patterns encountered in vertical flows as a result of geometric distribution of the components within the flow field[1]. This geometric distribution affects the mass, momentum and energy transfer rates of the two phases. The well-known flow pattern presented by flow through vertical pipes, as shown in Figure 1.2, include, bubbly, slug or plug, churn, annular and wispy-annular flow[2]. These flow patterns are observed with increasing gas flow rate.

In bubbly flow, as shown in Figure 1.2a, several bubbles are seen dispersed in a continuous liquid phase as discrete bubbles with varying size and shape. The bubbles are almost spherical and with diameters much smaller than that of the pipe.

Increasing the gas void fraction causes the bubbles to collide and coalesce to generate larger bubbles often in the shape of a bullet (Taylor bubbles) flowing upward as can be seen in Figure 1.2b[3]. This flow configuration is known as slug flow. The Taylor bubbles are usually separated by liquid slugs which might contain some small bubbles. The bubble dimensions are almost of the same size as the pipe diameter. There is a thin liquid film between the Taylor bubbles and the pipe wall, which, under the influence of gravity, may flow downward.

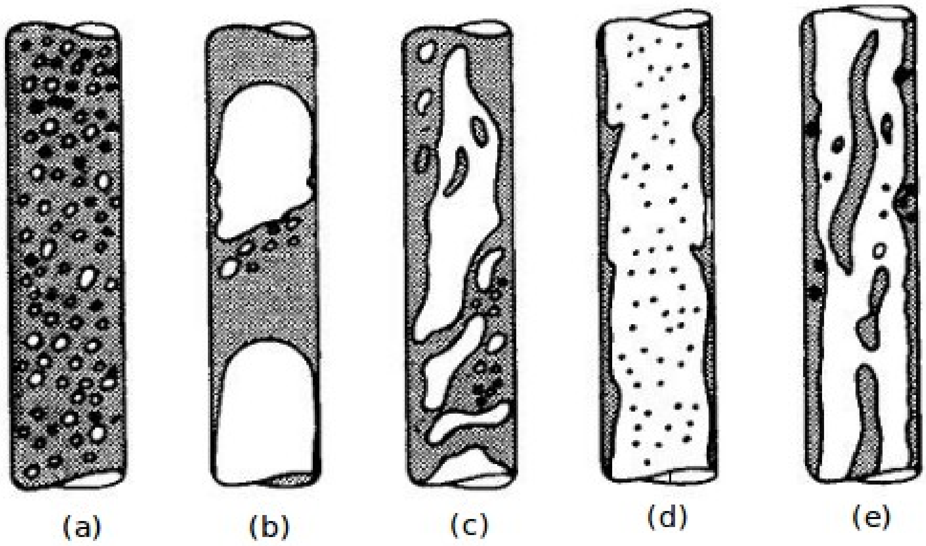

Figure 1.2: Flow regimes in vertical upward two-phase flow a) Bubbly, b) Slug, c) Churn, d) Annular and e) Wispy[2]

Churn flow is an intermediate regime observed between slug flow and annular flow regimes. As the gas superficial velocity is further increased, the flow becomes very unstable due to the breaking up of the slug bubbles leading to oscillatory action as can be observed in Figure 1.2c. The liquid phase tends to experience an intermittent up and down flow (though there is a net upward flow) due to the relative balance between shear and gravity forces acting in opposing direction.

Annular flow as shown in Figure 1.2d, presents a flow pattern with a liquid film on the pipe walls while the gas flows as a continuous stream in the pipe core region. Thus, the liquid film forms an annular ring round the gas stream. This flow pattern occurs because of further increasing the gas flow rate. There might be gas bubbles contained in the liquid film. Similarly, the gas stream might or might not contain entrained droplets of liquid[3]. Since this type of flow pattern or regime occurs mostly in pipe flow involving two phases, it is the focus of this study and will be considered much more in the subsequent sections. A further increase in the flow rate causes the entrained droplets in the gas phase to increase. Hence, they merge to form large lumps or "wisps" of liquid in the gas core, see Figure 1.2e.

1.3.1 Main Features of Annular Flow

This flow pattern is common in industrial applications such as power plants, nuclear reactors, boilers, gas well exploration and others. It is characterized by a high gas core flow rate surrounded by an annular ring of liquid phase on the pipe periphery. When both phases are flowing in the same direction, the flow is called cocurrent while when both phases flow in opposite directions, the flow is said to be countercurrent. In horizontal pipes, the liquid film at the bottom pipe is much thicker than the upper pipe wall. This is usually due to the gravitational effect which causes the constant drainage of the film from the upper section of the pipe surface to the lower side. As the pipe inclination is increased towards the vertical position, similar liquid film distribution, as observed in the horizontal pipe, is noticed with the exception that the bottom pipe liquid film thickness is gradually reduced. In the vertical orientation, the liquid film distribution tends to be axisymmetric with equal film thickness around the pipe periphery. The gas core in most cases contains droplets of liquids usually entrained from the liquid film on the pipe wall due to the shearing effect caused by the high-speed gas phase at the interface. The liquid film on the other hand, may also contain some gas bubbles. This usually occurs as a result of some bubbles being captured by the breakdown of the waves that are just in front of the large roll waves[4].

The understanding of the flow physics underlying the wavy interface that exist between the liquid film and the gas core is of great interest in that it is the main source of droplet entrainment into the gas core. Furthermore, the lateral force needed to maintain the liquid film on the tube walls and the turbulence flow structures found within the gas and the liquid phases which influence the drop in pressure could all be analyzed through the dynamics of the wavy interface that exists between the liquid film and the gas core[4]. The fundamental understanding of the physics regarding the interfacial processes is limited because of the complexity in acquiring comprehensive local data from experiments. However, as a result of technological advancement and availability of computing resources, computational fluid dynamics techniques can be utilized to gain more insight into the physical phenomenon of annular flow and produce enough numerical data for scientific advancement.

1.4 The Concept of Flow Reversal in Vertical Pipes

In two-phase (liquid-gas) cocurrent upward annular flow in vertical pipes, with high gas flow rate, the liquid phase being the film or droplets moves upward. However, if the gas flow rate is reduced below a certain threshold (critical value), the energy required to create the upward movement of the liquid phase decreases and as a result, the liquid phase reverses direction and fall back to the bottom of the pipe, a condition known as flow reversal. For flows in larger pipe diameters where droplet entrainment is significant, this condition initially occurs in the liquid film as observed by Westende[5]. Hewitt *et al.*[6] also observed that the flow reversal is characterized by regions of falling liquid film between large upward moving waves. The point of flow reversal is usually associated with the point of minimum pressure drop in upward gas-liquid flow and is usually adopted as a criterion to correlate the transition from annular flow to churn flow in terms of the superficial gas velocity[7].

In the course of gas production, both liquid and gas are produced initially and carried to the ground surface. This happens if the gas flow velocity is high enough to drag the liquid film and entrain the liquid droplets to the surface. But once the gas flow velocity falls (which is usually the case due the well ageing) below a critical value, the liquid phase tends to fall back into the wellbore and accumulate, a condition known as liquid loading. This accumulated liquid tends to produce an additional hydrostatic back pressure that limits the gas flow from the well. This usually happens in the life cycle of the gas well and very common in aged gas fields[8]. This problem, when allowed to prolong might "kill" the gas well and cease production. Liquid loading has become a major problem associated with gas production.

A good prediction of flow reversal (which may lead to liquid loading) together with appropriate and timely application of gas well deliquification measures, significantly, improves the production of a gas well.

1.5 Thesis Outline

This thesis is made up of five chapters. It is aimed at developing a numerical model for two-phase annular flow in a vertical pipe. The model is further used to investigate the onset of liquid film reversal in a vertical pipe.

Chapter 1 provides a general overview of multiphase flows in terms of their classifications. Also discussed in this chapter are the types of two-phase flows in vertical pipes. A more detailed view of annular flow and its features are also included. The chapter ends with a discussion on the concept of flow reversal in vertical pipes.

Chapter 2 starts with definitions of basic terminologies commonly encountered in two-phase flow studies. It discusses earlier studies conducted on two-phase annular flow and flow reversal in vertical pipes as well as the common closure models used for annular flow. Included in this section are the various experimental and numerical studies conducted in the research area.

Chapter 3 presents the problem definition and method of solution. This section is divided into three parts. The first part, which happens to be the problem definition, includes the statement of problem and the objectives of the research. The second part covers the governing equations and model assumptions. The third part of this section is the method of solution which discusses the discretization of the governing equations, the computational domain and mesh, the initial and boundary conditions, the phase materials utilized, the test matrix and the solution algorithm.

Chapter 4 includes the model validation, results and discussions. This section is divided into three parts. The first part presents the mesh and time step independency tests, and the validation of the model with experimental data. The second part discusses the estimation of the critical superficial gas velocities corresponding to film reversal and presents the flow field observed in the simulation, effects of the superficial velocities on the main features of flow and the final part presents the velocity and shear stress distributions in the flow.

Chapter 5 gives the conclusion of this study and suggests recommendations for potential further studies.

CHAPTER 2

LITERATURE REVIEW

2.1 Introduction

In this chapter, earlier studies in annular flow, churn flow and liquid loading phenomena as well as the commonly adopted numerical methodologies are presented. To further enhance understand the content of this thesis, basic terminologies are first defined and briefly explained.

2.2 Basic Terminologies

Some of the fundamentals of two-phase flow such as superficial velocities, flow regimes, pressure gradient, liquid holdup and entrainment fraction are briefly explained below to provide a clear understanding of this study.

2.2.1 Superficial Velocity

The superficial velocity of any given phase i, is a hypothetical flow velocity calculated as if the given phase is the only one flowing or present in a given cross section. Mathematically, it is defined as the ratio of the volumetric flow rate of the phase to the total cross-sectional area of the pipe as in equation (2.1).

$$U_i = \frac{q_i}{A} \tag{2.1}$$

where U_i is the velocity of phase i; q_i is the volumetric flow rate of phase i and A is the total cross-sectional area of the pipe.

2.2.2 Flow Regime or Flow Pattern Map

Flow regime is term used to describe the characteristic distributions of the fluid-fluid interface[3]. The flow regime is usually obtained or predicted from independent variables of the system such as the phase physical properties and flow rates. Flow regimes are usually presented on flow pattern maps. For a vertical pipe, the flow regimes include bubbly flow, slug flow, churn flow and annular flow. Shown in Figure 2.1 are examples of flow pattern maps for both vertical and horizontal pipes using superficial velocities.

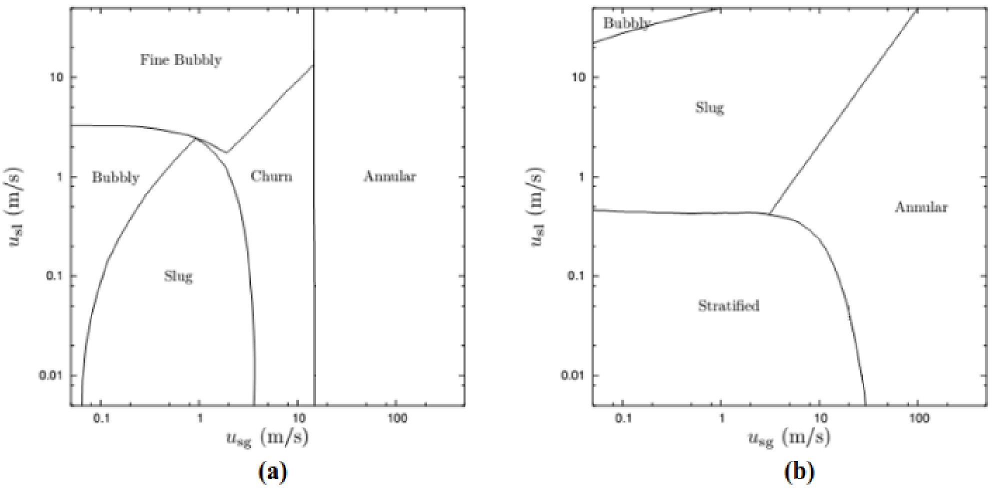

Figure 2.1: Examples of flow pattern maps for a) vertical upward flow and b) horizontal flow[9]

2.2.3 Pressure Gradient

The pressure drop per unit length of a pipe is the pressure gradient. For two-phase flows, the total pressure gradient, $-\frac{dp}{dL})$ is usually given as the sum of three main components, namely: the frictional term (f), the gravitational term (g) and the acceleration term (acc) as given in equation (2.2).

$$-\frac{dp}{dL}\Bigg) = -\left[\frac{dp}{dL}\Bigg)_f + \frac{dp}{dL}\Bigg)_g + \frac{dp}{dL}\Bigg)_{acc}\right] \tag{2.2}$$

2.2.4 Liquid Holdup

The liquid holdup sometimes called the liquid fraction is general term used to describe the volume fraction of liquid in a given pipe segment. It can be expressed in term of the void fraction, α, which is defined as:

$$\alpha = \frac{V_G}{V} \tag{2.3}$$

where V_G represents the volume of gas in a given segment of the pipe and V is the total volume of the pipe segment. In terms of the void fraction, the holdup, H_L is expressed as:

$$H_L = 1 - \alpha = \frac{V_L}{V} \tag{2.4}$$

where V_L represents the volume of liquid in the given pipe segment.

2.2.5 Entrainment Fraction

This is the term used to describe the fraction of the liquid flow rate which is entrained as droplets into the gas core. Mathematically, it is expressed as:

$$f_E = \frac{\dot{m}_{droplets}}{\dot{m}_L} = 1 - \frac{\dot{m}_{LF}}{\dot{m}_L} \tag{2.5}$$

where f_E is the entrainment fraction; $\dot{m}_{droplets}$ is the mass flow rate entrained as droplets; $\dot{m}_{LF}$ is the mass flow rate of the liquid film and $\dot{m}_L$ is the input liquid mass flowrate.

2.2.6 Froude Number

This is a dimensionless variable defined as the ratio of the inertial forces on an element to the weight of the fluid element. For two-phase flow, Wallis[10] proposed these two equations for the Froude number (also know as the modified Froude number):

$$Fr_G = \frac{\rho_G {U_G}^2}{gD(\rho_L - \rho_G)} \tag{2.6}$$

$$Fr_L = \frac{\rho_L {U_L}^2}{gD(\rho_L - \rho_G)} \tag{2.7}$$

where U_G is the gas velocity; ρ_G is the gas density; ρ_L is the liquid density; and D is the tube diameter. Fr_G can be used to predict the transition from annular flow to churn flow and vice versa[3]. Experimental studies show that transition occurs when $Fr_G \approx 1$[11].

Since flow reversal involves a transition from annular flow to churn flow[3], the next section presents a detailed description and the differences between annular and churn flows. This study focuses on flows in vertical pipes, hence annular and churn flows in vertical pipes are presented.

2.3 Annular and Churn Flows in Vertical Pipes

As described in the previous chapter, annular flow in vertical pipes features a high-speed gas core with entrained liquid droplets surrounded by a ring of liquid film around the pipe periphery. The liquid film is usually uniformly distributed around the pipe periphery in vertical pipe flows and may contain some gas bubbles. The drag force of the high-velocity gas flow generates waves on the liquid film which becomes the main source of the entrained liquid droplets in the gas core. These entrained droplets are occasionally re-deposited in the liquid film downstream as they move randomly in the gas core and are conveyed upward by the gas phase[3].

On the other hand, churn flow is a chaotic flow regime which makes it very difficult for investigators to model its physics and as such is usually described experimentally due to the complexity of the flow regime[12][13]. Similar to annular flow, churn flow presents a liquid film on the pipe wall except that the liquid film flows in an oscillatory manner, upward and downward, due to the gas velocity which is comparatively lower than that needed to convey the liquid film continuously upward[14]. As result of the drag force exerted by the upward movement of the gas phase at a velocity higher than the net-upward liquid film velocity, large waves are typically created on the liquid film. These large waves usually end up breaking up and entrained as liquid droplets or lumps. Shown in Figure 2.2 are the schematic diagrams for both annular and churn flows.

The next section presents the numerical studies conducted on annular and churn flows. The focus is on vertical pipes.

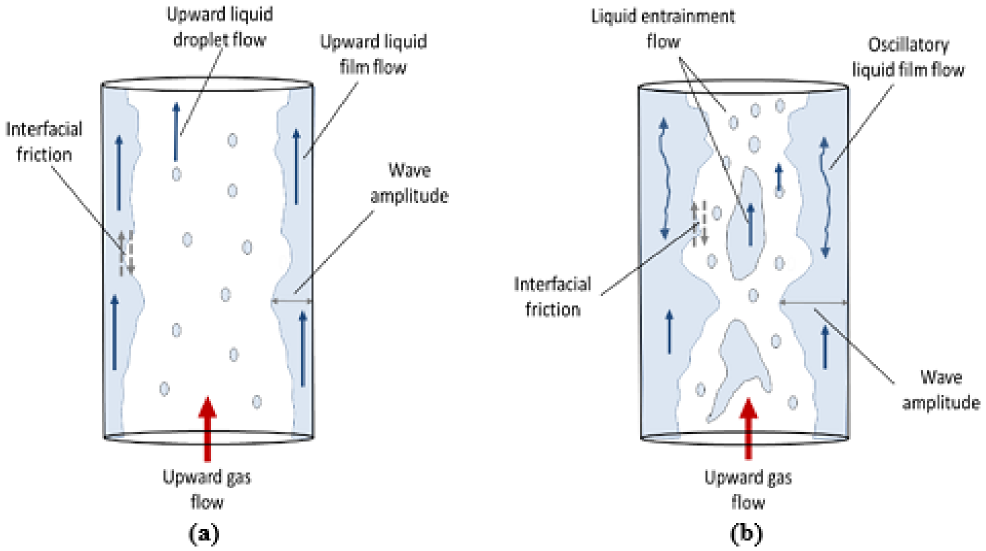

Figure 2.2: Schematic diagrams for a) annular flow and b) churn flow[15]

2.3.1 Numerical Studies on Annular and Churn Flows

Generally, two-phase flows are mainly studied through experiments based on which correlations for specific parameters are developed. No exact analytical solution exists for two-phase flow (annular flow) due to the complex nature of the flow in terms of the interfacial structure and the mechanism of droplet entrainment. Closure relationships are often utilized to estimate the interfacial friction and droplet entrainment. Numerical techniques are becoming more recognized in two-phase modeling in that they provide additional data to supplement those obtained from experiments. Usually, the main areas of investigation in two-phase annular and churn flows research include, the distribution of liquid film, mechanism of droplet entrainment and re-deposition[16], flooding and film reversal, liquid holdup and pressure gradient estimation[17], and many others. Discussed below are recent numerical studies conducted in annular flow and churn flow.

Annular Flow

In the work of Janyanti and Hewitt[18], a fixed liquid film configuration (roll wave) obtained directly from experimental observation was proposed in order to analyze a typical liquid film flow found in annular flow. Periodic boundary conditions were applied to both the inlet and outlet boundaries. The boundary conditions at the interface were obtained through experimental data found in existing studies. Three separate turbulence schemes (low-Reynolds $k-\varepsilon$, RNG $k-\varepsilon$, and standard $k-\varepsilon$) were utilized and the results compared. Results indicated that only small differences existed among the various turbulence models with the low-Reynolds $k-\varepsilon$ being the more accurate. It was concluded in their work that laminar flow exists in the liquid sublayer whereas in the vicinity of the wave peak, the flow is turbulent owing to the higher turbulent diffusivity than the molecular diffusivity in the proximity of the roll wave.

The gas core flow in a typical annular flow regime was modeled by Han[19] and Han[20]. Similar to the works of Jayanti[18], the effects of liquid film flow on the gas core were simplified and considered through the use of experimental correlations. The physical configuration of the interfacial wave as observed by Zhu[21] was utilized in their study. RNG $k-\varepsilon$ turbulence model was employed in their simulation. Periodic boundary conditions were utilized for both inlet and the outlet boundaries. The interface between the two phases was taken to be a moving wall with its entrainment rate and velocity obtained from experimental correlations. Results from the simulation showed that minimum static pressure exist at the vicinity of the wave peak and it was proposed that this might be the cause of the high droplet entrainment into the gas core region close to the wave peak.

To predict some of the flow parameters found in annular flow, Kishore[22] proposed a new model. They assumed a flat interface between the two phases with zero film thickness during the simulation. They obtained the parameters for the liquid film from correlations by Whalley[23]. The results from the model accurately predicted the axial pressure gradient and film height through experimental correlations. Even though the model was accurate, it could not account for the detailed wall information as well as the interfacial structure due to the zero-film height assumption.

Liu *et al.*[24] suggested a two-fluid model based on the volume of fluid (VOF) scheme to simulate two-phase annular flow in vertical pipes. They adopted the CFD commercial code, Fluent® (version 6.3.26). In their model, four assumptions were made. First, the gas core was assumed to be homogeneous mixture with a no-slip condition between the liquid droplets and the local gas phase. Also, the liquid droplets were taken to be small enough so that the gas diffusivity and the turbulent droplet were the same. Furthermore, the averaged spatial deposition and the correlations for the entrainment rate which were obtained from the open literature were justifiable for calculations involving wave scale and finally, the effects of the small ripple waves on the liquid film were ignored. They considered the effects of entrainment and deposition in their simulation using user defined function (UDF) option in the ANSYS Fluent® software. Even though the droplet effect was not accounted for in their simulation due to the no-slip assumption in the gas core, the model still gave good prediction when compared with data from experiments.

Churn Flow

Da Riva and Del Col[25] utilized the volume of fluid (VOF) model offered by ANSYS Fluent® commercial code to study air-water and R134a vapour-liquid mixture churn flow. Their 2D simulation was focused on the liquid inlet region of the pipe. Validating their results with experimental data yielded a satisfactory agreement. They proposed a simplified model of the levitation process of the ring-type in the churn flow. As part of their observations, increasing the liquid flow rate results in increasing the flooding waves formation thereby producing more disturbed and thicker liquid film on the pipe wall.

By assessing the capabilities of multiphase flow models in the modeling of churn flow, Parsi *et al.*[26] applied CFD techniques by adopting the Eulerian-Eulerian Multi-Fluid VOF often known as the hybrid model available in ANSYS Fluent® commercial code to simulate high flowrate air-water flows in a 76.2 mm pipe diameter. After successfully validating their 3D results (phase distributions, mean void fractions and average void fraction time series) with experimental data, they concluded that the hybrid model is capable of capturing the physical scenarios such as the passage of periodic interfacial structures of different length scales, effects of gas flow rate on huge wave amplitudes and the intricate wall film behavior.

As observed from above, the models can be categorized under a two-fluid model. However, other researchers attempted to simulate three-fluid model as seen in the works of Stevanovic and Studovic[27] and Alipchenkov *et al.*[28]. By this method, three distinct phases are involved, namely, the mainstream gas phase, dispersed liquid droplets and continuous liquid film. Here, a set of governing equations is assigned to each phase. Compared to the two-fluid model, this approach demands more computational effort and may pose convergence problems. Most of the studies tend to ignore the interactions at the two-phase interface and as a result, many detailed information regarding the interfacial structure is lost. This is due to the utilization of many empirical correlations.

2.4 Closure Models for Annular Flow

The microscopic physics linked with the wall and the interfaces is usually lost in the course of ensemble averaging of the conservation equations. This comprises of dynamic processes such as wall and interfacial shear, entrainment of droplets into the gas core, the droplet size distribution, and the effects of the wavy interface on the liquid film turbulence. In order to retrieve the lost information while averaging, closure models which describe the important physics are used. Most of these closure models till date are correlations due to the complicated nature of the flow and the difficulty involved in getting local information in the flow field.

Although numerically stable, correlations are usually subject to failure when used outside the assumptions made and the data range to which they were correlated. These correlations have limited applications in transient simulations in that they are usually correlated against equilibrium conditions. For the purpose of this study, only two of the most common closure models (interfacial shear stress and the liquid film thickness) utilized in annular flow are discussed below.

2.4.1 Interfacial Shear Stress

A shear stress is created at the interface between the liquid film and the gas core as a result of the relative motion between the two phases. Realizing that a higher shear is created on the high-speed gas core by a wavy interface than in the case of a smooth one, Wallis[7] assumed the interface as roughened wall and calculated the interfacial friction factor, f_I, by the modification of the single phase friction factor (f_{SP}) as in equation (2.8). He utilized the dimensionless length scale of liquid film thickness, δ, to the tube diameter, D.

$$f_I = f_{SP}\left(1 + 300\frac{\delta}{D}\right) \tag{2.8}$$

Neglecting the effect of the liquid film velocity, the interfacial shear, τ_I is calculated utilizing the wall friction model for a single phase:

$$\tau_I = \frac{1}{2} f_I \rho_G {U_G}^2 \tag{2.9}$$

Even though Wallis' model has been modified by many researchers (e.g. replacing U_G with the relative velocity), equation (2.8) forms the basis for most of the major models currently being used. Noting the trouble involved in initially estimating the film thickness, δ, Henstock and Hanratty[29] proposed a correlation to estimate the film thickness as a function of the liquid film Reynolds number, Re_{LF}, the gas core Reynolds number, Re_G, and the ratio of liquid to gas viscosities and densities as given in equation (2.10).

$$\begin{aligned} f_I &= f_{SP}(1 + 850F) \text{ Horizontal Pipe Flow} \\ f_I &= f_{SP}(1 + 1400F) \text{ Vertical Pipe Flow} \\ F &= Function\,(\; Re_G,\;\; Re_{LF}\;, \tfrac{\rho_L}{\rho_G}, \tfrac{\nu_L}{\nu_G}) \end{aligned} \tag{2.10}$$

Asali *et al.*[30] scaled the single phase friction factor using a friction length scale, l_f (given in equation (2.11)), having realized the less influence of the tube diameter on the friction factor (as observed in existing models). In place of ${}^{\delta}/_{D}$, they adopted ${}^{\delta}/_{l_f}$.

$$l_f = \frac{\nu_G}{\left({}^{\tau_I}/_{\rho_G}\right)^{0.5}} \tag{2.11}$$

In order to account for a wide range of liquid-air flows, pipe diameters and flowrates, Ambrosini *et al.*[31] modified the correlation of Asali *et al.*[30]. The modified correlation is expressed in terms of dimensionless parameters such as the gas Reynolds number (Re_D), the diameter based Weber number (We_D) and the dimensionless film height (${h_G}^+$) as provided in equation (2.12).

$$f_I = f_{SP}\left[1 + 13.8{We_D}^{0.2}{Re_G}^{-0.6}\left({h_G}^+ - 200\sqrt{{\rho_G}/{\rho_L}}\right)\right] \tag{2.12}$$

where, the dimensionless parameters are expressed below:

$$\begin{aligned} We_D &= \frac{\rho_G {U_G}^2 D}{\sigma} \\ Re_D &= \frac{U_G D}{\nu_G} \\ {h_G}^+ &= \frac{h {U_G}^*}{\nu_G} \end{aligned} \tag{2.13}$$

where, h is the film height and ${U_G}^*$ is the friction velocity expressed as $({\tau_i}/{\rho_G})^{0.5}$.

Brauner and Maron[32] made further modifications by adding a "memory effect" to enhance calculations for transition between smooth and wavy stratified flow[4]. Similarly, the effects of viscosity variations on interfacial shear were tested by Fukano and Furukawa[33] and a viscosity correction term was added. Finally, in order to satisfy a larger database, the correlation was shifted by Fore *et al.*[34]. Adopting a power law relationship between the interfacial shear (τ_I) and the wall shear (τ_W) stress, Ishii and Mishima[35] developed another relation as given below:

$$\tau_I = \tau_W \left(\frac{R}{R_W}\right)^m \tag{2.14}$$

where, R and R_W refer to the local radius and tube radius respectively. A similar approach (i.e. power law relationship) was utilized by Dobran[36] to obtain the effective momentum diffusivity (μ_{eff}) present in the wavy region as given in equation (2.15).

$$\frac{\mu_{eff}}{\mu_L} = 1 + C_1 \left(\delta^+ - {\delta_t}^+\right)^n \tag{2.15}$$

where δ^+ refers to the average liquid film height, ${\delta_t}^+$ is the liquid film height to the wave troughs, μ_L represents the liquid phase momentum diffusivity and n and C_1 are constants obtained from data. The base liquid film was modeled considering single phase flow while the wavy top of the liquid film was taken to be a function of the height of the wave instead of the wall distance. Hence, a modified diffusivity[4]. By correlating to air/water data, Dobran[36] obtained an expression for ${\delta_t}^+$. By utilizing the law-of-the-interface method, Kumar and Edwards[37] tried to minimize the number of correlations involved with the modeling of the interfacial shear stress by adopting a comparable law-of-the-wall relation to determine the shear directly from the turbulent kinetic energy. Upon realizing the relationship between the single-phase shear stress (τ) and the turbulent kinetic energy (k) as shown in equation (2.16):

$$\tau = C_\mu \rho k \tag{2.16}$$

Kumar and Edwards[37] made a similar assumption for the interfacial shear stress as presented in equation (2.17).

$$\begin{aligned}\tau_I &= T_m \left(U_L - U_I\right) \\ T_m &= \frac{\rho_G {C_\mu}^{0.25} k^{0.5}}{U^+}\end{aligned} \tag{2.17}$$

where U^+ is the dimensionless velocity obtained from a logarithmic relationship analogous to the law-of-the-wall with normalized terms against the film height, interfacial velocity and shear. U_i and U_L being the interfacial and liquid velocities respectively. No agreement with data was established due to the entrainment model utilized in their study.

2.4.2 Liquid Film Thickness

The liquid film thickness (height), δ, is mainly correlated against the liquid film Reynolds number, Re_F. By way of modification, other terms are included by some researchers to consider the effects of viscosity, density and buoyancy. Among the earlier researchers is Kosky[38], who, through a force balance of the liquid film, determined the average film thickness by assuming turbulent flow in the liquid film. Two equations were developed for the liquid film thickness for two regions of δ^+.

$$\begin{aligned}\delta^+ &= \left(0.5 Re_F\right)^{1/2} \qquad \text{for } \delta^+ < 25 \\ \delta^+ &= 0.0504 {Re_F}^{7/8} \qquad \text{for } \delta^+ > 25\end{aligned} \tag{2.18}$$

where the dimensionless film thickness, δ^+ is derived from the relation:

$$\delta^+ = \delta \frac{\rho_L U^*}{\mu_L} \tag{2.19}$$

where U^* refers to the friction velocity. Re_F refers to the liquid film Reynolds number and it is given as follows:

$$Re_F = \frac{\rho_L U_F D_{h,F}}{\mu_L} \tag{2.20}$$

where, $D_{h,F}$ and U_F represent the hydraulic diameter and velocity of the liquid film respectively.

The low Re_F flow model of Kosky[38] was modified by Asali *et al.*[30] in order to fit their data for air/water and air/aqueous glycerin vertical pipe flow. The derived correlation in their case is given as:

$$\delta^+ = 0.34 {Re_F}^{0.6} \tag{2.21}$$

The entrained droplet size and interfacial friction factor were re-correlated later on by Ambrosini *et al.*[31] for a large range of data with different working fluids and tube diameters. Their data fitted best when they adopted the average film thickness correlation (for $Re_F < 1000$) of Asali *et al.*[30] and the model of Kosky[38] (for $Re_F > 1000$).

2.5 Flow Reversal and Liquid Loading

Two main approaches exist in the literature for the study of flow reversal and liquid loading. These are, (i) the concept of liquid droplet entrainment and (ii) the concept of liquid film stability.

2.5.1 The Concept of Liquid Droplet Entrainment

As part of the founding researchers, Turner *et al.*[39] argued that liquid removal from gas wells can be taken care of by utilizing two physical models. First, a model from the liquid film movement on the pipe wall and second, a model from the entrained droplets flowing in the high-speed gas core. For the movement of the liquid film along the wall, they based their analysis on the fact that the film on the pipe wall must be carried upward in order to avoid liquid loading in the gas well. As a result, they came up with a model which is adopted to compute the minimum gas flow rate needed to achieve this goal. They adhered to the analysis of Dukler[40] and Hewitt[41]. In the entrained liquid droplet model, they utilized the mechanics of particle and drop breakup to establish a relationship for the minimum gas flow rate that would be needed to carry or lift the liquid droplets out of the gas well. They found that the minimum gas velocity is simply the terminal velocity of the droplet. They recommended an upward adjustment of 20% in the model to ensure its accuracy. The models were validated with field data from gas wells with wellhead pressures mostly above 500 psi (high pressure wells). After field observations, it was concluded that prediction based on the liquid film movement were inaccurate. It was therefore, recommended that predictions should be based on the entrained droplet model alone in order to ensure a complete removal of the liquid phase from the gas well.

Most of the wellhead flowing pressures observed in the field data of Turner *et al.*[39] were very high (above 500 psi). Coleman *et al.*[42] then adopted Turner's model in a field test where the wellhead flowing pressures were below 500 psi (low pressure gas wells). It was noticed that the model could predict better results corresponding to field data without any modification to Turner's model as suggested by Turner and his colleagues. Coleman and his team observed that the pressure and diameter of the wellbore contributed intensively in the commencement of liquid loading. However, they suggested that gravity, temperature and interfacial surface tension have less contribution to this phenomenon and their effects could be neglected.

Nosseir *et al.*[43] followed the fundamental analysis of Turner but considered different conditions of the flow resulting in different flow regimes. They noted that at some instance (with a particular flow regime), Turner's model worked perfectly without the 20% upward adjustment as suggested by Turner and his group. They observed again that the model depended on the type of flow regime which Turner and his group only consider as a constant turbulent flow regime ($10^4 \leq Re \leq 2\times10^5$). They then came up with two models that do not consider an empirical adjustment but performs better with field data. Their models consider the different flow regimes (transition and highly turbulent).

In 2002, Li *et al.*[44] observed that deformation of falling droplets in the gas phase was neglected in Turner and Coleman's models. They proposed in their work that as the droplets are entrained in the high-speed gas phase, they are deformed as a result of pressure distribution and they change shape from spherical to convex bean whose sides are not equal (flattened shape). Analyses showed that spherical droplets have smaller surface area compared to that flattened droplets and as such require a higher value of the terminal velocity and critical flow rate to be entrained while those with flat-shapes are easily carried out of the well.

Westende[5] conducted an experiment to measure the size of the droplet at the start of liquid loading using 2-in ID vertical pipe. It was observed that there were no falling droplets and that the size of the droplet was smaller than the diameter required to achieve the settling velocity by one order of magnitude. It was concluded however, that the idea of liquid loading should be characterized by the liquid film instability.

Tan *et al.*[45] in their paper came up with a model which considers the dependence of liquid droplet diameter on the critical liquid flowrate removal from gas wells. Their model was based on observational technique. They compared and evaluated the performance of various critical liquid removal flow rate models by examining model outputs. They noticed that the critical liquid removal flow rates determined by the different models varied significantly. Utilizing the balance relationship between the total surface energy of the droplets of the liquid and turbulent kinetic energy of gas flow, they obtained the new model under critical conditions. A droplet diameter was obtained from the balanced total surface free energy, which was then substituted into Turner's equation for critical liquid removal velocity to end up with the new model. They then verified the reliability of the new model by comparing its results with gas well production data from four gas reservoirs in China. The model was again compared with models by Turner *et al.*[39], Coleman *et al.*[42] and Li *et al.*[44]. It was found after comparison that the new model gave almost the same results with Li *et al.*[44] when the tubing pressure is less than 10 MPa and production gas-water flow rate ratio (GWR) exceeds 1×10^4 m^3/m^3 while with a GWR values between 0.137×10^4 m^3/m^3 and 1×10^4 m^3/m^3, the new model approaches that of Coleman *et al.*[42].

2.5.2 The Concept of Liquid Film Stability

Zabaras *et al.*[46] conducted an experiment to investigate an upward co-current liquid and gas annular flow in a 2-in ID vertical pipe. They observed a liquid film flow changing behavior near the wall of the pipe. They noticed from their analysis that the liquid film flowed in the opposite direction at low gas flow rates. As the film flowed in the reverse direction, the dominant flow regime observed was the churn flow. However, the liquid film was found to be flowing in the upward direction at high gas flow rates and the noticeable flow pattern was annular flow. The direction of the wall shear stress was determined and it was observed that the shear stress gave a negative value for high gas flow rates showing a correlation for the local film thickness. At the reversal condition, it was noticed that the sign of the wall shear stress changed periodically.

Adopting water and air as the main test fluids, Belt[47] conducted an experiment to study film reversal in 2-in ID vertical and inclined pipes. Film distribution mechanisms were investigated through the observation of wave characteristics, interfacial friction and secondary flow. He measured the film thickness by utilizing conductance sensors. He demonstrated that the prediction of the interfacial friction can be achieved by roll waves height and spatial distribution. In conclusion, he said that in determining the liquid film thickness, the roll waves must be considered.

In his experiment, Yuan[48] investigated liquid loading and well deviation effects associated with gas wells. It was established that the superficial gas velocity conforming to the least pressure gradient concurs with the start of liquid loading. He noticed as the superficial liquid velocity increases, liquid loading tends to occur at higher gas flow velocities.

Guner[17] conducted an experimental study on liquid loading of a gas well by adopting air and tap water as test fluids in a 3-in inner diameter pipes. The experiment was conducted using deviation from $0°$ to $45°$ from the vertical. A total number of 156 tests were conducted and CFD simulations were performed to comprehend the velocity and phase distributions. The experiment showed that increasing the deviation from the vertical increases the critical gas velocity of liquid loading. It was again noticed that the superficial gas velocity corresponding to complete film reversal could be used as the critical gas velocity to predict initiation of liquid loading for vertical and deviated wells.

2.6 Numerical Studies on Flow Reversal and Liquid Loading

Very little has been done on computational modeling of annular flow in a vertical pipe especially for liquid film reversal and liquid loading. In the following, we present some of the numerical studies reported in the literature.

Predicting the formation of water buildup in a gas well, Dousi *et al.*[49] proposed that gas wells can operate at two different rates, namely, a stable rate where full production is observed and a lower metastable rate where the effects of liquid loading is significant. It was observed in their analysis that even at a metastable state below the critical value proposed by Turner *et al.*[39] or the minimum stable, the gas well can still produce. The model did not describe the physics of the flow in the liquid film so no information on that was provided.

Vieiro *et al.*[11] applied CFD techniques to study the two-phase liquid loading phenomenon. They used a 2D (axisymmetric) simplification to execute the numerical simulation in ANSYS CFX® version 13.0 by adopting the homogeneous model. The criterion used to determine the critical gas velocity was not clearly defined in their work. However, the pressure drop measurement showed good agreement with some of the data from Westende[5]. Included in their work were measurements of liquid film thickness, velocity profiles and liquid volume fractions.

Despite the numerous studies reported in the open literature, very little has been done in the area of applying numerical techniques to modeling annular flow and flow reversal. This study therefore aims at modeling annular flow through the use of numerical techniques and predicting the onset of film reversal. The assertion that the superficial gas velocity corresponding to the onset of film reversal could be used as the critical gas velocity to predict the initiation of flow reversal is adopted for study in this work.

2.7 Liquid Loading Criterion

Studying liquid loading phenomenon through liquid film flow reversal in vertical pipes is related to the churn flow-annular flow transition[3]. For a gas flow velocity above that for the flow reversal will result in upward annular flow. A correlation for the flow reversal condition (churn flow-annular flow transition) was first proposed by Wallis[10]. The correlation is the modified gas phase Froude (Fr_G) number which is given in equation (2.6). The transition occurs in regions where $Fr_G \approx 1$. Wallis[10] suggested for the flow reversal condition, Fr_G has a value of $0.8 - 0.9$.

Noted by Hewitt and Hall-Taylor[3], two criteria can be used to predict the onset of liquid loading. These criteria are the minimum pressure gradient and the zero-wall shear stress. If the gas velocity is gradually reduced in an upward co-current flow, the pressure gradient falls until a minimum is reached. At this instant, the flow reversal point is reached. Due to the effects of the gravitational force in upward annular flow, the liquid film shear stress falls from the interface to the wall. Reducing the gas velocity decreases the interfacial shear stress. Gradually, the wall shear stress falls to zero. Further reduction in the interfacial shear can result in a negative wall shear stress, an indication of downward liquid film movement (flow reversal) on the wall. Most experimental analyses use the minimum pressure gradient as the point for flow reversal as presented in the work by Westende[5] and Guner[17].

2.8 Two-Phase Modeling Techniques

At the moment, two main approaches exist for solving multiphase flow problems using computational fluid dynamics (CFD) techniques[50]. The first being the Euler-Lagrange approach and the second, the Euler-Euler approach.

The Euler-Lagrange approach treats the fluid phase as a continuum by solving the Navier-Stokes equations while the dispersed phase on the other hand, is solved by means of tracking many particles, droplets or bubbles via the computed flow field. Momentum, mass and energy exchange can occur between the dispersed phase and the fluid phase. In this approach, the dispersed phase is assumed to occupy a small volume fraction although high mass loading is acceptable. Computations of the droplet or particle trajectories are done individually at specified intervals during the fluid phase calculation[50]. This makes the Euler-Lagrange approach inappropriate for modeling some typical multiphase problems (such as, fluidized beds, liquid-liquid mixtures or any application requiring the computation of the volume fraction of the secondary phase). However, the Euler-Lagrange approach is suitable for the modeling of coal and liquid fuel combustion, spray dryers and some particle-laden flows.

The Euler-Euler approach treats the distinct phases as interpenetrating continua with each phase occupying a certain volume in the flow domain. The volume fractions of each phase are assumed to be continuous functions of time and space and they sum up to unity. Derivation of conservation equations for each phase is made to yield a set of equations, with similar structure for all phases. These derived equations are usually averaged; hence, the microscopic characteristics are lost. However, the lost information as result of the averaging are accounted for via the utilization of closure models[4]. These closure models depend on the physical phenomena being modeled. Three averaging methods are found in literature, namely, time, space and ensemble averaging.

2.8.1 Available Euler-Euler Models

Three different Euler-Euler models are provided in ANSYS Fluent®, namely, the mixture model, the volume of fluid (VOF) model and the Eulerian model.

The mixture model on the other hand, is capable of handling two or more phases (fluids or particulates). The phases involved here are treated as interpenetrating continua. This model solves the mixture momentum equation and prescribes relative velocities to describe the dispersed phases. However, it can be used to model homogeneous multiphase flow without relative velocities for the dispersed phases.

The VOF model being a surface-tracking technique is applied to a fixed Eulerian mesh. Designed for two or more immiscible fluids, VOF is employed where the position of the interface is of great interest. Under this model, the involved fluids share a single set of momentum equations and the volume fraction of each fluid in each of the computational cell is tracked throughout the flow domain. It is can be applied to several multiphase flows such as stratified flows, sloshing, filling, free-surface flows, large bubble motion and the steady or transient tracking of any liquid-gas interface. Even though this model (VOF) has proven to be successful in many researches[24][20], it does have some limitations when it comes to flows where there is momentum exchange between the phases[51]. This is because the phases involve share a common set of equations and as a result, the momentum exchange between them is ignored.

Finally, the most complex model among the multiphase models in ANSYS Fluent® is the Eulerian model[50]. A set of momentum and continuity equations are solved for each phase involved. Coupling in this method is achieved through the pressure and interface exchange coefficients. The momentum exchange between the phases is dependent on the type of mixture being modeled. Areas of applications include bubbly columns, risers, particle suspension, and fluidized beds. It can model multiple separate, yet interacting phases.

Accordingly, the Eulerian model and the VOF model with surface tracking technique are the most widely used to model two-phase air-water flows. Incorporated in ANSYS Fluent® is a way to utilize both the Eulerian and VOF model. This is done by selecting the Multi-Fluid VOF model under the Eulerian multiphase model. This allows the researcher to be able to use the sharpening interface tracking schemes like Geo-Reconstruct, compressive, CICSAM and Modified HRIC under the Explicit VOF option. This model has the advantage of overcoming some limitations of the VOF model due to the shared velocity and temperature formulation. The numerous applications of this model include the study of flooding phenomenon[51] and study of churn flow[25][52]. It is often adopted for cases requiring sharp treatment of the interface. For details about this formulation, please refer to user manual of ANSYS Fluent® commercial software.

Eulerian Multi-Fluid VOF Model

The main governing equations for the flow in the Eulerian Multi-Fluid VOF model are the independent momentum and mass conservation equations for the two phases involved (water and air). These are given in ANSYS Fluent® [50]

1. Mass Conservation

$$\frac{\partial}{\partial t}(\alpha_q \rho_p) + \nabla \cdot \big(\alpha_q \rho_p \mathbf{U}_q\big) = \sum_{p=1}^{n} (\dot{m}_{pq} - \dot{m}_{qp}) + S_q \tag{2.22}$$

2. Momentum Conservation

$$
\begin{aligned}
\frac{\partial}{\partial t}\left(\alpha_q \rho_q \mathbf{U}_q\right) + \nabla \cdot \left(\alpha_q \rho_q \mathbf{U}_q \mathbf{U}_q\right) = &- \alpha_q \nabla p + \nabla \cdot \bar{\bar{\tau}}_q + \alpha_q \rho_q g \\
&+ \sum_{p=1}^{n} \left(\mathbf{R}_{pq} + \dot{m}_{pq} \mathbf{U}_{pq} - \dot{m}_{qp} \mathbf{U}_{qp}\right) \quad (2.23) \\
&+ \left(\mathbf{F}_q + \mathbf{F}_{lift,q} + \mathbf{F}_{vm,q} + \mathbf{F}_{td,q}\right)
\end{aligned}
$$

where $\bar{\bar{\tau}}_q$ is the phase q stress-strain tensor and it is given as:

$$
\bar{\bar{\tau}}_q = \alpha_q \mu_q \left(\nabla \mathbf{U}_q + \nabla \mathbf{U_q}^T\right) + \alpha_q \left(\lambda_q - \frac{2}{3}\mu_q\right) \nabla \cdot \mathbf{U}_q \bar{\bar{I}} \quad (2.24)
$$

where $\mathbf{U}_q$ is the velocity of phase q; $\dot{m}_{pq}$ is the mass transfer from phase p to phase q; $\dot{m}_{qp}$ is the mass transfer from phase q to phase p; S_q is a source term; α_q is the volume fraction of phase q; μ_q is the shear viscosity of phase q; λ_q is the bulk viscosity of phase q; $\mathbf{F}_q$ is an external body force; $\mathbf{F}_{lift,q}$ is a lift force; $\mathbf{F}_{wl,q}$ is a wall lubrication force; $\mathbf{F}_{vm,q}$ is a virtual mass force; $\mathbf{F}_{td,q}$ is a turbulent dispersion force; $\mathbf{R}_{pq}$ is an interaction between phases; p is the pressure shared by all the phases; $\mathbf{U}_{pq}$ and $\mathbf{U}_{qp}$ represent the interphase velocities defined as follows:

$$
\mathbf{U}_{pq} = \begin{cases} \mathbf{U}_p; & \text{if } \dot{m}_{pq} > 0 \\ \mathbf{U}_q; & \text{if } \dot{m}_{pq} < 0 \end{cases} \quad (2.25)
$$

In a similar way,

$$\mathbf{U}_{qp} = \begin{cases} \mathbf{U}_q; & \text{if } \dot{m}_{qp} > 0 \\ \\ \mathbf{U}_p; & \text{if } \dot{m}_{qp} < 0 \end{cases} \tag{2.26}$$

Appropriate closer relationships are required for the interphase force $\mathbf{R}_{pq}$, in equation (2.23). $\mathbf{R}_{pq}$ depends on friction, pressure, cohesion and other effects. It is subject to the conditions:

$$\mathbf{R}_{pq} = -\mathbf{R}_{qp} \text{ and } \mathbf{R}_{qq} = 0 \tag{2.27}$$

The interphase force should also satisfy (see ANSYS Fluent® software),

$$\sum_{p=1}^{n} \mathbf{R}_{pq} = \sum_{p=1}^{n} K_{pq}(\mathbf{U}_p - \mathbf{U}_q) \tag{2.28}$$

where $\mathbf{U}_p$ and $\mathbf{U}_q$ are the phase velocities; $K_{pq} = K_{qp}$ is the interphase momentum exchange coefficient which is given by the expression:

$$K_{pq} = \frac{\rho_p f}{6\tau_p d_p A_i} \tag{2.29}$$

where A_i is the interfacial area; d_p is the bubble or droplet diameter of phase p; τ_p is the particulate relaxation time which is expressed as:

$$\tau_p = \frac{\rho_p {d_p}^2}{18\mu_q} \tag{2.30}$$

and f is the drag function which is given as:

$$f = \frac{C_D Re_R}{24} \tag{2.31}$$

where C_D is the drag coefficient which is usually computed from empirical correlation known as the drag models; Re_R is the relative Reynolds number given as:

$$Re_R = \frac{\rho_q |\mathbf{U}_p - \mathbf{U}_q| d_p}{\mu_q} \tag{2.32}$$

2.8.2 Available Drag Models

Almost all definitions of the drag function, f, comprise of a Reynold-number-based drag coefficient, C_D. There are several models in the open literature for the calculation of C_D in equation (2.31). The available drag models in ANSYS Fluent® commercial code include, Schiller-Naumann model[53], Morsi-Alexander model[54], symmetric model, Grace *et al.* model[55], Tomiyama *et al.* model[56], Ishii model[57] and Anisotropic drag model. The Schiller-Naumann model is generally applicable to all fluid-fluid multiphase simulation. Morsi-Alexander model adjusts the function definition frequently over a large range of Reynolds number making it the most complete model. The only problem with this model is that it is less stable compared with the other models. The symmetric drag model is more suitable for flows where the secondary phase in one region of the domain becomes the primary (continuous) phase in another. Grace *et al.* model and Tomiyama *et al.* model more applicable to bubbly flows. Ishii model is applicable to boiling flows only. For free surface flow applications, the anisotropic drag model is recommended. This drag model is based on a higher drag in the normal direction to the interface and a lower drag in the direction tangential to the interface. Detailed mathematical relations can be found in ANSYS Fluent® commercial software.

2.9 CFD Simulation Methodologies for Two-Phase Flows

Several numerical methodologies reported in the literature for the modeling of two-phase flow are described in this section. The flow features in this study has shown that both the gas and the liquid phases are in the turbulent flow regime and the liquid film flow exhibits near-wall flow features. Due to the amount of computational resources required to solve the time dependent Navier-Stokes (N-S) equations, in most of the available literature, the Reynolds-averaged Navier-Stokes (RANS) equations are usually solved for turbulent flows, hence, serve as the main governing equations for the transport of the averaged flow quantities. The RANS equations are time-averaged[58] and primarily used to describe turbulent flows. Expressed below are the Reynolds-Averaged Navier-Stokes (RANS) equations in the Cartesian coordinate system:

1. Continuity

$$\frac{\partial \rho}{\partial t} + \frac{\partial}{\partial x_i}\big(\rho U_i\big) = 0 \tag{2.33}$$

2. Momentum

$$\frac{\partial}{\partial t}\big(\rho U_i\big) + \frac{\partial}{\partial x_j}\big(\rho U_i U_j\big) = -P_i + \frac{\partial}{\partial x_j}\left[\mu\left(\frac{\partial U_i}{\partial x_j} + \frac{\partial U_j}{\partial x_i}\right)\right] - \frac{\partial}{\partial x_j}\big(\rho\overline{u_i' u_j'}\big) \tag{2.34}$$

where U_i and u_i' are the mean and the fluctuating velocity components ($i = 1, 2$ for 2D flows); P_i is the pressure gradient; μ and ρ are the dynamic viscosity and density of the fluid; x_i represents the coordinate; and the last term, $\rho\overline{u_i' u_j'}$ represents the effects of turbulence and is referred to as Reynolds stress tensor. To close the RANS equations, the Reynolds stress tensor must be modeled [58]. One common approach to achieve this is to use the hypothesis of Boussinesq to relate the Reynolds stresses to the mean velocity gradients as shown:

$$\rho\overline{u_i' u_j'} = \mu_t\left(\frac{\partial U_i}{\partial x_j} + \frac{\partial U_j}{\partial x_i}\right) - \frac{2}{3}\rho\delta_{ij}k \tag{2.35}$$

where, k is the turbulent kinetic energy and it is given as:

$$k = \frac{1}{2}\overline{u_i' u_i'} \tag{2.36}$$

and μ_t is the turbulent or eddy viscosity which is a function of k and ε (in $k -$

ε model) or k and ω (in $k - \omega$ model). These models are described in the next section. Generally, turbulent flows show characteristics of small fluctuations in velocity and pressure fields. Usually, these fluctuations are computationally expensive to resolve, hence the time-averaging of the Navier-Stokes equations[19].

2.9.1 Overview of Turbulence Models

To close the RANS equations, the Reynolds stress tensor is modeled to account for the effects of turbulence and the increased viscosity. The most commonly used transport equations available in literature for two-phase flow turbulence modeling are the two- equation models ($k-\varepsilon$, and $k-\omega$ models). The first equation is for the turbulent kinetic energy, k, and second equation for the turbulent dissipation, ε, or the specific turbulence dissipation rate, ω. The second equation usually determines the scale of the turbulence. Using the two-equation models, computational time is significantly minimized[19]. These two additional equations are added to the averaged N-S equations and computed. In this thesis, only the $k - \varepsilon$ turbulent model will be studied in detail.

The $k - \varepsilon$ Turbulence Model

This closure model has been effectively utilized by many researchers in a wide range of multiphase flow applications including bubbly flows, slug flows, stratified flows, churn flows, annular flows and sedimentation phenomena as reported by Han[19]. It was also utilized in the study of low liquid loading phenomena by Karami *et al.*[59]. ANSYS Fluent® commercial software makes available three options for the $k-\varepsilon$ turbulence model, namely, standard $k-\varepsilon$ model, renormalization-group (RNG) $k-\varepsilon$ model and realizable $k-\varepsilon$ model. The main differences between these models are: (1) turbulent viscosity calculation method, (2) the turbulent Prandtl numbers that govern the turbulent diffusion of k and ε and (3) the generation and destruction terms in the $\varepsilon-$ equation [50].

Proposed initially by Launder and Spalding[60], the standard $k-\varepsilon$ is a high Reynolds number turbulence model and as such only applicable to fully turbulent flows. The transport equations describing the standard $k-\varepsilon$ turbulent model are presented as follows:

$$\frac{\partial}{\partial t}(\rho k)+\frac{\partial}{\partial x_i}(\rho U_i k)=\frac{\partial}{\partial x_j}\left[\left(\mu+\frac{\mu_t}{\sigma_k}\right)\frac{\partial k}{\partial x_j}\right]+G_k+G_b-\rho\varepsilon-Y_M+S_k \quad (2.37)$$

and

$$\begin{aligned}\frac{\partial}{\partial t}(\rho\varepsilon)+\frac{\partial}{\partial x_i}(\rho U_i\varepsilon)=&\frac{\partial}{\partial x_j}\left[\left(\mu+\frac{\mu_t}{\sigma_\varepsilon}\right)\frac{\partial\varepsilon}{\partial x_j}\right]\\&+C_{1\varepsilon}\frac{\varepsilon}{k}(G_k+C_{3\varepsilon}G_b)-C_{2\varepsilon}\rho\frac{\varepsilon^2}{k}+S_k\end{aligned} \quad (2.38)$$

In the above equations, G_k is the generation of turbulence kinetic energy due to the mean velocity gradients; G_b is the generation of turbulence kinetic energy due to buoyancy; Y_M is the contribution of the fluctuating dilatation in compressible turbulence to the overall dissipation rate; $C_{1\varepsilon}$, $C_{2\varepsilon}$ and $C_{3\varepsilon}$ are constants; σ_k and σ_ε are the turbulent Prandtl numbers for k and ε respectively; S_k and S_ε are user-defined source terms. The turbulent viscosity, μ_t in the standard $k-\varepsilon$ is calculated using the relation:

$$\mu_t = \rho C_\mu \frac{k^2}{\varepsilon} \tag{2.39}$$

where C_μ is a constant. Commonly used values for the constants in the above transport equations obtained from experiments are as follows [60]: $C_{1\varepsilon} = 1.44$, $C_{2\varepsilon} = 1.92$, $C_\mu = 0.09$, $\sigma_k = 1.0$ and $\sigma_\varepsilon = 1.3$. There have, however, been several improvements to improve its performance. The RNG $k - \varepsilon$ model and the realizable $k - \varepsilon$ model are other alternatives with improved performance than the standard $k - \varepsilon$ model.

The realizable $k - \varepsilon$ was proposed by Shin *et al.*[61]. Comparing to the standard $k - \varepsilon$ model, the realizable $k - \varepsilon$ has a new formulation for the turbulent viscosity. It also has a new form of the transport equation derived for the dissipation rate, ε. This model has the advantage of predicting the spreading of both planar and round jet accurately. The realizable $k - \varepsilon$ model by its form is also a high Reynolds number turbulence model. This model uses the following transport equations for k and ε:

$$\frac{\partial}{\partial t}(\rho k) + \frac{\partial}{\partial x_i}(\rho U_i k) = \frac{\partial}{\partial x_j}\left[\left(\mu + \frac{\mu_t}{\sigma_k}\right)\frac{\partial k}{\partial x_j}\right] + G_k + G_b - \rho\varepsilon - Y_M + S_k \tag{2.40}$$

and

$$\begin{aligned}\frac{\partial}{\partial t}(\rho\varepsilon)+\frac{\partial}{\partial x_i}(\rho U_i\varepsilon)=&\frac{\partial}{\partial x_j}\left[\left(\mu+\frac{\mu_t}{\sigma_\varepsilon}\right)\frac{\partial\varepsilon}{\partial x_j}\right]+\rho C_1 S\varepsilon\\&-\rho C_2\frac{\varepsilon^2}{k+\sqrt{v\varepsilon}}+C_{1\varepsilon}\frac{\varepsilon}{k}C_{3\varepsilon}G_b+S_\varepsilon\end{aligned}\tag{2.41}$$

where $C_1=\max\left[0.43,\frac{\eta}{\eta+5}\right]$; $\eta=S\frac{k}{\varepsilon}$; $S=\sqrt{2S_{ij}S_{ij}}$; G_k, G_b, Y_M, S_k and S_ε have the same description as in the standard $k-\varepsilon$ model; C_2, $C_{1\varepsilon}$ and $C_{3\varepsilon}$ are constants. The eddy viscosity (turbulent viscosity) is obtained from equation (2.39) but C_μ is computed as follows:

$$C_\mu=\frac{1}{A_o+A_s\frac{kU^*}{\varepsilon}}\tag{2.42}$$

where

$$U^*\equiv\sqrt{S_{ij}S_{ij}+\tilde{\Omega}_{ij}\tilde{\Omega}_{ij}}\tag{2.43}$$

and

$$\tilde{\Omega}_{ij}=\Omega_{ij}+2\varepsilon_{ijk}\omega_{ij}\tag{2.44}$$

where

$$\Omega_{ij}=\overline{\Omega}_{ij}+\varepsilon_{ijk}\omega_{ij}\tag{2.45}$$

where Ω_{ij} refers to the mean rate of rotation tensor viewed in a moving reference frame with the angular velocity, ω_k. Constants A_o and A_s are given as $A_o = 4.04$ and

$$A_s = \sqrt{6}\cos\phi \tag{2.46}$$

where

$$\phi = \frac{1}{3}\cos^{-1}\left(\sqrt{6}W\right) \tag{2.47}$$

$$W = \frac{S_{ij}S_{jk}S_{ki}}{\tilde{S}^3} \tag{2.48}$$

$$\tilde{S} = \sqrt{S_{ij}S_{ij}} \tag{2.49}$$

$$S_{ij} = \frac{1}{2}\left(\frac{\partial U_j}{\partial x_i} + \frac{\partial U_i}{\partial x_j}\right) \tag{2.50}$$

The model constants are given as: $C_{1\varepsilon} = 1.44$, $C_2 = 1.9$, $\sigma_k = 1.0$ and $\sigma_\varepsilon = 1.2$. Initial results from Shin *et al.*[61] and Kim *et al.*[62] showed that this model can provide best performance in separated flow and flows with complex secondary flow. However, specific conditions for its superior performance over the RNG $k - \varepsilon$ model is unclear[19].

Yakhot and Orszag[63] proposed the RNG $k-\varepsilon$ model which was basically derived from the instantaneous N-S equation by utilizing a rigorous statistical technique known as "renormalization group" method, hence the name RNG $k-\varepsilon$ model. Four main improvements are made in this model, namely, (1) it has a new term in its Îţ equation to improve the accuracy of simulating rapidly strained flows; (2) consideration is made for the effects of swirl and hence more accurate for swirl flow application; (3) unlike the standard $k-\varepsilon$ model, where constant values of the turbulent Prandtl numbers are used, the RNG $k-\varepsilon$ model utilizes an analytical formula; and (4) an analytically derived differential equation is provided for the effective viscosity that accounts for low-Reynolds number effects.

The two additional transport equations in the RNG $k-\varepsilon$ turbulence model are given below for k and ε respectively:

$$\frac{\partial}{\partial t}(\rho k)+\frac{\partial}{\partial x_i}(\rho U_i k)=\frac{\partial}{\partial x_j}\left(\alpha_k \mu_{eff}\frac{\partial k}{\partial x_j}\right)+G_k+G_b-\rho\varepsilon-Y_M+S_k \tag{2.51}$$

and

$$\begin{aligned}\frac{\partial}{\partial t}(\rho\varepsilon)+\frac{\partial}{\partial x_i}(\rho U_i\varepsilon)=&\frac{\partial}{\partial x_j}\left(\alpha_\varepsilon \mu_{eff}\frac{\partial \varepsilon}{\partial x_j}\right)\\&+C_{1\varepsilon}\frac{\varepsilon}{k}(G_k+C_{3\varepsilon}G_b)-C_{2\varepsilon}\rho\frac{\varepsilon^2}{k}-R_M+S_\varepsilon\end{aligned} \tag{2.52}$$

where G_k refers to the production of turbulent kinetic energy calculated from the relation:

$$G_k = -\rho \overline{u_i' u_j'} \frac{\partial U_j}{\partial x_i} \tag{2.53}$$

G b refers to the generation of k due to buoyancy as function of gravity and temperature gradient and is expressed as:

$$G_b = \beta g_i \frac{\mu_t}{Pr_t} \frac{\partial T}{\partial x_i} \tag{2.54}$$

In this study, $G_b = 0$, because the temperature remains constant. Y_M represents the dilatation term. This term is utilized in compressible flow since it reflects the compressibility of high-Mach number flows on turbulence. It is usually neglected in incompressible flows. α_k and α_ε represents the inverse effective Prandtl numbers for k and ε and are calculated from the following relation derived from the theory of RNG:

$$\left| \frac{\alpha - 1.3929}{\alpha_o - 1.3929} \right|^{0.6321} \left| \frac{\alpha + 2.3929}{\alpha_o + 2.3929} \right|^{0.3679} = \frac{\mu}{\mu_{eff}} \tag{2.55}$$

Here, $\varepsilon_k = 1.0$; μ is the fluid physical viscosity; and μ_{eff} is the effective viscosity (the sum of the molecular viscosity of the fluid and turbulent viscosity of the flow). In ANSYS Fluent® commercial software, S_k and S_ε are user-defined source terms. In the current study, these source terms are set to zero since there no specific sources to generate or dissipate k. R_ε is an additional term found in the RNG model which makes it different from the standard $k - \varepsilon$ model. It has the following expression:

$$R_\varepsilon = \frac{C_\mu \rho \eta^3 \left(1 - \frac{\eta}{\eta_o}\right)}{1 + \beta \eta^3} \frac{\varepsilon^2}{k} \tag{2.56}$$

where $\eta = S\frac{k}{\varepsilon}$ (S refers to the modulus of strain rate tensor), $\eta_o = 4.38$, and $\beta = 0.012$. $C_{1\varepsilon}$, $C_{2\varepsilon}$ and $C_{3\varepsilon}$ are constants. $C_{3\varepsilon}$ is not specified in ANSYS Fluent®, instead it is computed by ANSYS Fluent®. According to Choudhury[64], the values of C_μ, $C_{1\varepsilon}$ and $C_{2\varepsilon}$ are analytically derived from RNG theory and respectively take values of 0.0845, 1.42 and 1.68.

For the RNG turbulent to better handle the low-Reynolds number and near-wall flows, a differential equation is utilized to compute the turbulent viscosity, μ_t. This relation is given as:

$$\frac{d}{d\nu'}\left(\frac{\rho^2 k}{\sqrt{\varepsilon \mu}}\right) = 1.72 \frac{\nu'}{\sqrt{\nu'^3 - 1 + C_\nu}} \tag{2.57}$$

where ν' is the turbulent kinematic viscosity $\left(\frac{\mu_{eff}}{\mu}\right)$, $\mu_{eff} = \mu + \mu_t$ and $C_\nu = 100$.

2.9.2 Surface Tension Modeling

In the modeling process, surface tension becomes an important variable to consider. It results from the sharp changes in the molecular forces of attraction at the two-phase interface due the discontinuous changes in properties. Usually in complex geometries, modeling this local force becomes a stressful task. Two main surface tension models commonly used include, the continuum surface force

(CSF) and the continuum surface stress (CSS).

The CSF model was proposed by Brackbill *et al.*[65] and it is utilized where the surface tension is along the surface and only the normal forces to the interface are considered. In the CSF model, the surface tension is modeled in a non-conservative way.

On the other hand, a conservative formulation is used in the modeling of the CSS model. The CSS is mostly used in applications involving variable surface tension. But most commonly utilized model in literature is the continuum surface force (CSF) derived by Brackbill *et al.*[65]. For only two phases, the force is expressed as:

$$F_{CSF} = \sigma \frac{\rho_{LG} \kappa_L \nabla \alpha_L}{\frac{1}{2}\left(\rho_L + \rho_G\right)} \tag{2.58}$$

where κ is the local curvature of the interface, σ is the coefficient of surface tension. In a nonconservative manner, the surface tension force in the CSF method is written as:

$$F_{CSF} = \sigma k \nabla \alpha \tag{2.59}$$

For cases with variable surface tension as in the CSS model, the surface tension force (F_{CSS}) is given as:

$$F_{CSS} = \nabla \cdot \left[\sigma \left(|\nabla\alpha| \, I - \frac{\nabla\alpha \otimes \nabla\alpha}{|\nabla\alpha|} \right) \right] \tag{2.60}$$

where I is the unit tensor; $\otimes$ is the tensor product of the two vectors; and α is the volume fraction. Equation (2.60) is only valid for constant surface tension. For cases where $Re >> 1$, the surface tension effects can be neglected for Weber number, $We >> 1$[50], where the Weber number, We, is expressed as:

$$We = \frac{\rho L U^2}{\sigma} \tag{2.61}$$

where L is the characteristic length.

2.9.3 Near-Wall Treatment

Special treatments are needed to make the $k-\varepsilon$ models more suitable for near-wall flows since they are basically valid for turbulent core flows, thus, flow regions sufficiently far from the walls. Generally, the near-wall flows comprise of three regions, namely, (1) a viscous sublayer region where the effect of molecular viscosity is very critical in the flow transport phenomena, (2) a buffer region where the effect of both turbulent and molecular viscosity are important, and (3) a turbulent core region where the effect of molecular viscosity can be ignored. The viscous sublayer is an extremely thin layer physically.

From White and Corfield[58], the velocity profile for each of the region is limited by the value of the dimensionless distance from the wall, y^+ , according to the law of the wall equation which is a logarithmic relationship. For $y^+ < 5$, the flow is in the viscous sublayer, for $5 < y^+ < 30$, the flow is in the buffer region and finally, the turbulent core region exists for $30 < y^+ < 1000$. In the generation of grid points, the y^+ plays a key role[19]. It was proposed by Pope[66], that the viscous effects can be considered up to $y^+ < 50$. By using this assumption, the grid points (mesh) in this region around the wall, can be a little coarse to save computational time. Using this near-wall flow feature, correct grid points are chosen in the region close to the wall.

Most researchers adopt this approach by utilizing the enhanced wall treatment method included in ANSYS Fluent® commercial code. ANSYS Fluent® contains subroutines that specifically solve this problem.

2.9.4 Interface Tracking Models

Visualizing the dynamic behavior of the boundaries or interfaces between fluid components is very crucial in multiphase flow studies. Special algorithms capable of tracking the interfaces between the fluid components are required to achieve this purpose. As far as multiphase flow simulation is concerned, three main interface tracking methods exist in the open literature[67], namely, Level Set (LS) Method[68], Volume of Fluid (VOF) Method[69], and Front Tracking (FT) Method[70]. Both the Volume of Fluid Method and the Level Set Method (LSM) are derived using one-phase formulation[67]. In this formulation, a marker or and indicator function, β, is introduced to indicate the phase change by one of the phases through the attachment of a marker on that phase.

$$\beta = \begin{cases} 1; & \text{fluid 1} \\ 0; & \text{fluid 2} \end{cases} \tag{2.62}$$

Thus, rather than having two sets of variables for each phase of the fluid mixture (as in two-phase formulation), the marker function marks the integration volume by a characteristic function and the conservation law for the two phases[71] results in one:

$$\frac{\partial \phi}{\partial t} + \nabla \cdot (\phi \mathbf{U}) = 0 \tag{2.63}$$

where ϕ is any given physical property (density) and can be expressed as:

$$\phi = \phi_1 \beta + (1 - \beta)\,\phi_2 \tag{2.64}$$

Hence, the complexity of the computation is significantly reduced when using the one-phase formulation for the multi-fluid problem.

According to Unverdi and Tryggvason[70], Gloth *et al.*[72] and Terashima and Tryggvason[73], the front tracking method (FTM) is restricted to changes in multiphase-fluid topologies in that a marked interface from an initial configuration is advected and the topology is kept in the course of the simulation. This method is not recommended in applications where there is significant amount of topological changes (breaking or merging of droplets) in the multiphase fluid flow.

Initially developed by Osher and Sethian[68], the level set method (LSM) defines the interface as the zero set[74][75] of isosurface or isocontour of the given scalar field. This level set method was adopted in the simulation works of Lakehal *et al.*[71] and Sethian and Smereka[76]. A combination of Lagrangian marker particles and level set method was made by Enright *et al.*[77] to achieve and sustain a smooth geometrical description of the fluid interface. This semi-Lagrangian approach was used to improve the mass conservation. Analogous to the VOF method, LSM is also a one-fluid based formulation. The implicit material interface/boundary is provided by the zero set of the scalar field, ϕ:

$$\phi = \begin{cases} > 0; & \text{fluid 1} \\ < 0; & \text{fluid 2} \\ = 0; & \text{at the boundary } \Gamma \end{cases} \tag{2.65}$$

where $\Gamma : (x, y, z)|\phi(x, y, z) = 0\}$; ϕ is similar to the marker function, β except that here, the interface is defined at $\phi = 0$. To find the zero set, one has to extract isosurface or isocontour at a starting time. Usually, with volume faction, α dataset, the zero set is defined at the isosurface of $\alpha = 0.5$.

As given by Osher and Fedkiw[74], Enright *et al.*[77] and Lakehal *et al.*[71], the normal n, and the curvature κ, are expressed as:

$$n = \frac{\nabla \phi}{|\nabla \phi|} \tag{2.66}$$

$$\kappa = \nabla \cdot \frac{\nabla \phi}{|\nabla \phi|} \tag{2.67}$$

Usually, constraints are applied on the curvature and this should be done during physically correct simulation[67]. The universal concern of the curvature is the surface energy minimization. This method, however, finds majority of its applications in free surface flows.

Although LSM is a widely used method due to the simplicity in the mathematical formulation, volume is not always preserved during the interface advection[78][79]. The main setback is usually corrected through the application of volume correction after each numerical advection.

The volume of fluid method is one of the well-established interface volume tracking methods[80][81] which is currently in use. This method was developed by Hirt and Nichols[69]. The volume of each fluid phase is tracked with a sub-volume or sub-cell. Hence, this method is sub-cells or sub-volumes based and the volume percentage that one type of fluid takes up a sub-cell or sub-volume is tracked. VOF method is an Eulerian method of interface tracking which obeys the conservation of mass/volume. Unlike the FTM, VOF method can capture the topological changes of the moving surfaces, such as breaking up or merging of bubbles. As indicated earlier, the VOF method is derived from the one-phase formulation. A fraction variable, α, is defined as the integral of the marker function, β, in the control volume, V:

$$\alpha = \frac{1}{V} \int_V \beta\left(x, t\right) dV \tag{2.68}$$

where typically, the control volume, V is the computational cell volume. Also,

$$\begin{aligned} &\alpha = 0; && \text{fluid 1} \\ &\alpha = 1; && \text{fluid 2} \\ &0 < \alpha < 1; && \text{interface} \end{aligned} \tag{2.69}$$

For a given velocity field, $\mathbf{U}$, the transportation equation for the volume fraction is expressed as:

$$\frac{\partial \alpha}{\partial t} + \mathbf{U} \cdot \nabla \alpha = 0 \tag{2.70}$$

The VOF method also needs to approximate and reconstruct the interface at each time step. It preserves the volume accurately, however, maintaining the topology of the interface becomes difficult due to the process of interface reconstruction[67].

In addition to the above described interface or boundary tracking methods, there exist also research directions for material interface reconstruction. The main goal of the reconstruction methods is working on rebuilding continuous interfaces out of discrete pieces or piecewise functions, whereas the interface tracking methods focuses on tracking the dynamic behavior of the interface. Two main material researches exist in literature, namely, simple line interface (SLIC)[82] and piecewise linear interface construction (PLIC)[83].

2.10 Numerical Methods for Solving the Control Equations

The use of numerical simulations to solve a wide variety of fluid flow problems has become a common phenomenon. This is due to the complicated nature of practical problems in which analytical solutions are impossible and the increasingly number of computers available today. Generally, the governing equations for the physical processes are in the form of partial differential equations (PDEs). Two main approaches exist for the solution of these partial equations, namely, the Grid-based method (GBM) and the Particle-based method (PBM) as noted in the work of Chen and Hagen [67]. For the purpose of this study, only the GBM is described.

Under GBM, the PDEs governing the fluid flow are numerically solved on a fixed grid points. These equations are solved in using Euler approach. Thus, the propagation of the flow properties is computed on a fixed time independent grid.

In order to solve the governing equations, they need to be transformed or discretized into algebraic equations that can then be solved numerically using direct means (e.g. matrix inversion) or through iterative methods (Gauss elimination, Gauss-Seidel, Successive over-relaxation, etc.). For information on these solution method, please refer to Patankar[84].

2.10.1 Discretization Methods

Several discretization methods exist in literature, such as finite difference method (FDM), finite volume method (FVM) and finite element method (FEM). These techniques are usually developed to take the form of CFD codes to provide the solutions. Some of the well-known CFD code packages include ANSYS Fluent, TRAC, PHOENICS, FLOW 3D, NEKTON, FIDAP 8, MIXSIM, ICEPAK, COMSOL and OpenFOAM.

This study focuses on the FVM since this approach is mostly adopted in the multiphase flow applications. These methods are adopted to transform the governing equation into algebraic equations that can be solved numerically. More information on FDM and FEM discretization schemes can be found respectively in the works of Thomas and Trujillo[85] and Reddy[86]. This study adopts the FVM proposed by Patankar[84] which is commonly used by most CFD experts. It is what the ANSYS Fluent® commercial software uses.

The FVM transforms the governing equations into a system of algebraic equations by using a control volume approach. The differential equations are integrated over each control volume to produce discretized equations where each quantity is conserved on a control volume basis.

2.11 Convergence Criteria

Three main convergence criteria often adopted for CFD simulations include, residual values, solution imbalances and quantities of interest[87]. During a typical CFD simulation, these three parameters are monitored to assess the convergence of the CFD analysis.

Monitoring the values of the residuals is one of the basic ways to measure the convergence of an iterative solution. This is because the errors in the solution of the system of equations are directly quantified by the residuals. The residuals determine the imbalances of the conserved variables in each control volume. Since in a numerical solution (using iterative method), the residual never gets to zero, a minimum value must be set. The smaller the residual, the more accurate the solution is numerically. The default setting of the residuals in ANSYS Fluent® commercial code is 0.001. This value can however be reduced to obtain the desired degree of accuracy. However, in a very complicated problem analysis, attaining a very small residual can be challenging[87].

The solution imbalances can also be monitored for convergence. Ensuring that the conservation equations (mass, momentum, etc.) are indeed conserved at the end of the solution is an effective way to measure CFD convergence. These imbalances should be sufficiently small (approximately zero) before considering a solution to be conserved. Most authors ensure solution imbalances of smaller than 0.1%.

Making sure that there are no changes in the quantities of interest is a good practice to consider the convergence of a CFD solution. Usually in two-phase flow simulations, the quantities of interest include, liquid hold-up, pressure drop, mass flow rate, etc. Monitoring these quantities can help determine the convergence of the solution.

2.12 Summary

A review of commonly adopted CFD techniques to two-phase modeling and study of flow reversal and liquid loading is presented. Although not much information directly applies to the study of liquid loading phenomena, the combined knowledge presented here can be used to successfully model liquid loading phenomena. Most of the techniques presented indicate that the choice of the various models (turbulence, interface tracking, near-wall treatment, surface tension, drag, etc.) play an important role in the modeling process. The wrong choice could lead to wrongful numerical procedure and lead to wrongful results. The consumption of high computational resources must also be considered in the selection of the models for the simulation.

In most of the studies, the gas velocity corresponding to the minimum pressure gradient in the flow is taken as the critical gas velocity and its analysis is usually based on the liquid droplets. To the best of the author's knowledge, no direct application of CFD techniques based on the liquid film behavior (film reversal) has been used to study the liquid loading phenomena.

CHAPTER 3

PROBLEM STATEMENT AND METHOD OF SOLUTION

3.1 Statement of Problem

Considering the case of an annular flow through a vertical pipe in which the task is to model the liquid film in order to predict the initiation of liquid film reversal which would eventually lead to liquid loading. Figure 3.1 shows a schematic of the flow field in which gas flows in the core region surrounded by a liquid film adjacent to the pipe wall. Liquid droplets may migrate from the liquid film to the gas core and also gas bubbles may take place in the liquid film. In this regime, both phases flow in the upward direction and it is called co-current flow regime.

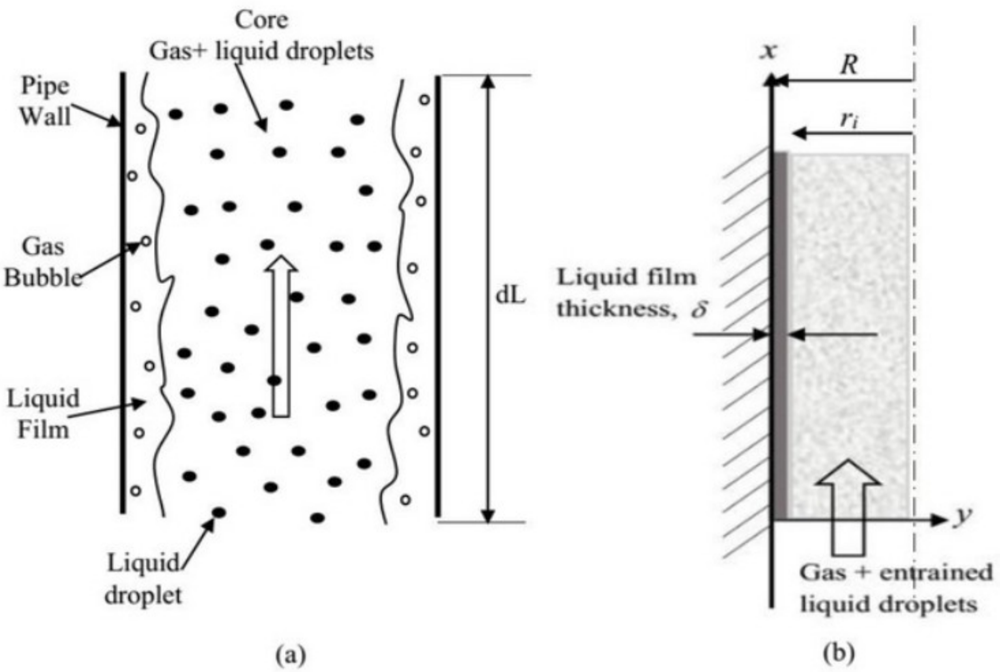

Figure 3.1: Schematic diagrams of the flow domain

3.1.1 Study Objectives

This study aims at utilizing computational fluid dynamics (CFD) techniques to:

1. Establish a computational model for two-phase annular flow and validation
2. Model the film flow along the pipe to predict the onset of film reversal in a vertical pipe
3. Obtain the velocity, shear stress and pressure drop variations in the flow

3.2 Governing Equations and Assumptions

3.2.1 Model Assumptions

The main assumptions made in this study include:

1. The flow is axisymmetric, adiabatic and incompressible
2. The net mass transfer between the two phases is zero
3. The flow is transient and solution continued until reaching quasi-steady state
4. The flow is turbulent in both phases
5. No source terms (in the form of heat source etc) are added

3.2.2 Governing Equations

This study adopts the Eulerian Multi-Fluid model presented in ANSYS Fluent® commercial code version 16.1 as described in the previous chapter to solve the problem due to associated advantages over the other models. Simplifying equations (2.22) and (2.23) using the model assumptions ($\dot{m}_{pq} - \dot{m}_{qp} = 0$, $S_q = 0$, $\mathbf{F}_{lift,q} = \mathbf{F}_{wl,q} = \mathbf{F}_{vm,q} = \mathbf{F}_{td,q} = 0$), the main governing equations which are the independent mass and momentum conservation equations are simplified and presented below for the liquid phase. Similar equations exist for the gas phase.

1. Mass Conservation

$$\frac{\partial}{\partial t}(\alpha_L \rho_L) + \nabla \cdot \big(\alpha_L \rho_L \mathbf{U}_L\big) = 0 \tag{3.1}$$

2. Momentum Conservation

$$\frac{\partial}{\partial t}\big(\alpha_L \rho_L \mathbf{U}_q\big) + \nabla \cdot \big(\alpha_L \rho_L \mathbf{U}_L \mathbf{U}_L\big) = -\,\alpha_L \nabla p + \nabla \cdot \bar{\bar{\tau}}_L + \alpha_L \rho_L g + \mathbf{R}_{GL} + \mathbf{F}_{CSF} \tag{3.2}$$

where $\bar{\bar{\tau}}_L$ is liquid phase stress-strain tensor which is expressed as:

$$\bar{\bar{\tau}}_L = \alpha_L \mu_L \Big(\nabla \mathbf{U}_L + \nabla \mathbf{U_L}^T\Big) + \alpha_L \bigg(\lambda_L - \frac{2}{3}\mu_L\bigg) \nabla \cdot \mathbf{U}_L \bar{\bar{I}} \tag{3.3}$$

where the subscript L represents the liquid phase; $\mathbf{U}$ is the flow velocity; α is the volume fraction; $\mathbf{F}_{CSF}$ is the continuum surface force (external body force); $\mathbf{R}_{GL}$ is an interaction between phases (gas and liquid); and p is the pressure shared by the two phases. From equation (2.28), $\mathbf{R}_{GL}$ can be written as:

$$\mathbf{R}_{GL} = K_{GL}\left(\mathbf{U}_G - \mathbf{U}_L\right) \tag{3.4}$$

where, K_{GL} which is the interphase momentum exchange coefficient is computed using the relation:

$$K_{GL} = \frac{\alpha_L \alpha_G \rho_G}{\tau_G} f \tag{3.5}$$

where subscript G, represents the gas phase; τ_G is the particulate relaxation time which is expressed in equation (2.30); f is the drag function (equation (2.31)) which is obtained from available drag models as described in the previous chapter.

Some of these drag models are made available in ANSYS Fluent® commercial code.

3.2.3 Turbulence Modeling

High turbulence usually exist in both phases due to the high velocity gradients at the interface between the two phases in free surface flows when differential eddy viscosity models are used[51]. Among the available turbulence models described in the literature, the standard $k-\varepsilon$ turbulence model available in ANSYS Fluent® is chosen for this study. This model is applicable to fully turbulent flow which makes it suitable for the current study for the range of flow rates to be used. All this model was found to be more stable for the current study. Given below are the transport equations describing the the selected turbulence model (standard $k-\varepsilon$ model):

$$\frac{\partial}{\partial t}(\rho k) + \frac{\partial}{\partial x_i}(\rho U_i k) = \frac{\partial}{\partial x_j}\left[\left(\mu + \frac{\mu_t}{\sigma_k}\right)\frac{\partial k}{\partial x_j}\right] + G_k + G_b - \rho\varepsilon - Y_M + S_k \quad (3.6)$$

and

$$\begin{aligned}\frac{\partial}{\partial t}(\rho \varepsilon) + \frac{\partial}{\partial x_i}(\rho U_i \varepsilon) =& \frac{\partial}{\partial x_j}\left[\left(\mu + \frac{\mu_t}{\sigma_\varepsilon}\right)\frac{\partial \varepsilon}{\partial x_j}\right] \\ &+ C_{1\varepsilon}\frac{\varepsilon}{k}(G_k + C_{3\varepsilon}G_b) - C_{2\varepsilon}\rho\frac{\varepsilon^2}{k} + S_k\end{aligned} \quad (3.7)$$

In the above equations, G_k is the generation of turbulence kinetic energy due to the mean velocity gradients; G_b is the generation of turbulence kinetic energy due to buoyancy; Y_M is the contribution of the fluctuating dilatation in compressible turbulence to the overall dissipation rate; $C_{1\varepsilon}$, $C_{2\varepsilon}$ and $C_{3\varepsilon}$ are constants; σ_k and σ_ε are the turbulent Prandtl numbers for k and ε respectively; S_k and S_ε are user-defined source terms. The following values were utilized for the constants, $C_{1\varepsilon} = 1.44$, $C_{2\varepsilon} = 1.92$, $\sigma_k = 1.0$ and $\sigma_\varepsilon = 1.3$. The turbulent viscosity, μ_t in the standard $k - \varepsilon$ as described in the previous chapter is computed using the relation:

$$\mu_t = \rho C_\mu \frac{k^2}{\varepsilon} \tag{3.8}$$

where C_μ is a constant and is assigned $C_\mu = 0.09$, in the current study.

3.2.4 Near-Wall Treatment

Adopting the standard $k - \varepsilon$ turbulence model requires special treatments for the flows at regions near the pipe wall to make it applicable since this model is basically applicable to turbulent core flows as described in the literature. Pope[66] proposed that the viscous effects can be considered up to $y^+ < 50$. This assumption is adopted for the generation of the finite-volume grid in the current study so as to save computational time. In ANSYS Fluent® commercial code, the near-wall treatment is utilized through the enhanced wall treatment option.

3.2.5 Surface Tension Model

Surface tension is an important parameter which results from the sharp changes in the molecular forces of attraction at the two-phase interface due to the discontinuous changes in properties. Usually, in complex geometry, modeling this local force becomes a stressful task. In this study, the continuum surface force (CSF) model derived by Brackbill *et al.*[65] which is available in ANSYS Fluent® code, is utilized to model the surface tension due the fact that in this study, the surface tension is assumed constant. Since this study considers only two phases, this force can be computed using the relation:

$$F_{CSF} = \sigma \frac{\rho_{LG} \kappa_L \nabla \alpha_L}{\frac{1}{2}\left(\rho_L + \rho_G\right)} \tag{3.9}$$

where κ as explained in the previous chapter is the local curvature of the interface, σ is the coefficient of surface tension.

3.2.6 Interface Tracking Modeling

The interface between the two phases is tracked by solving a volume fraction (α), continuity equation for the liquid phase. The equation is expressed as follows:

$$\frac{\partial \alpha_L}{\partial t} + \nabla \cdot (\alpha_L \mathbf{U}) = 0 \tag{3.10}$$

For $\alpha_L = 1$ implies the liquid phase zone, $\alpha_L = 0$ implies the gas phase zone and for $0 < \alpha_L < 1$ implies the interface. The volume fraction of the gas phase (void fraction), α_G, is solved using the equation below:

$$\alpha_G = 1 - \alpha_L \tag{3.11}$$

3.2.7 Interfacial Drag Modeling

Out of the drag models described in the literature, the Schiller and Naumann drag model available in ANSYS Fluent® code is adopted for this study based on its application as highlighted in chapter 2. This model has been found to be very successful in a wide range of multiphase flow applications as found in the works of Besagni *et al.*[88], Kabanda and Wang[89] and others. According to Schiller and Naumann[53], the drag coefficient, C_D, found in equation (2.31) can be computed using the relation:

$$C_D = \begin{cases} \frac{24\left(1+0.15Re^{0.687}\right)}{Re}; & Re \leq 1000 \\ 0.44; & Re > 1000 \end{cases} \tag{3.12}$$

Substituting the results from equations (3.12) and (2.32) into equation (2.31), the drag function can be obtained.

3.3 Computational Domain and Mesh

Both the geometry and the mesh for this study were constructed using the Gambit software. Since the flow is axisymmetric, only half of the pipe domain is considered in the simulation work so as to save computational time as shown in Figure 3.2a. It should be noted that the computational domain shown in Figure 3.2 is not drawn to scale. The computational domain is a vertical pipe of diameter, D, and length, L. The domain is bounded by the pipe axis, two velocity inlet sections (liquid and gas inlets), a pressure outlet and a pipe wall. The pipe diameter, D, is set to be 76.2 mm, the pipe length, L, is set to be 3000 mm in order to attain hydrodynamically fully developed flow and to help obtain results for validation against the experimental data of Guner[17]. The width of the liquid inlet is set to 20 mm to avoid jet flow at the inlet. A section of the pipe is shown in Figure 3.2b to illustrate the type of finite volume (FV) mesh utilized. The mesh is made dense closed to the pipe wall in order to capture the physical phenomena at the liquid film region and the interface between the liquid and the gas. The mesh, however, is made coarser towards the pipe axis so as to save computational time. The grid transition rate utilized in this study is 1.15 with an aspect ratio of less than 4. Three different meshes (mesh 1, mesh 2 and mesh 3) were tested for grid

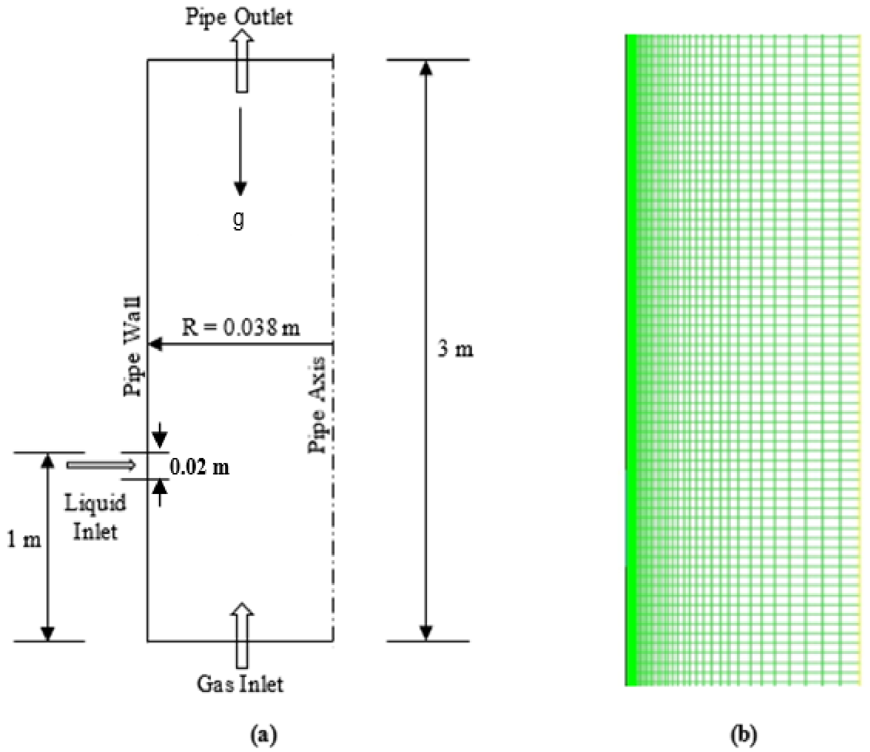

Figure 3.2: Schematic diagram of the flow domain (a) and FV mesh (b)

independency test. Details are presented in Table 3.1.

Table 3.1: Mesh sizes tested

Mesh	**Number of Nodes**
1	51,591
2	99,921
3	137,016

Liquid film thickness distributions were measured for all the three meshes and compared to demonstrate grid independence. There was little difference between mesh 2 and 3. Hence, mesh 2 is selected for this study.

3.4 Initial and Boundary Conditions

3.4.1 Initial Conditions

Initially ($t = 0$), the pipe is filled with the gas phase at the input flow rate surrounded by a film of liquid on the pipe wall. The liquid phase which enters through the side of the pipe wall at a constant input velocity ensures the continuous formation of the liquid film on the pipe wall. The pressure is set to be 1 atm.

3.4.2 Boundary Conditions

Based on the analysis in this study, velocity inlet boundary conditions were applied to both the liquid and gas inlets; a pressure outlet boundary condition is applied to the pipe outlet; the pipe axis is set to be axisymmetric boundary and a no-slip boundary condition is applied to the pipe wall. The flow inputs for the both the gas and the liquid phases are computed using the following relations:

$$U_L = \frac{U_{SL} A_P}{A_L} \tag{3.13}$$

$$U_G = \frac{U_{SG} A_P}{A_G} \tag{3.14}$$

where U_L and U_G are the liquid and gas phase input velocities respectively; U_{SL} and U_{SG} are the superficial liquid and gas velocities respectively; A_L and A_G are the input cross-sectional areas of the liquid and the gas phase respectively; and A_P is the cross-sectional area of the pipe.

3.5 Test Matrix

The data utilized in this study is based on the experimental work of Guner[17]. Air and water are used as the phase fluids for the simulation. Properties of these fluids are provided in Table 3.2.

Table 3.2: Phase properties for the simulation

Phase	**Type**	**Density** [kg/m^3]	**Viscosity** [kg/(m s)]
Air	Primary	1.225	1.8×10^{-5}
Water	Secondary	998.2	1.0×10^{-3}

The input superficial gas velocities (U_{SG}) range from approximately 38 m/s to approximately 18 m/s and the superficial liquid velocities (U_{SL}) range from 0.10 m/s to 0.01 m/s as indicated in Table 3.3. These input values were chosen to conform with the data points of Guner[17] in order to allow validation of the model.

Table 3.3: Test matrix for current simulation

Case	**1**	**2**	**3**	**4**	**5**	**6**
			$\mathbf{U_{SL}} = \mathbf{0.10}$ m/s			
$\mathbf{U_{SG}}$ [m/s]	36.77	31.77	27.64	23.99	21.17	18.03
			$\mathbf{U_{SL}} = \mathbf{0.10}$ m/s			
$\mathbf{U_{SG}}$ [m/s]	36.77	32.92	27.79	23.77	21.77	19.11
			$\mathbf{U_{SL}} = \mathbf{0.10}$ m/s			
$\mathbf{U_{SG}}$ [m/s]	37.60	33.00	29.74	24.23	22.33	19.96

The simulation is conducted such that for a given constant flow input of liquid phase, the superficial gas velocity is gradually reduced until onset of liquid film reversal is observed. Shown in Figure 3.3 is the test matrix for a 3-in pipe diameter on a flow pattern map using two models, one by Barnea[90] and the other by Taitel[9].

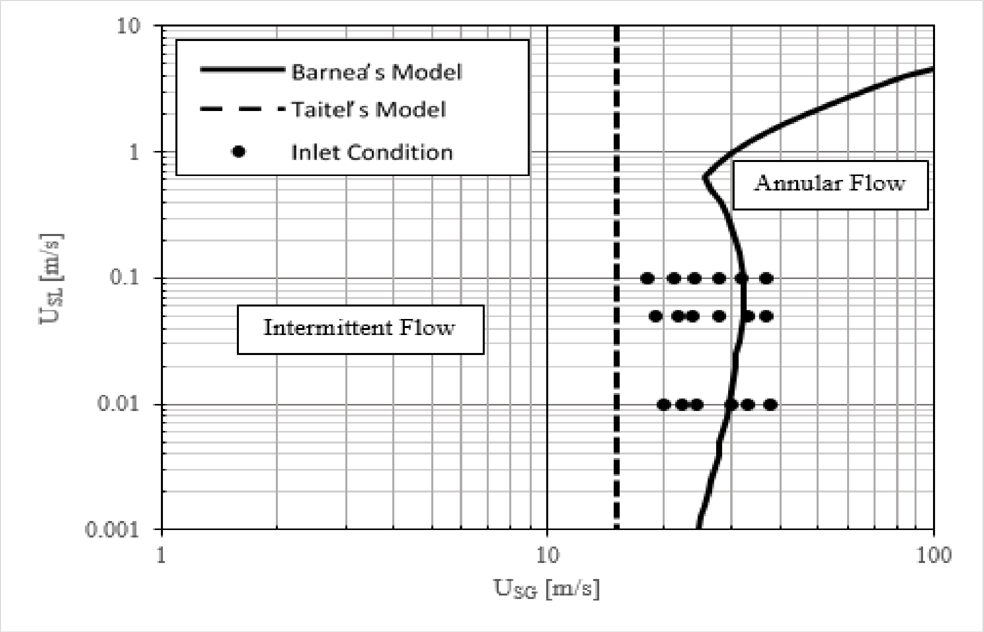

Figure 3.3: Test matrix on flow pattern map using Barnea's and Taitel's models

3.6 Convergence Criteria

In order to reach convergence, residuals were monitored for axial velocity (u), radial velocity (v), turbulent kinetic energy (k), kinetic energy dissipation rate (ε), and mass imbalance. In addition to the above, the liquid volume fraction and void fraction were also monitored at some cross-sections to ensure they reach constant values when the simulation converges.

3.7 Solution Algorithm

The simulation of the two-phase flow is carried out using the two-fluid model found ANSYS Fluent® 16.1 software. This software uses the finite volume discretization scheme for the model formulation. The Eulerian-Eulerian Multi-Fluid VOF scheme in Fluent® permits the option of using the sharpening schemes such as Geo-Reconstruct, CICSAM and compressive models, necessary to track the interface between the two phases accurately. This model when used, overcomes some of the flaws of the VOF scheme as a result of the shared velocity and temperature formulations[51][26]. Hence, its adoption for the current study. This is because a set of Navier-Stokes equations (NSEs) is solved for each phase involved. The outline below is the summary of the solution procedure used.

1. A transient solver using an implicit time step size of 0.0001 s is employed.
2. Simulation was carried out adopting Eulerian-Eulerian Multi-Fluid VOF model.

3. Phase coupled SIMPLE scheme was used for the pressure velocity coupling.

4. For the spatial discretization schemes, the following were used:

    I Least squares cell based for gradient

    II Second order upwind for momentum, turbulent kinetic energy and turbulent dissipation rate.

    III Modified HRIC scheme is used for the Volume Fraction.

    IV First order implicit was used for the transient formulation

5. Scaled absolute values of the residual of the calculated variables were monitored and convergence criterion set to 10^{-3}.

CHAPTER 4

RESULTS AND DISCUSSION

4.1 Mesh Independency Test

As described in the previous chapter, three different finite-element meshes were studied as detailed in Table 3.1. The dynamic liquid film thicknesses (δ) calculated using isosurface values of constant volume fraction of 0.5 as the interface were compared when the flow reached quasi-steady state for a section in the flow domain located at $x = 2.5 - 2.70$ m. At that state, the mass imbalance was less than 5% as shown in Figure 4.1.

Figure 4.2 shows the dynamic film thickness distribution in the flow domain for the mesh independency test. A similar approach was utilized by Chen[51]. The results indicate that mesh 2 and mesh 3 have almost same liquid film wave fluctuation. Hence, mesh 2 is adopted in the current study to reduce computer time.

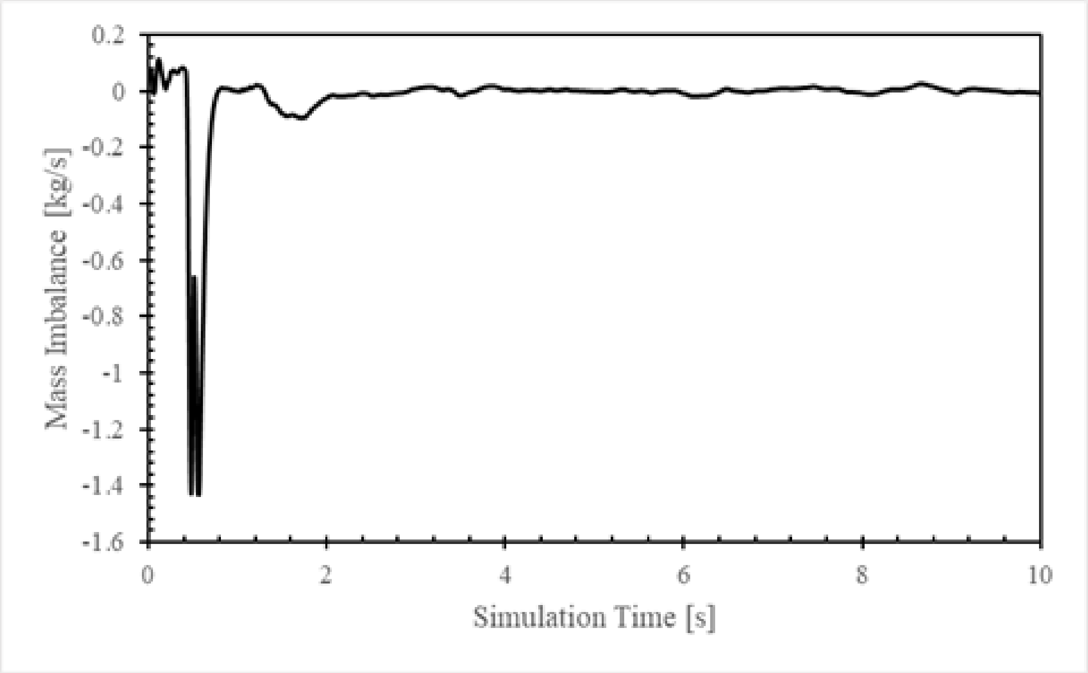

Figure 4.1: Time variation of the calculated mass imbalance for the case of $U_{SL} = 0.05$ m/s and $U_{SG} = 21.77$ m/s

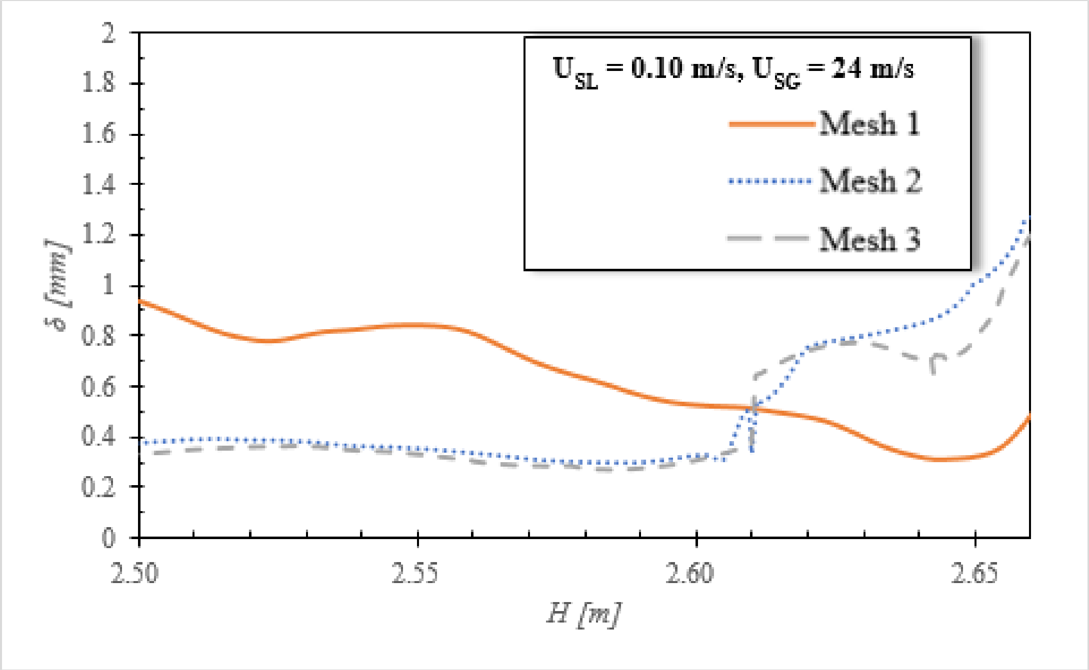

Figure 4.2: Variation of liquid film thickness with mesh types for a section ($x = 2.5 - 2.7$ m) in the flow domain

4.2 Time Step Independency Test

In order to select a time step size (Δt) capable of providing a more accurate results, four different time step sizes were studied and the resulting time averaged liquid (water) holdup were compared with the available experimental data. In this test, the time-averaged liquid holdup (H_L) was calculated for the case of superficial gas velocity of 36.77 m/s and superficial liquid velocity of 0.10 m/s. The computational simulation continued for 1s for different time steps and the obtained results for H_L were compared to the data stated in the experimental work by Guner[17] who reported a liquid holdup of 0.0165 as shown in Table 4.1. The results show that the choice of time step size can significantly affect numerical accuracy. The results shown in Table 4.1 indicate that more accurate results are obtained using smaller time steps. The time step size of 0.0001 s was selected for this study due to computational time limitation.

Table 4.1: Variation of liquid holdup with different time steps (Δt)

$\Delta t[s]$	$\mathbf{H_L}$ **[-]**	**Error [%]**	**Simulation Time [minutes]**
0.01	0.0474	187.27	12
0.001	0.0315	90.91	1,184
0.0001	0.0187	13.33	2,656
0.00001	0.0171	3.63	5,111

4.3 Model Validation

In order to test the accuracy of the present 2D axisymmetric numerical model, some of the results were compared with the corresponding experimental data obtained by Guner[17]. The experiments were conducted at an average operating pressure of 1 bar at adiabatic conditions, with superficial gas velocities ranging from approximately 2 m/s to 40 m/s and superficial liquid velocities ranging from 0.01 m/s to 0.10 m/s in a 76.2 mm pipe. It should be noted that only the data from the vertical pipe orientation is considered in this study for superficial gas velocities ranging from approximately 18 m/s to 37 m/s. The test matrix for the current study is presented in Table 3.3. The test section of the pipe is approximately 16.46 m (54 ft) long in the experimental setup. In order to minimize computational time and also ensure hydrodynamically fully developed flow, only length of 3 m was considered in this study. Pressure gradients measurements from the experiments were compared to that predicted by the model developed in this study as shown in Figure 4.3.

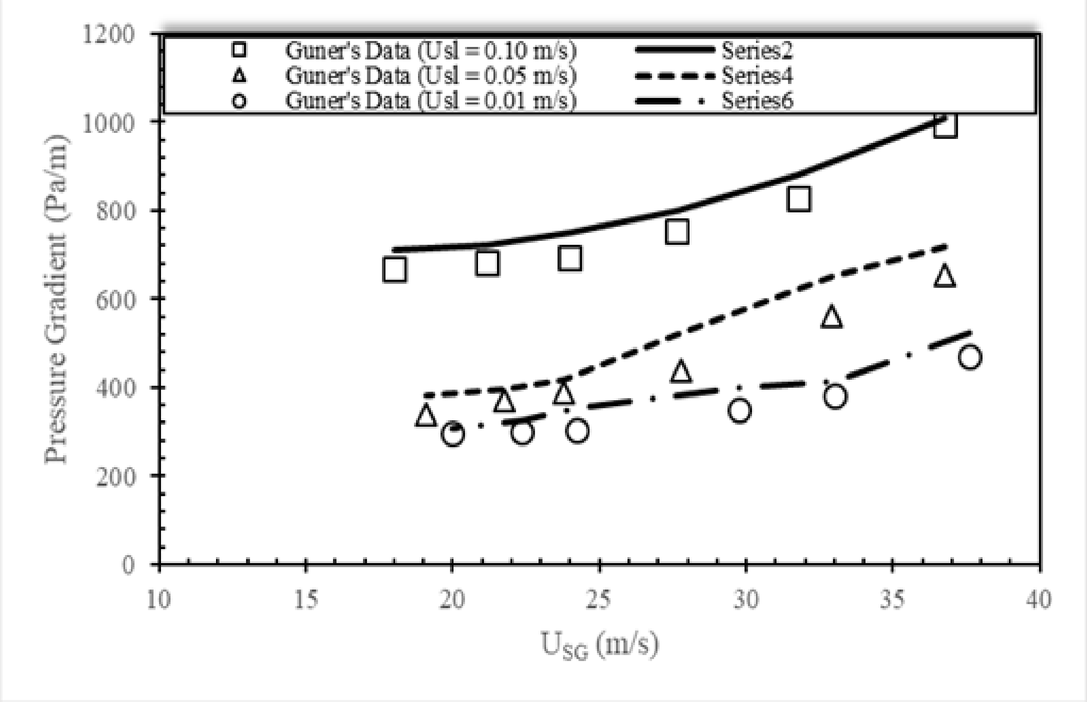

Figure 4.3: Variation of pressure gradient with superficial gas velocity

Three different superficial liquid velocities (0.10 m/s, 0.05 m/s and 0.01 m/s) were simulated, maintaining each superficial liquid velocity constant while gradually reducing the superficial gas velocity in each simulation as shown in the test matrix in Figure 3.3. As can be seen in Figure 4.3, pressure gradient measurements by the model are in good agreement with the experimental data.

4.4 Critical Superficial Gas Velocities ($U_{SG,cr}$)

The computational simulation of the phenomenon of liquid film reversal started by considering a liquid film flowing upward adjacent to the pipe walls with a constant superficial liquid velocity (U_{SL}) together with a very high superficial gas velocity (U_{SG}) in the core region. The gas velocity, U_{SG} , is then gradually reduced at small intervals until part of the liquid film reverses its flow direction and starts to move downwards. This moment refers to the phenomenon of film reversal and the corresponding U_{SG} is called the critical superficial gas velocity ($U_{SG,cr}$). It should be noted here that the critical superficial gas velocities computed in this study, refer to those velocities corresponding to the beginning of liquid film reversal. $U_{SG,cr}$ is computed for the three different superficial liquid velocities (0.10 m/s, 0.05 m/s and 0.01 m/s) utilized in this study. In the experiments, the film reversal initiation was identified through visualization of change in direction by the liquid film through high speed videos. In the numerical simulations, a similar approach is observed where the beginning of liquid film reversal was identified by close inspection of the flow pattern variation and gestured by the manifestation of local downward liquid velocities in the neighborhood of the pipe walls. This phenomenon is referred to as the onset of liquid film reversal or simply film reversal. Figure 4.4 shows a comparison between the critical gas velocities predicted by the model at different superficial liquid velocities and the experimental results reported in the work by Guner[17].

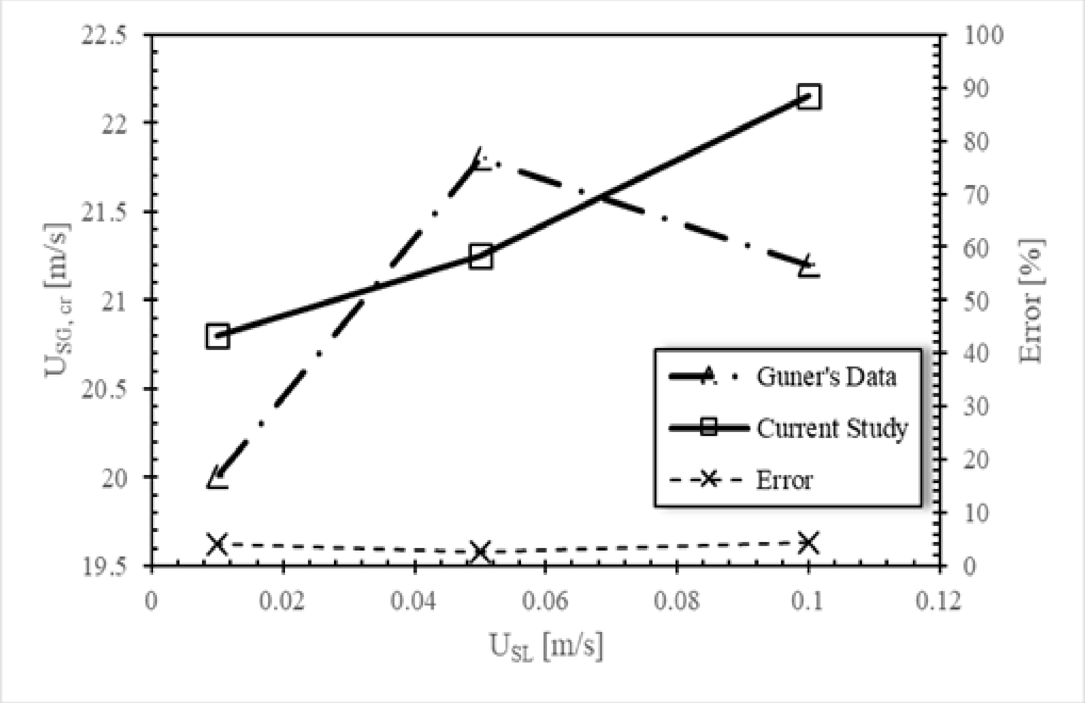

Figure 4.4: Critical superficial gas velocities for three superficial liquid velocities and comparison with experimental results reported by Guner[17]

The figure shows a good agreement with a maximum difference of 4.48% between the computed and measured critical gas velocities. This difference is considered very small and may be attributed to the identification of the beginning of liquid film reversal and may also be due to the mode of liquid injection into the flow domain in the computational model. In the experiments, the air and water enter the test section through a mixing tee while the water enters in this study through pipe wall section with air is injected from below. The mode by which the liquid phase is introduced into the channel can significantly affect the results as observed in the works of Hewitt and Hall-Taylor[3].

4.5 Typical Flow Field

The streamlines inside the air and water phases for a superficial liquid velocity of 0.10 m/s and superficial gas velocities of 31.77 m/s 18.03 m/s downstream of the liquid inlet section is presented in Figure 4.5a and 4.5b respectively to show the characteristics of the flow field. Both Figure 4.5a and Figure 4.5b show a typical annular flow pattern.

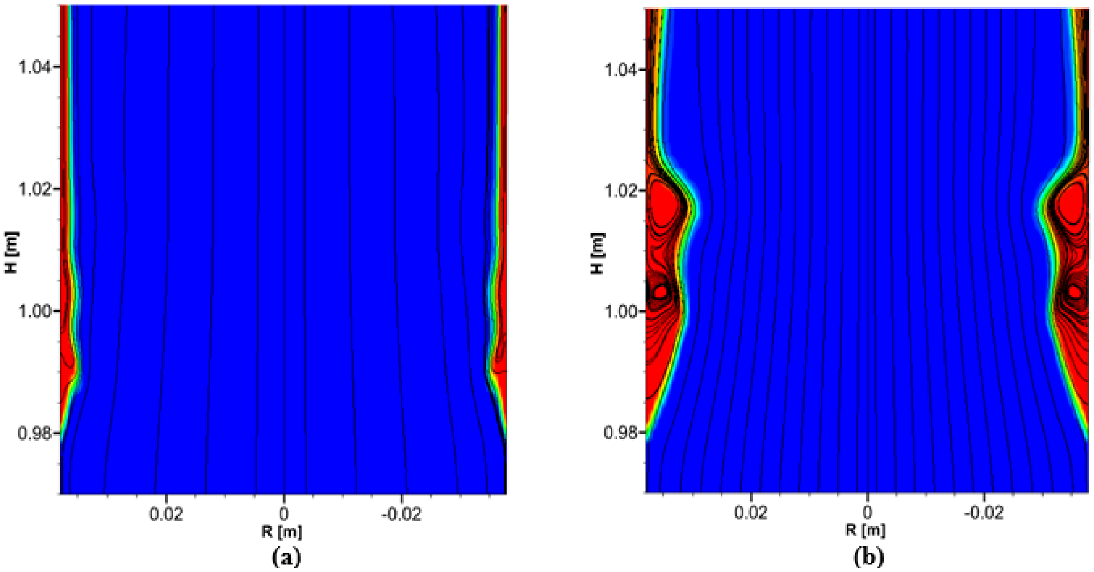

Figure 4.5: Typical flow field: a) higher U_{SG} ($U_{SG} = 31.77$ m/s) and b) lower U_{SG} ($U_{SG} = 18.03$ m/s) at $U_{SL} = 0.1$ m/s,

However, Figure 4.5b shows some film reversal condition at the pipe wall which could present some intermittent flow (as observed in the flow pattern in Figure 3.3 using the model by Barnea[90]). It can be seen that when the amplitude of the forming wave at the liquid inlet section reaches its maximum value, it starts to move upwards. In Figure 4.5a, the liquid phase travels as thin film and it is carried out of the pipe due to the higher gas velocity (31.77 m/s) resulting in an annular flow pattern. The waves in this flow pattern tend to be flatter. All simulated cases with comparatively high gas velocities show that all the liquid film moves upward out of the pipe. As the superficial gas velocity reduces to 18.03 m/s, the shear force imparted on the liquid film by the gas phase becomes insufficient to carry the liquid phase to the pipe exit section while keeping complete upward liquid film movement. As a result, the liquid film thickens, thus producing a circulatory flow region in the liquid phase causing part of the liquid film to move downward near the pipe wall. This is accompanied by the formation of flooding waves that have higher frequencies and tend to cause the continuous throwing of the liquid phase (water) in the region located above the liquid inlet section. In all the simulated cases with gas velocities below the critical superficial gas velocities, part of the liquid film flows downwards periodically.

In their work, Da Riva and Del Col[25] reported that the gas flow velocity increases on the windward side of the wave and results in a flatter velocity profile at the crest followed by flow separation with large wake just after the wave crest.

4.6 Effects of Liquid and Gas Superficial Velocities

Three sets of results are presented. First, contour plots of the phase distributions in the pipe; second, plots of the streamlines and; finally, the velocity vectors in the flow field are provided for detailed visualization. In all the three sets, the pipe is divided into three regions (inlet region, middle region and upper region) for the visualization. To visualize the full pipe phase distributions, the divisions are as follows: inlet region (0.97 m to 1.6 m), middle region (1.6 m to 2.3 m) and upper region (2.3 m to 3.0 m). Considering air-water mixture for the current simulations, the phase distributions for various superficial velocities are provided when the flow reaches quasi-stable state.

The simulations captured some of the major characteristics of annular flow such as the development of instabilities on the interface between the liquid film and the gas core, the formation of large roll waves which causes most of the mechanisms attributed to the annular flow. However, the simulation was unable to capture the small air bubbles which are usually carried under into the liquid film and also the droplet deposition back into the liquid film.

However, to have a detailed view at the streamlines and the velocity vectors, the inlet, middle and outlet sections were redefined as follows: inlet section (0.97 m to 1.05 m), middle section (1.80 m to 1.88 m) and upper section (2.75 m to 2.83 m). Presented below are the results and the discussions.

The phase distribution is estimated by the volume fraction values where for this particular case, a volume fraction value of 0 means the fluid is gas (air) and a volume fraction value of 1 means the fluid is liquid. For volume fraction values between 0 and 1, the fluid is classified as a mixture. Three zones can be observed in the phase distribution contours; (1)the gas core zone, (2) zone of waves and liquid droplets and (3) the liquid film zone occupying the region from the pipe axis to the pipe wall as shown in Figures 4.6 and 4.7. For cases with sufficiently high superficial gas velocities (Figure 4.6a to 4.6d), the interfacial shear force is high enough to carry all the liquid phase upward as a smooth film of approximately uniform thickness adjacent to the pipe wall. In these cases, both phases flow in the same direction exhibiting upward co-current annular flow pattern. This is evident in the streamlines and velocity vectors presented in Figure 4.8, 4.10, 4.12 and 4.14. In this type of flow, a smooth continuous interface is observed separating the gas phase from the liquid phase and accompanied by a gradual reduction of the film thickness from the inlet section to the pipe outlet section.

As the superficial gas velocity is gradually reduced while maintaining a constant superficial liquid velocity, a point is reached where part of the liquid film on the pipe wall reverses direction from upward flow to downward flow as observed in Figure 4.9b, 4.11b, 4.13a and 4.15b. At this state, periodically large interfacial waves are seen dragging the liquid film upward causing oscillatory motion in the film. A falling liquid film can be seen in this type of flow. This is a typical feature of churn flow[3][6][91]. This usually marks the onset of liquid film reversal which will gradually lead to complete liquid film reversal when the superficial gas velocity is further reduced below a critical value. In this simulation, the superficial gas velocity corresponding to the onset of film reversal for a constant superficial liquid velocity of 0.10 m/s lies between 23.99 m/s and 18.03 m/s. This corresponds to the value of 21.2 m/s obtained by Guner[17] in her experimental study.

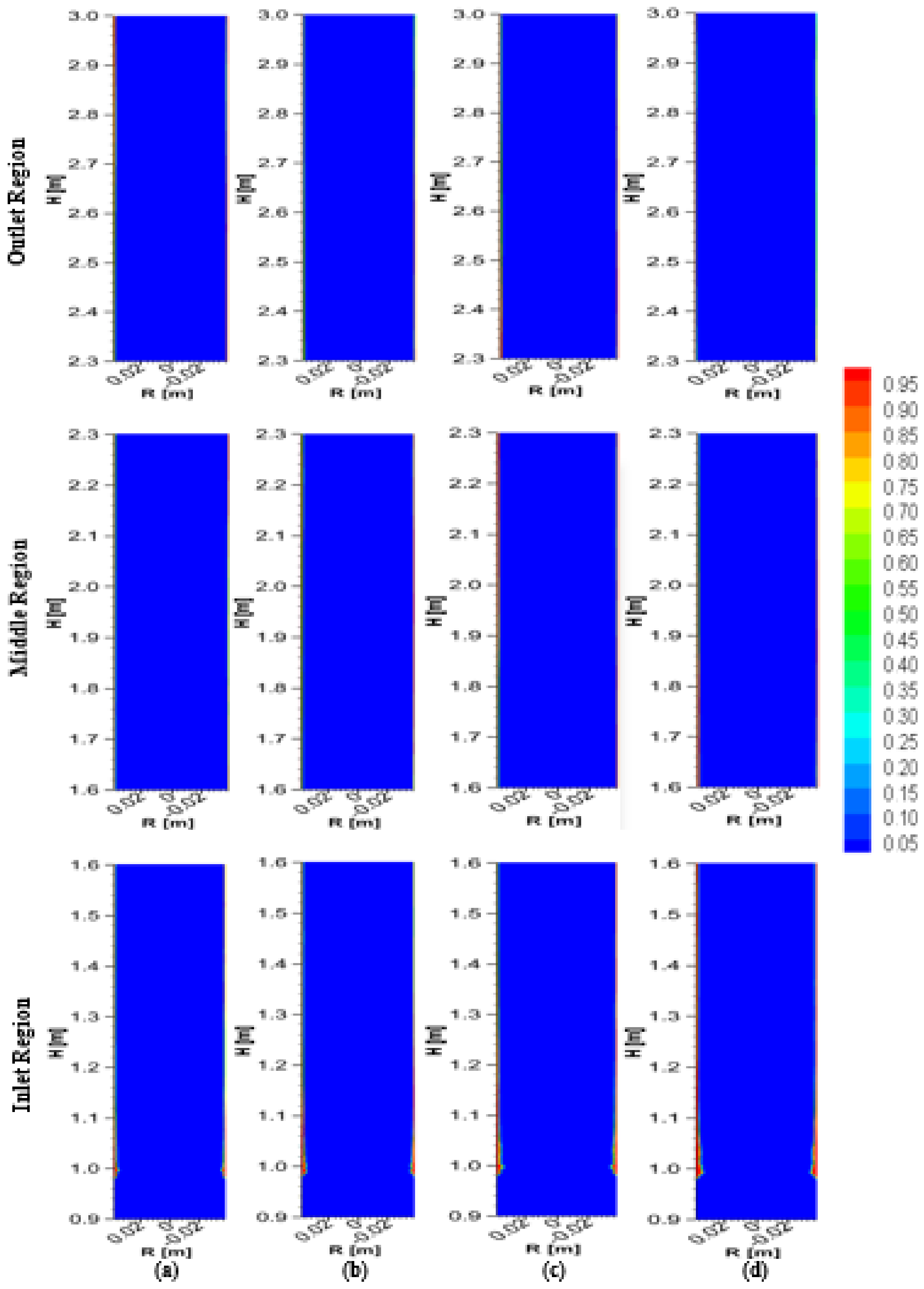

Figure 4.6: Phase distribution for the case of $U_{SL} = 0.10$ m/s and varying U_{SG}: a) case 1, b) case 2, c) case 3 and d) case 4

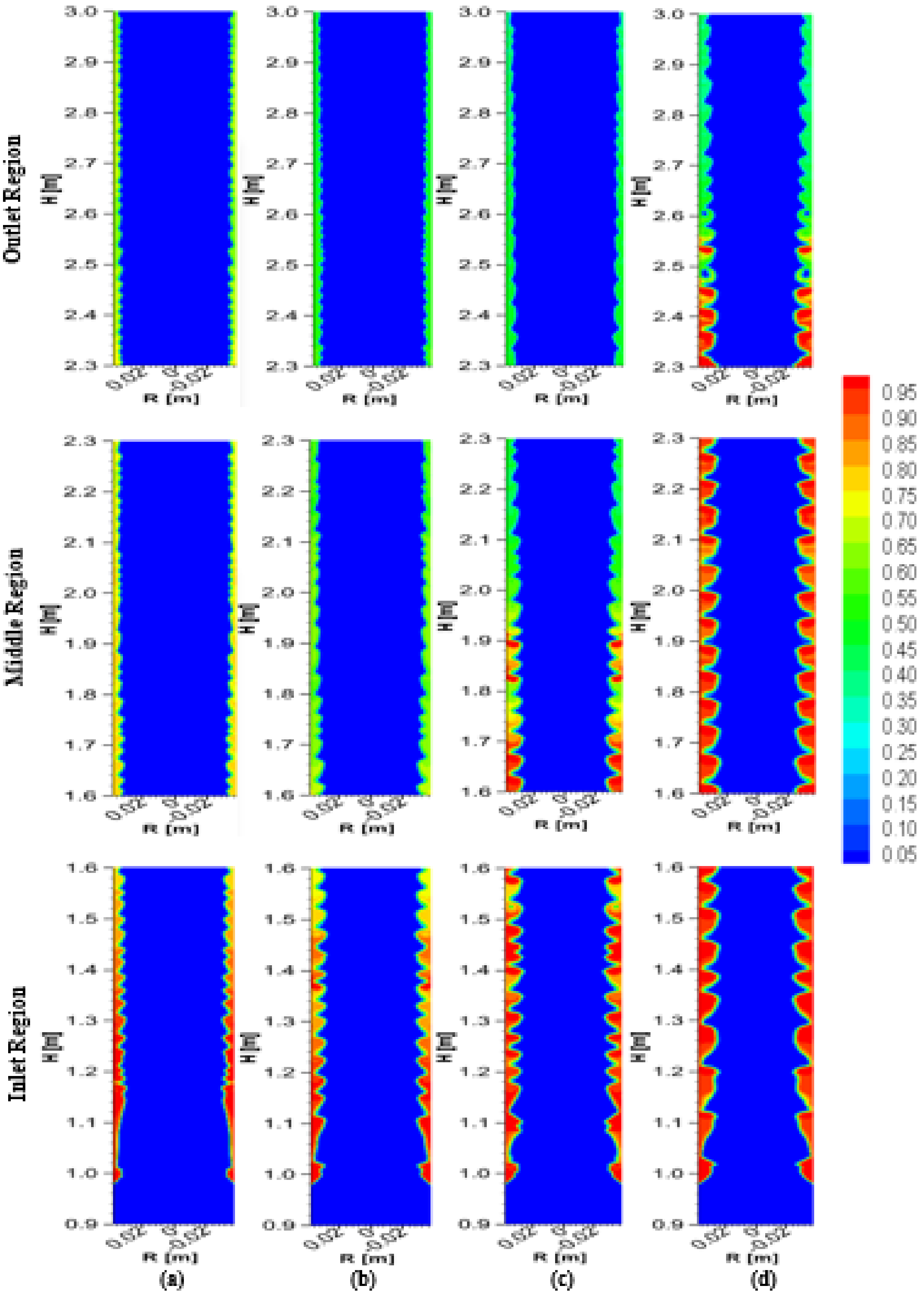

Figure 4.7: Phase distribution for the case of $U_{SL} = 0.10$ m/s and varying U_{SG}: a) case 5, b) case 6, c) $U_{SG} = 16.01$ m/s and d) $U_{SG} = 13.46$ m/s

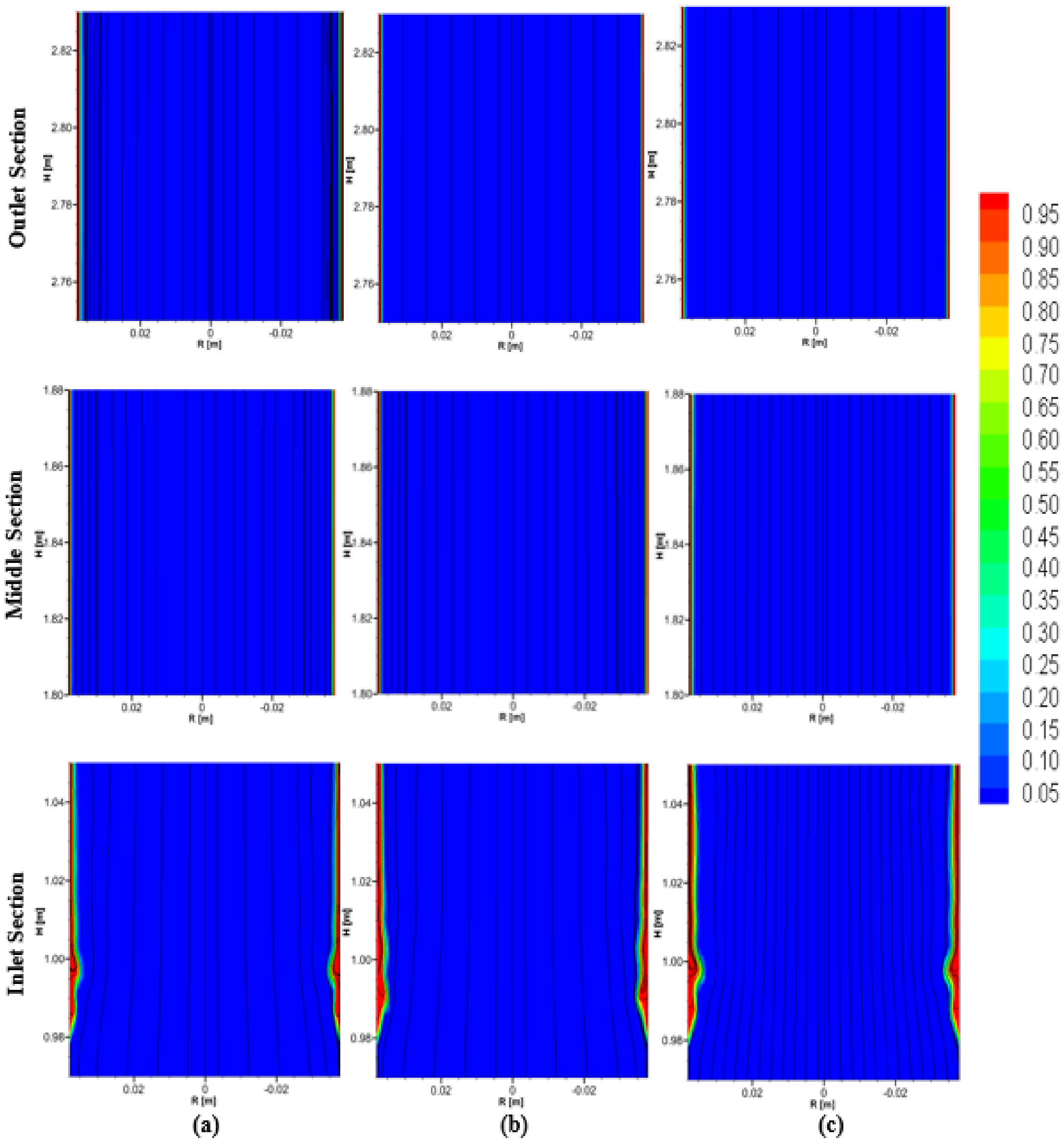

Figure 4.8: Stream traces for the case of $U_{SL} = 0.10$ m/s and varying U_{SG}: a) case 1, b) case 2 and c) case 3

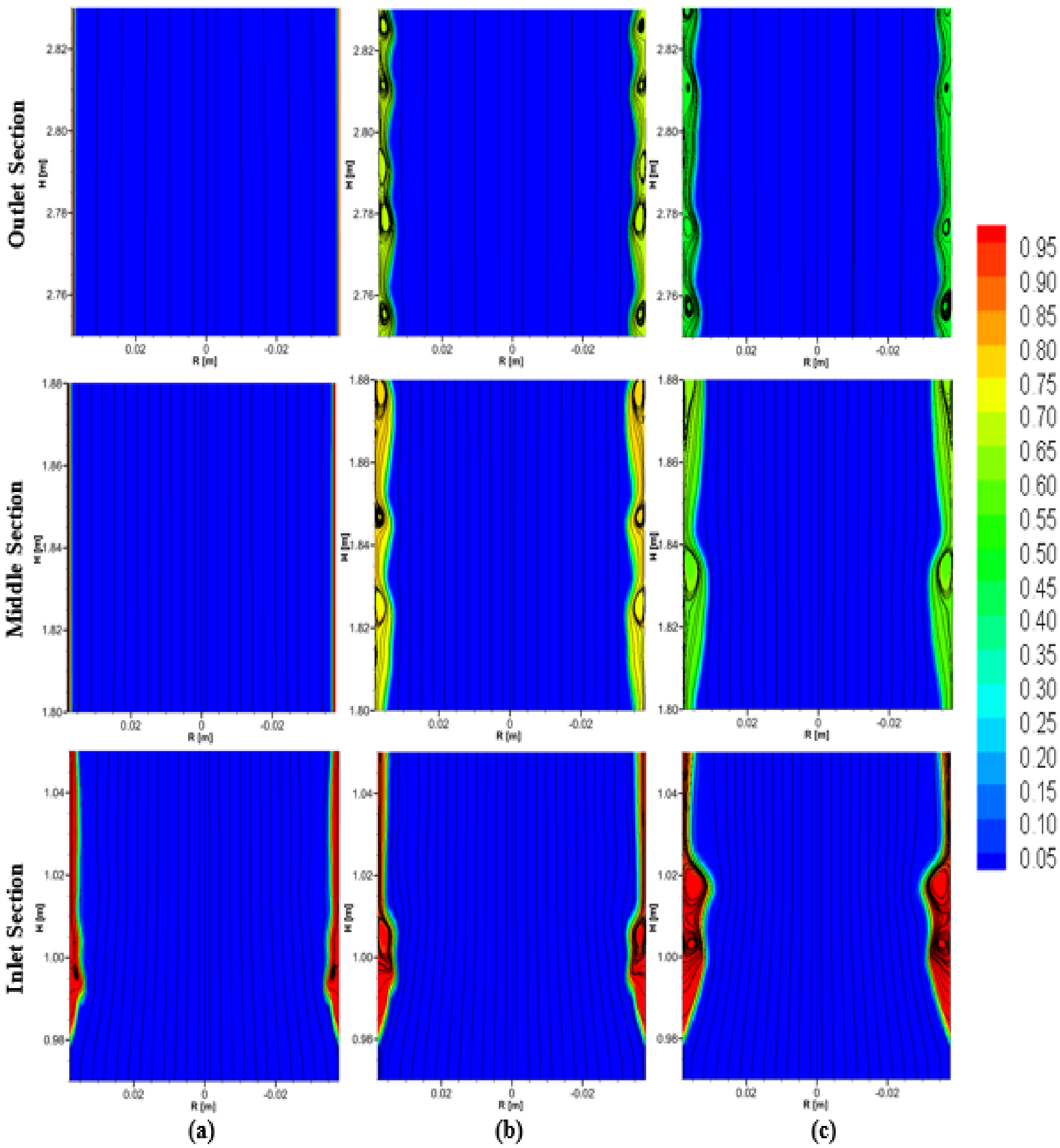

Figure 4.9: Stream traces for the case of $U_{SL} = 0.10$ m/s and varying U_{SG}: a) case 4, b) case 5 and c) case 6

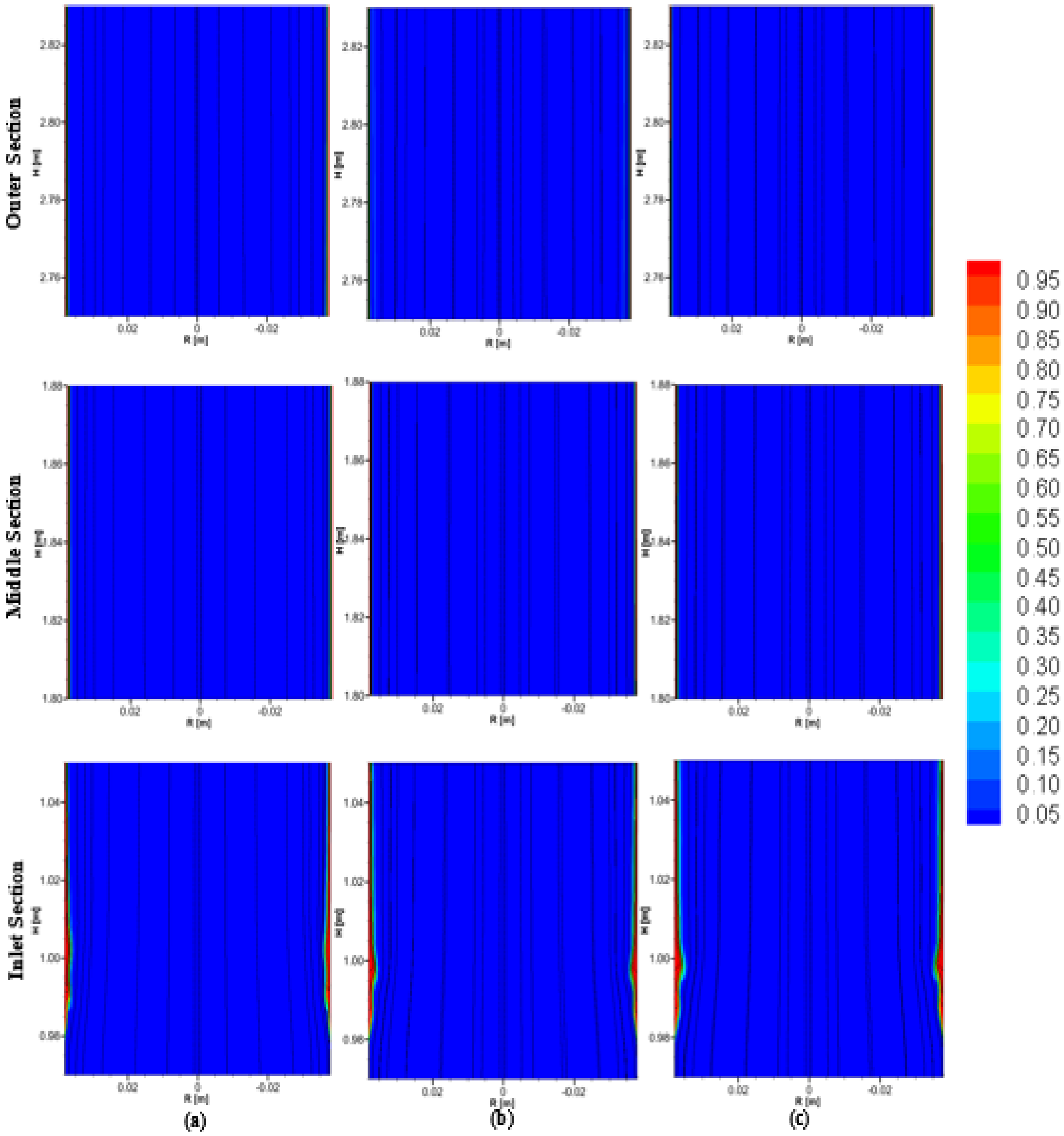

Figure 4.10: Stream traces for the case of $U_{SL} = 0.05$ m/s and varying U_{SG}: a) case 1, b) case 2 and c) case 3

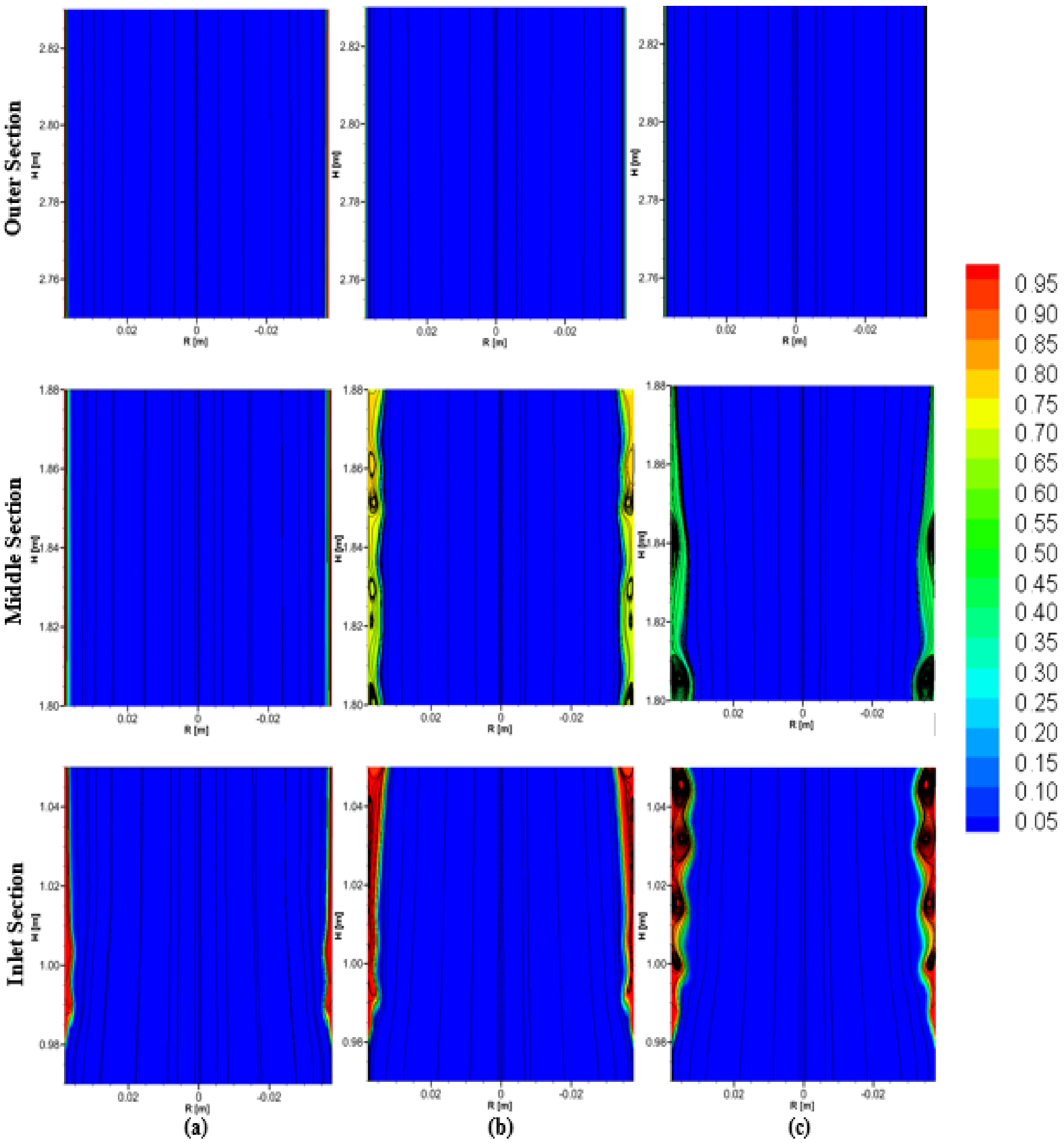

Figure 4.11: Stream traces for the case of $U_{SL} = 0.05$ m/s and varying U_{SG}: a) case 4, b) case 5 and c) case 6

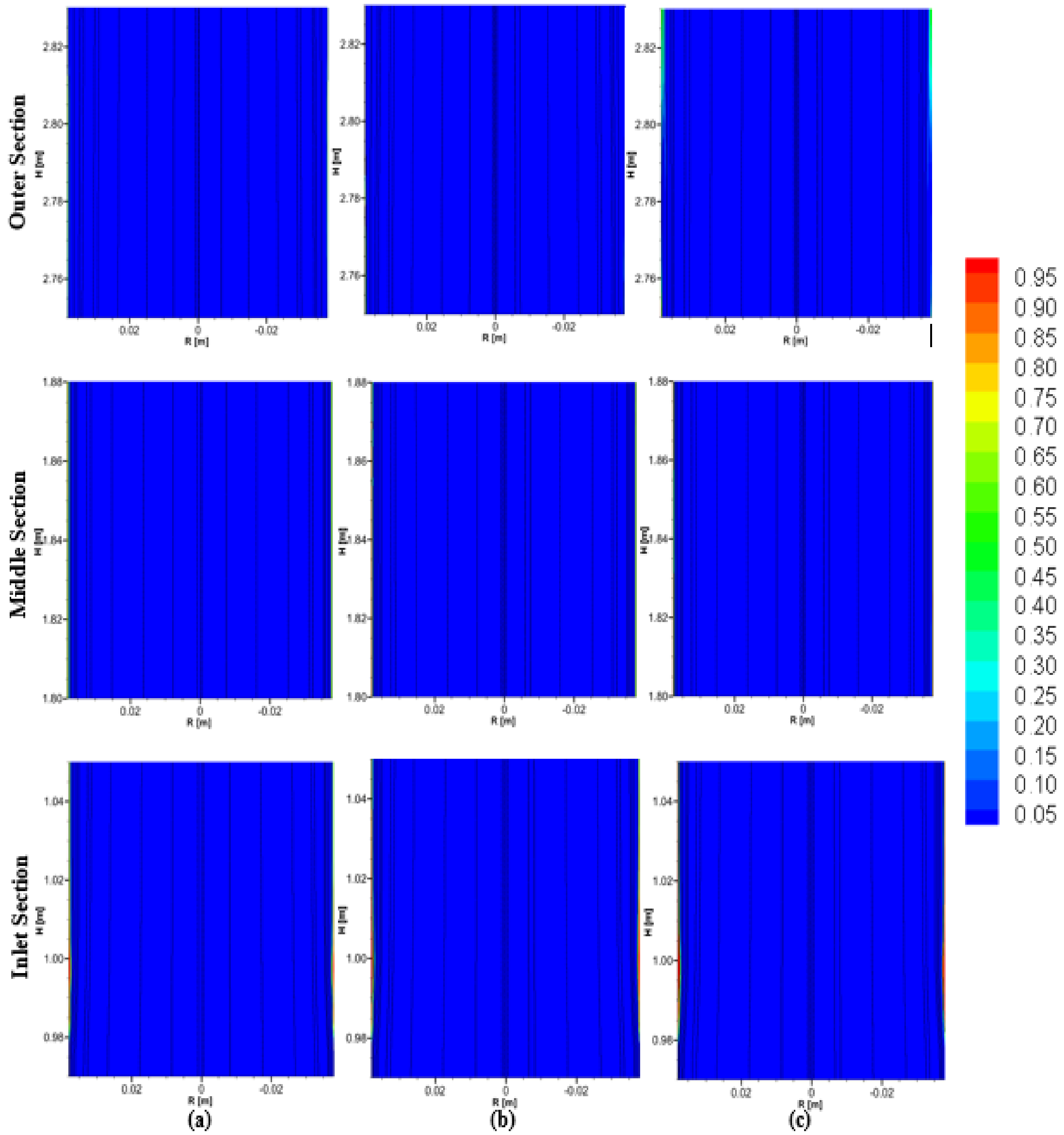

Figure 4.12: Stream traces for the case of $U_{SL} = 0.01$ m/s and varying U_{SG}: a) case 1, b) case 2 and c) case 3

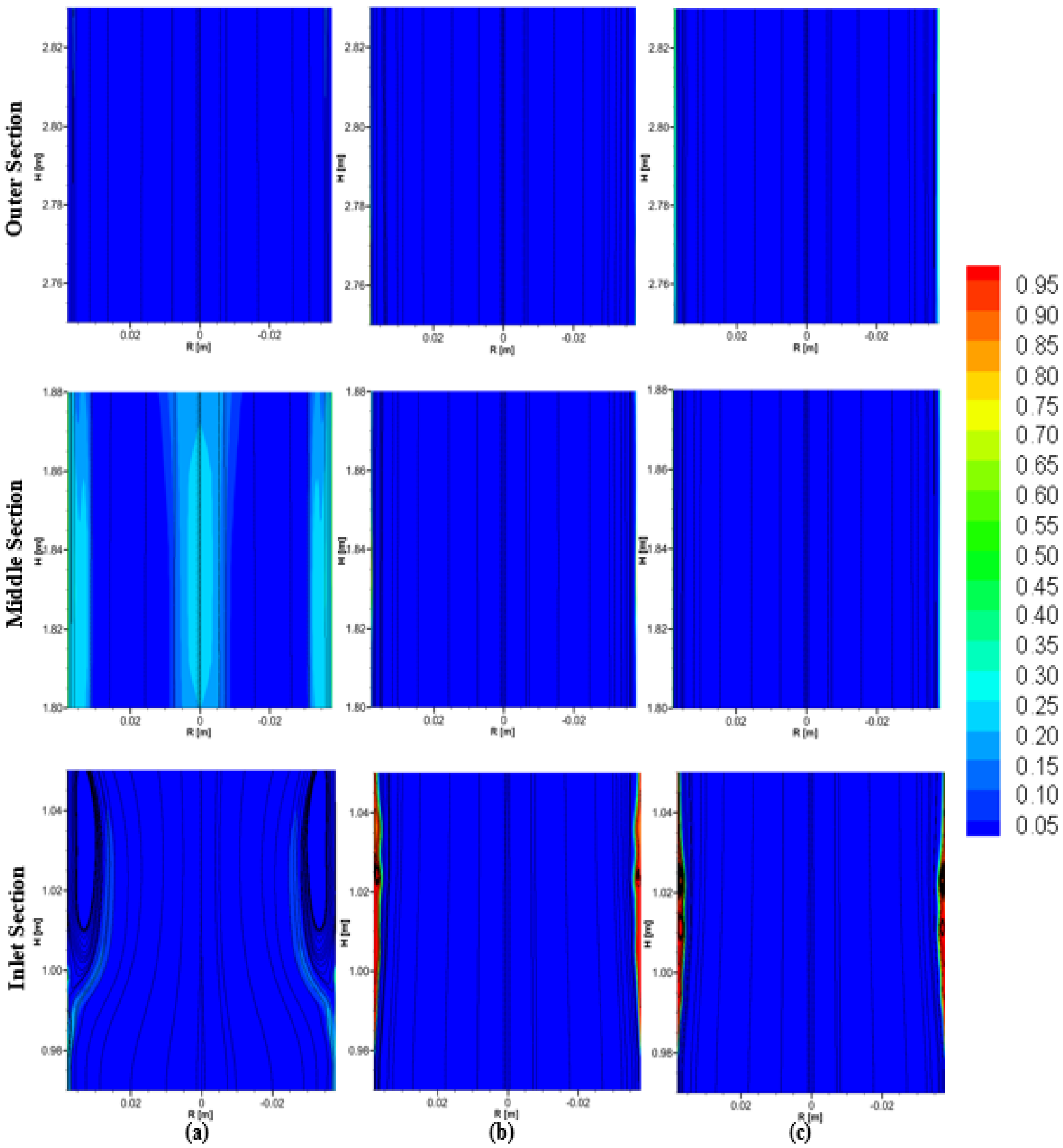

Figure 4.13: Stream traces for the case of $U_{SL} = 0.01$ m/s and varying U_{SG}: a) case 4, b) case 5 and c) case 6

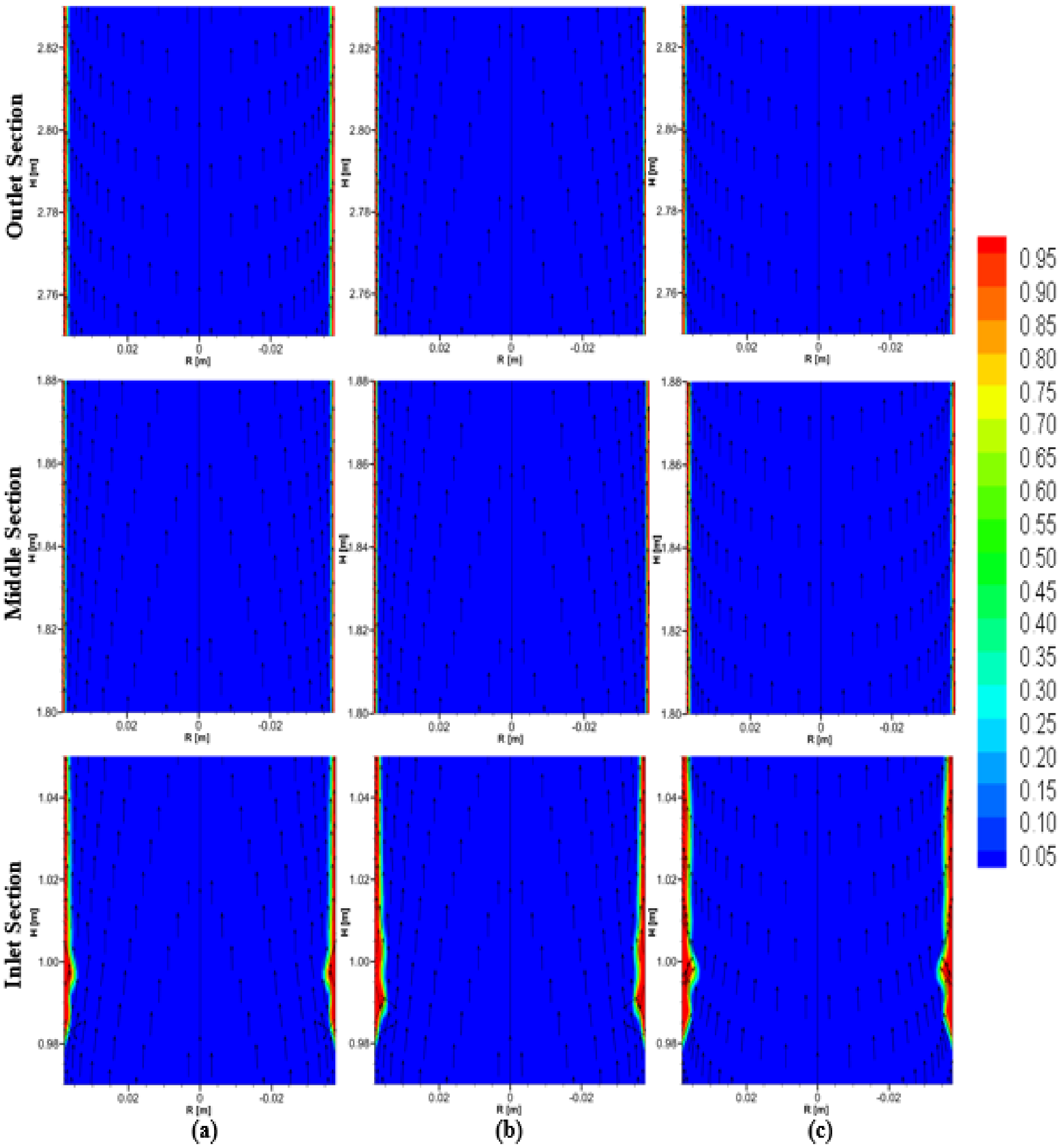

Figure 4.14: Velocity vectors for the case of $U_{SL} = 0.10$ m/s and varying U_{SG}: a) case 1, b) case 2 and c) case 3

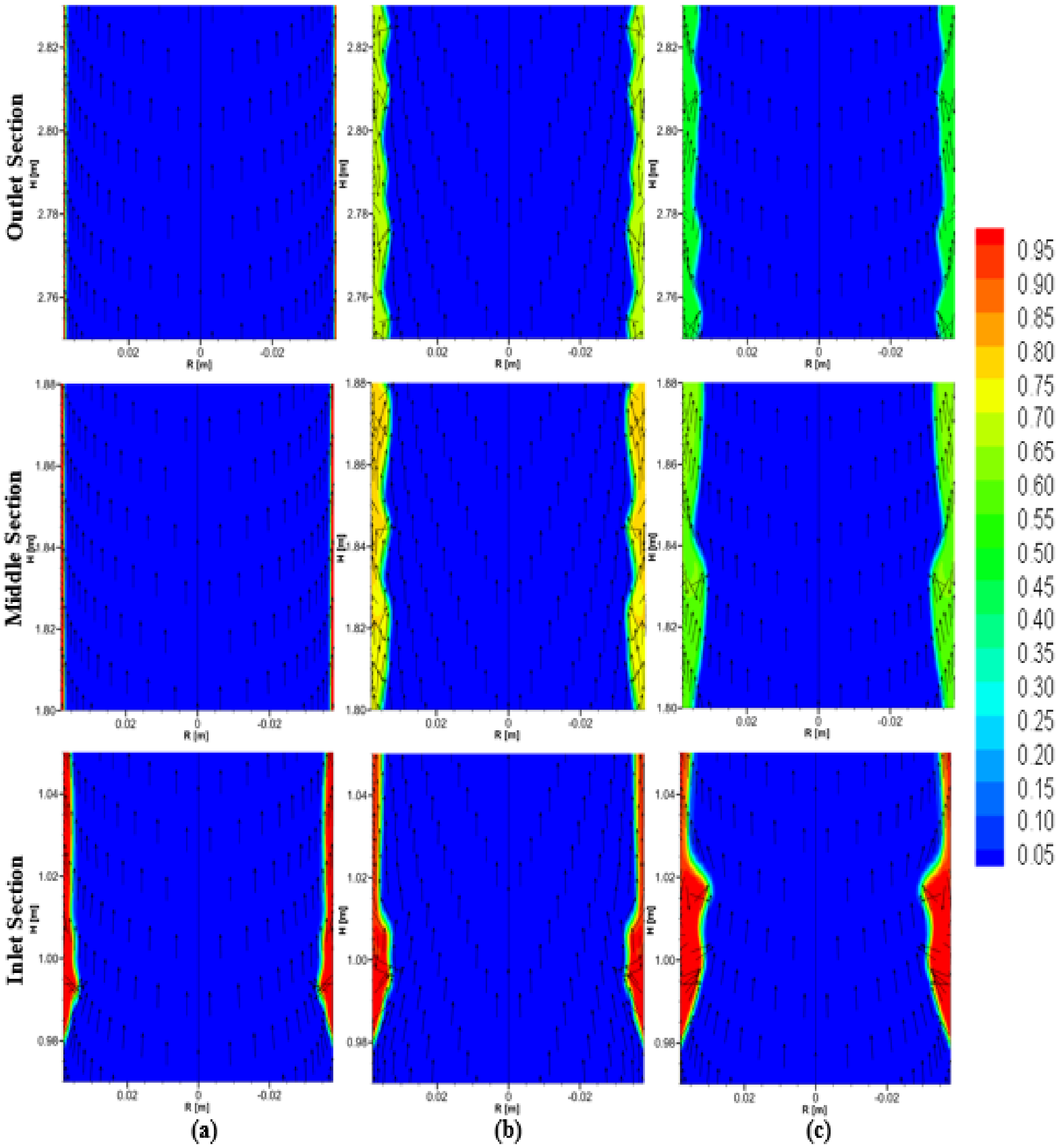

Figure 4.15: Velocity vectors for the case of $U_{SL} = 0.10$ m/s and varying U_{SG}: a) case 4, b) case 5 and c) case 6

4.7 Liquid Film Thickness

After conducting a sensitivity of liquid film thickness using liquid volume fractions of 0.3, 0.5 and 0.7 as the interface between the two fluids, Vieiro[11] showed that using a liquid volume fraction of 0.5 can provide a good approximation for the measurement of the liquid film thickness. This approach has been adopted by other researchers[51][92] where the estimation of the liquid film thickness gave good agreement with experimental results. In order to estimate the liquid film thickness for the current study, a similar approach was utilized. The film thickness is computed as the average value between $H = 2.5$ m and $H = 2.8$ m and the results presented in Figure 4.16. The estimated liquid film thicknesses (δ) were compared with that of the experimental data using equation (4.1) which was obtained by modifying that of Guner[17] for vertical pipes.

$$\delta = \frac{1}{2}\left(D - \sqrt{\frac{\left(1 - H_L\right) D^2}{\alpha_c}}\right) \tag{4.1}$$

where D is the pipe diameter; H_L is the liquid holdup; and α_c is the gas core void fraction which is given by equation (4.2).

$$\alpha_c = \frac{U_{SG}}{U_{SG} + f_E U_{SL}} \tag{4.2}$$

where f_E is the liquid entrainment fraction, which can be estimated using correlations from literature. In this study, f_E was estimated using the correlation developed by Guner[17].

Figure 4.16 shows that the liquid film thickness increases with decreasing superficial gas velocity for the three superficial liquid velocities as seen in the current model result and that of the experiment. There are however some discrepancies between the current model values and the experimental data as the superficial gas velocity reduces. This can be due to the way the liquid was introduced into the channel (lateral injection) as stated in section 4.4.

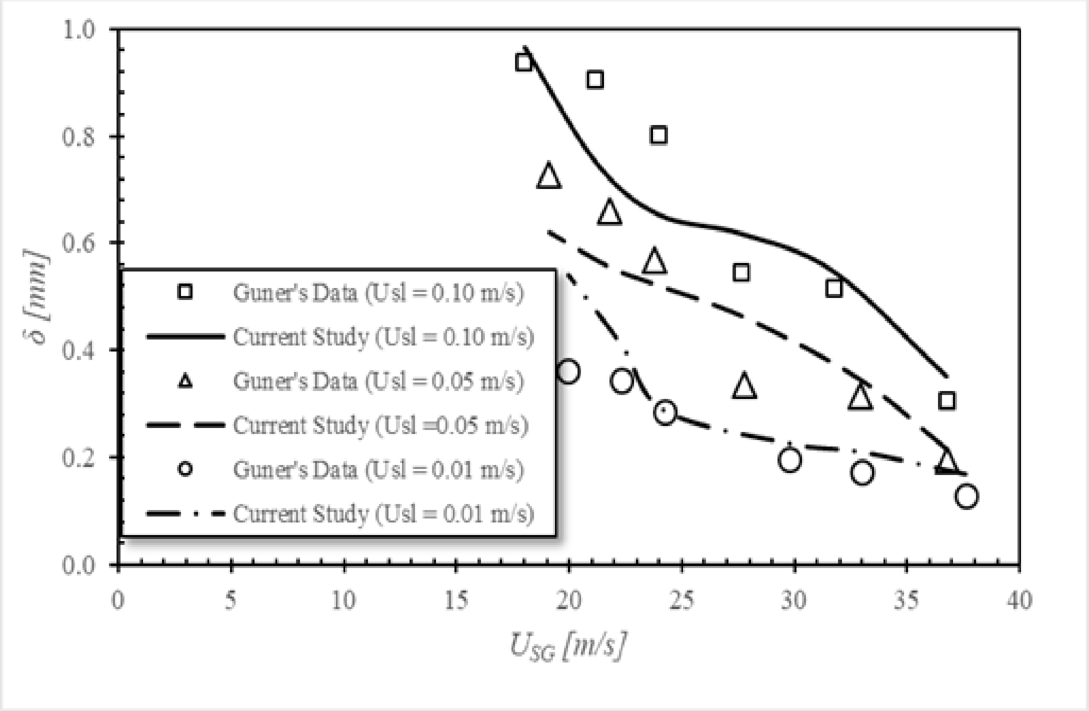

Figure 4.16: Variation of liquid film thickness with superficial gas velocity and comparison with experimental data by Guner[17]

4.8 Velocity Profiles and Liquid Volume Fractions

The axial gas and liquid velocity profiles for various cases are simulated and presented in this section. Shown in Figure 4.17 to 4.22 are the pipe outlet axial gas and liquid velocity profiles for the three different superficial liquid velocities (0.10 m/s, 0.05 m/s and 0.01 m/s).

In these figures, the radial distance of the pipe is represented by the horizontal axes and the pipe wall is represented by the rightmost point while the origin corresponds to the pipe axis. It can be seen that for a given input superficial liquid velocity, as the inlet gas superficial velocity decreases, the axial velocities (both gas and liquid) also decrease. Since the diameter of the droplets of the liquid phase is assumed to be very small, there is virtually no slip between the entrained droplets and the gas phase in the core region. Hence, the velocity profiles of both phases are almost the same in the gas core region as shown in Figure 4.17 to 4.22. The axial velocity distribution is highly affected by the phase distribution. It can be seen that the local gas velocity at the center of the pipe is higher than the input gas velocity. This is the due to the constriction of the area the pipe formed by the liquid phase. Hence, three zones can also be observed in the axial velocity distribution; (1) the gas core zone with the highest velocities, (2) the transition zone with slightly lower velocities (waves and liquid droplets) and (3) the liquid film velocity distribution with least velocities (no-slip at the pipe wall).

As described in section 4.6, the phase distribution has a great impact on the axial velocity distribution. The maximum values of the axial velocity are located in the region near the pipe axis and the lower values in the vicinity of the pipe wall. The phase distribution (liquid volume fraction) shown in Figure 4.23 presents two regions in the flow domain. The region with the highest liquid volume fraction (near the pipe wall) and the region with approximately zero liquid volume fraction (gas core section). The same liquid volume fraction profiles were observed in all the simulated cases.

In all the velocity profiles, two unique zones were observed. The first zone is located near the pipe wall with comparatively high liquid volume fraction and the second one occupies the core region close to the pipe centerline with approximately zero liquid volume fraction. Figure 4.24 shows the liquid phase axial velocity profile and the liquid volume fraction at the pipe outlet section for U_{SG} = 23.77 m/s at U_{SL} = 0.05 m/s. In the region where the liquid volume fraction is approximately zero, the axial velocity profile presents a feature of a typical turbulent flow in pipes whereas, in the vicinity of the pipe wall, velocity reduces dramatically. A similar feature was observed in the work of Vieiro *et al.*[11].

Figure 4.25 shows a detailed view of the near-wall behavior of the velocity profile and the liquid volume fraction for the case of U_{SG} = 23.77 m/s and U_{SL} = 0.05 m/ s . In this view, all the three zones described in section 4.6 can be observed.

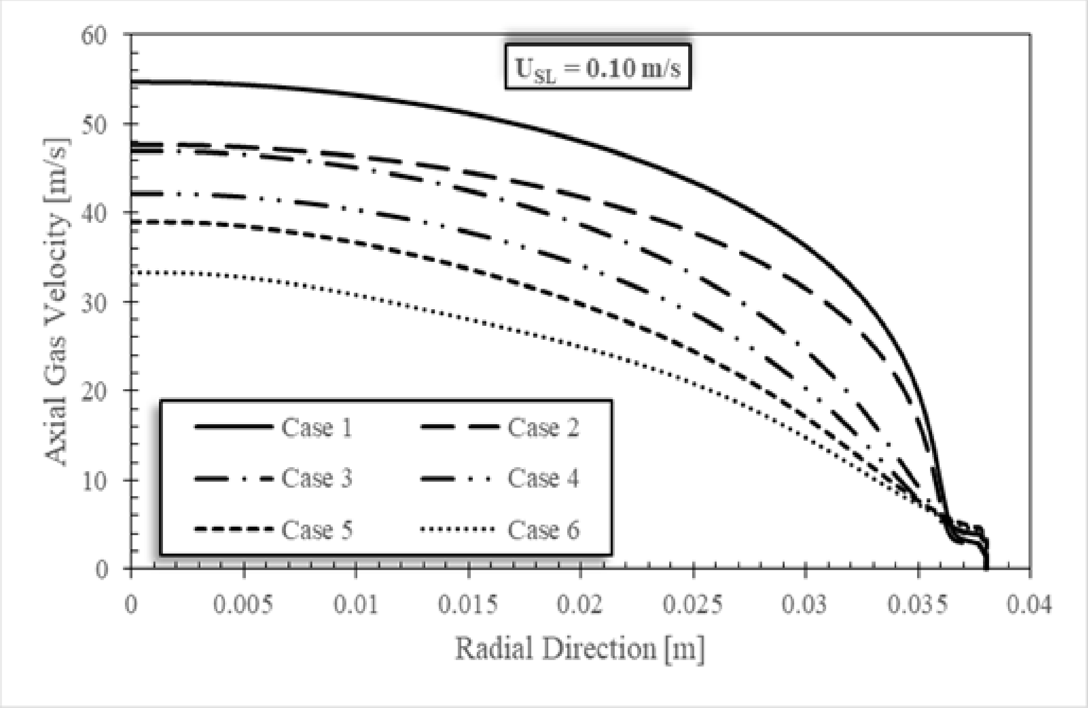

Figure 4.17: Pipe outlet gas phase velocity distribution for $U_{SL} = 0.10$ m/s and varying U_{SG}

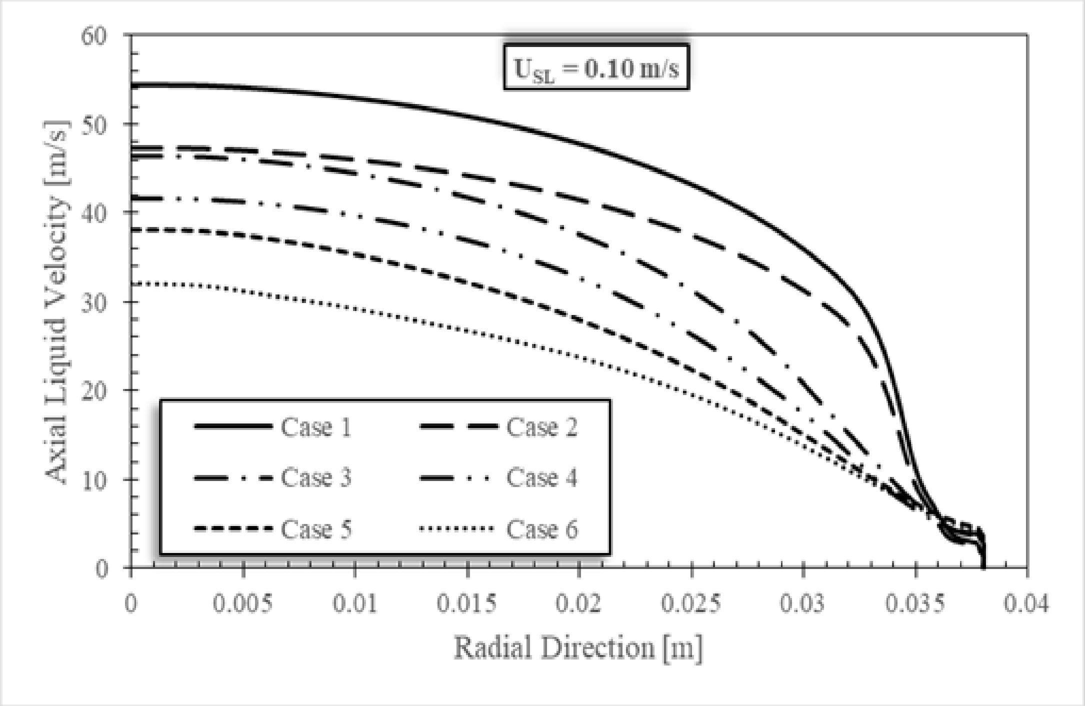

Figure 4.18: Pipe outlet liquid phase velocity distribution for $U_{SL} = 0.10$ m/s and varying U_{SG}

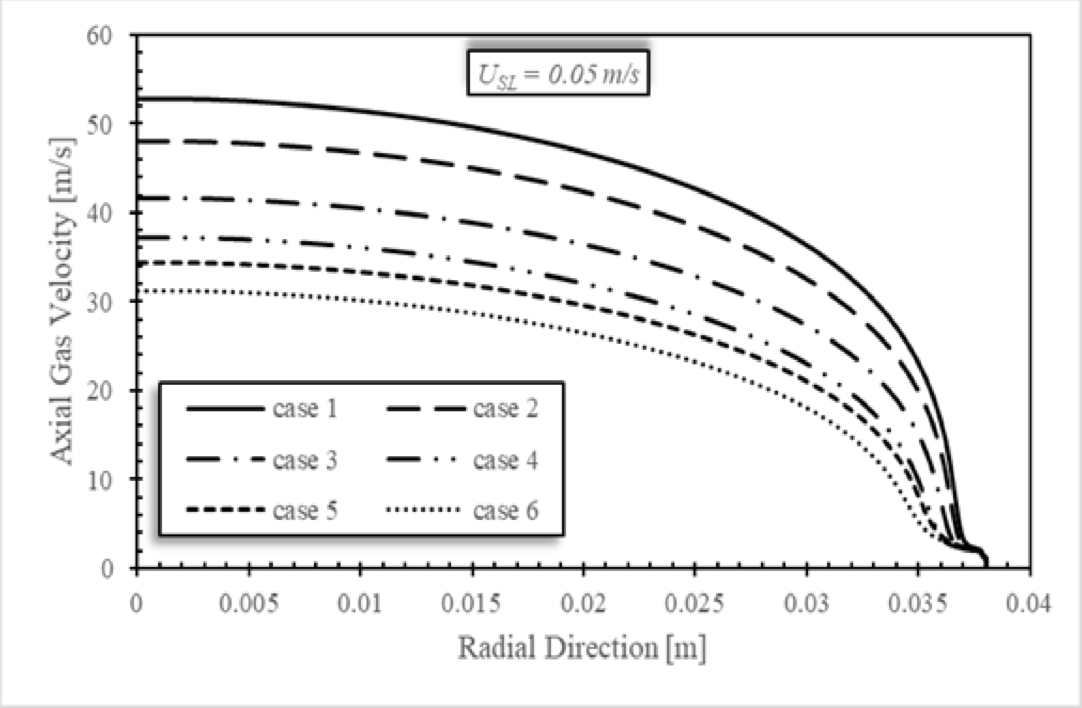

Figure 4.19: Pipe outlet gas phase velocity distribution for $U_{SL} = 0.05$ m/s and varying U_{SG}

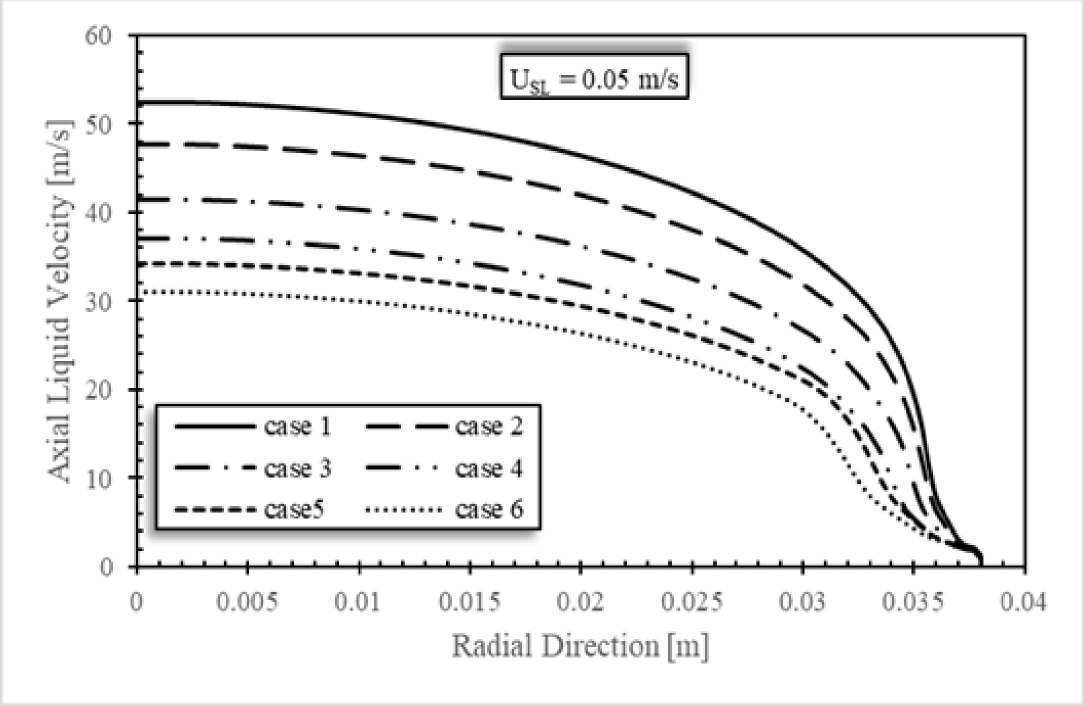

Figure 4.20: Pipe outlet liquid phase velocity distribution for $U_{SL} = 0.05$ m/s and varying U_{SG}

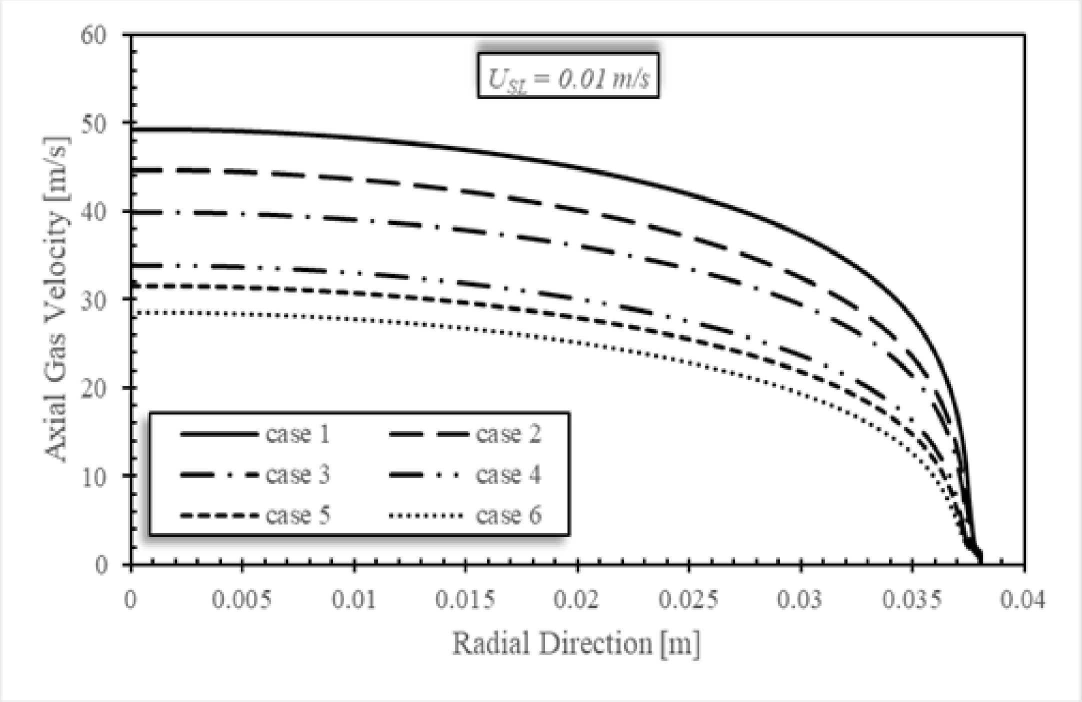

Figure 4.21: Pipe outlet gas phase velocity distribution for $U_{SL} = 0.01$ m/s and varying U_{SG}

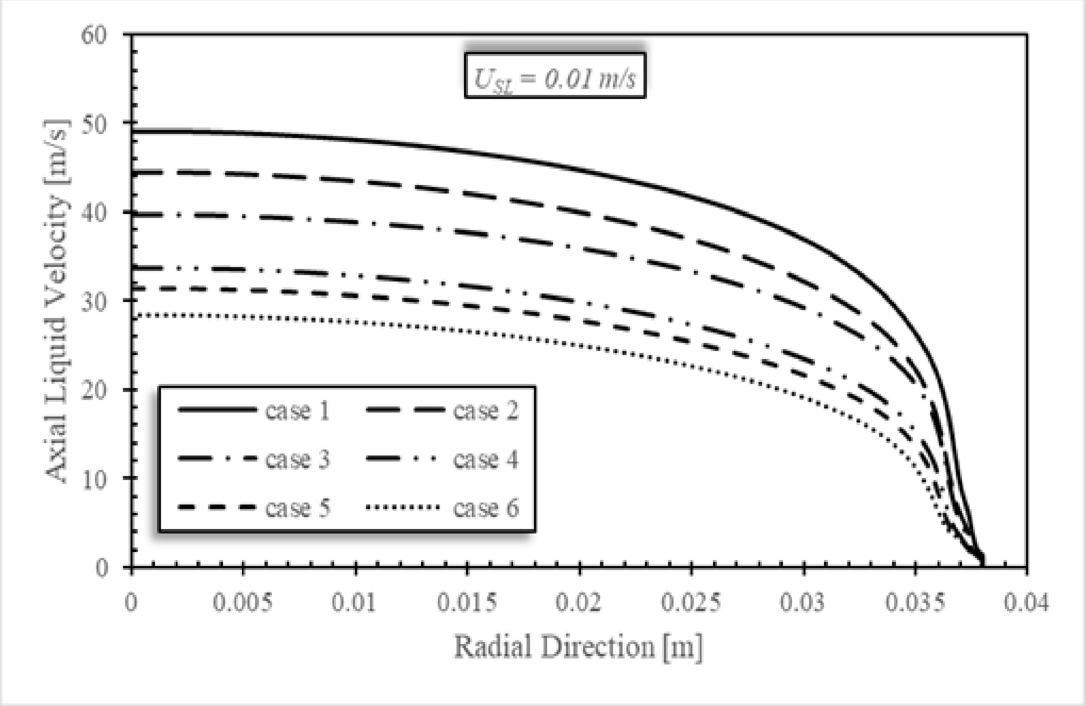

Figure 4.22: Pipe outlet liquid phase velocity distribution for $U_{SL} = 0.01$ m/s and varying U_{SG}

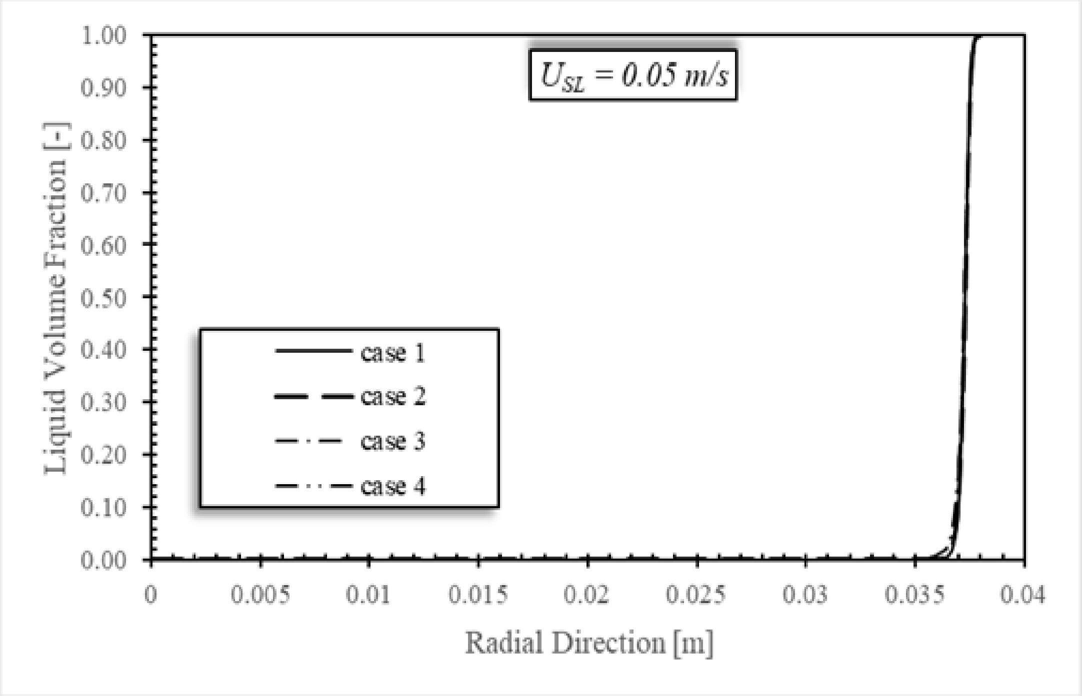

Figure 4.23: Pipe outlet liquid volume fraction distribution for $U_{SL} = 0.05$ m/s and varying U_{SG}

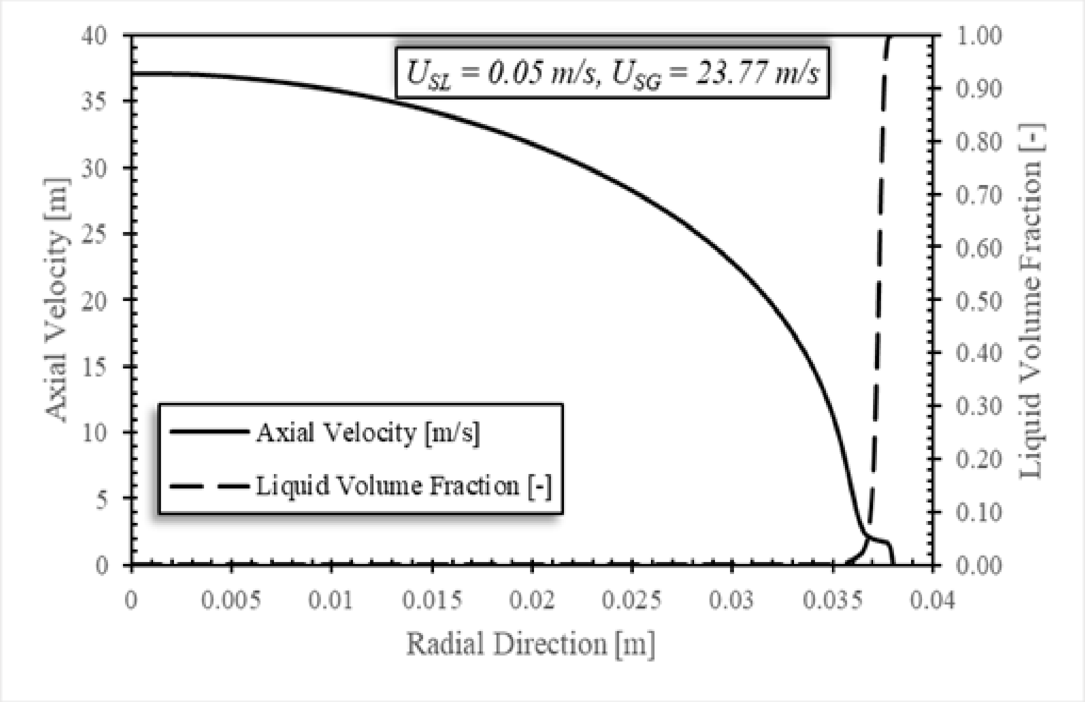

Figure 4.24: Axial velocity profile and volume fraction for the liquid phase for $U_{SL} = 0.05$ m/s and $U_{SG} = 0.23.77$ m/s

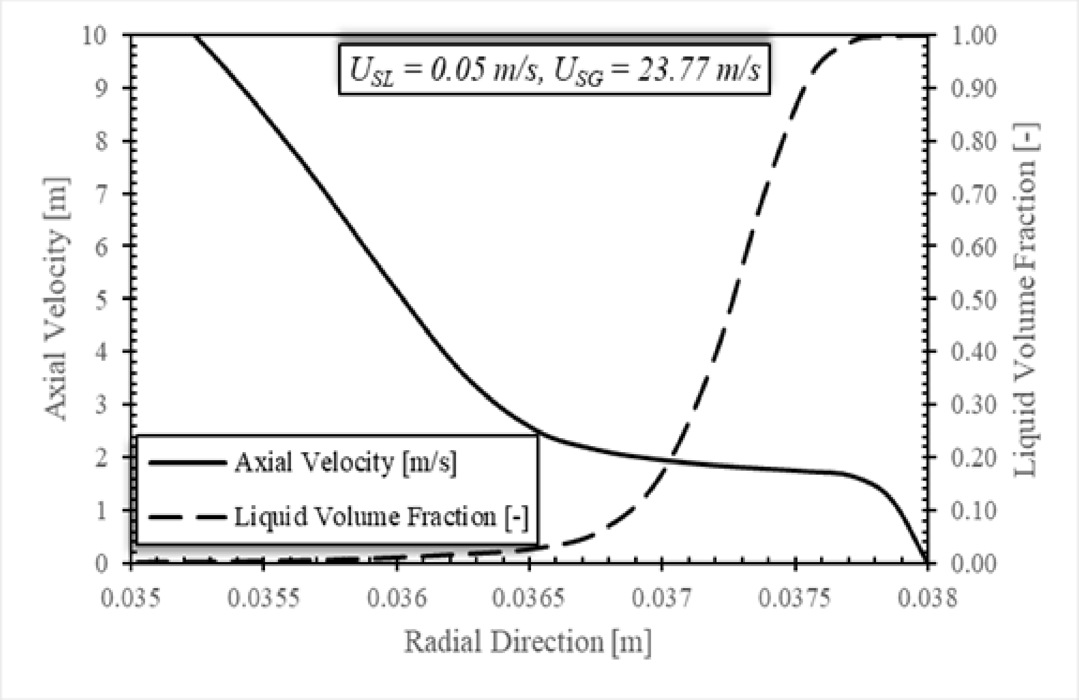

Figure 4.25: An expanded view of the near-wall behaviour

4.8.1 Slip Velocity

The slip velocity between the two phases seems to be negligible in the gas core where highest velocities are observed. However, in the liquid film section (waves and liquid droplets region) near the pipe wall, there is slip between the gas phase and liquid phase as observed in Figures 4.23, 4.24 and 4.25 for $U_{SL} = 0.10$ m/s, $U_{SL} = 0.05$ m/s and $U_{SL} = 0.01$ respectively. For a detailed view of the near-wall region where slip is significant see Figure 4.26 for the case of $U_{SG} = 32.92$ m/s and $U_{SL} = 0.05$ m/s.

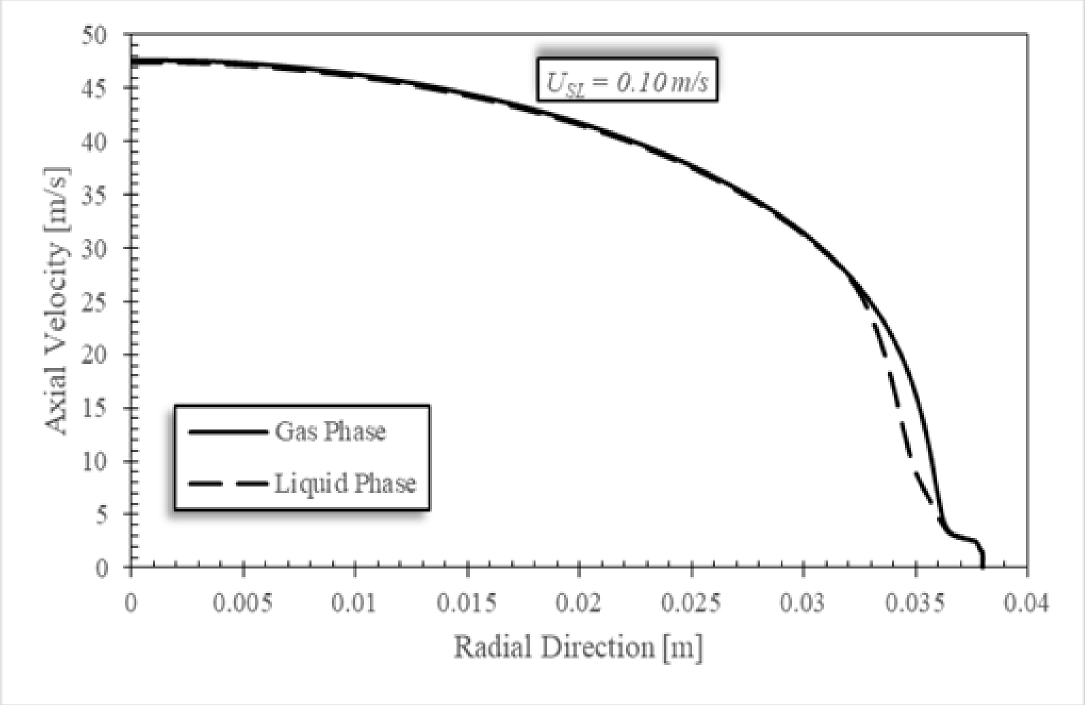

Figure 4.26: Slip velocity between the gas and liquid phases ($U_{SG} = 32.92$ m/s and $U_{SL} = 0.10$ m/s)

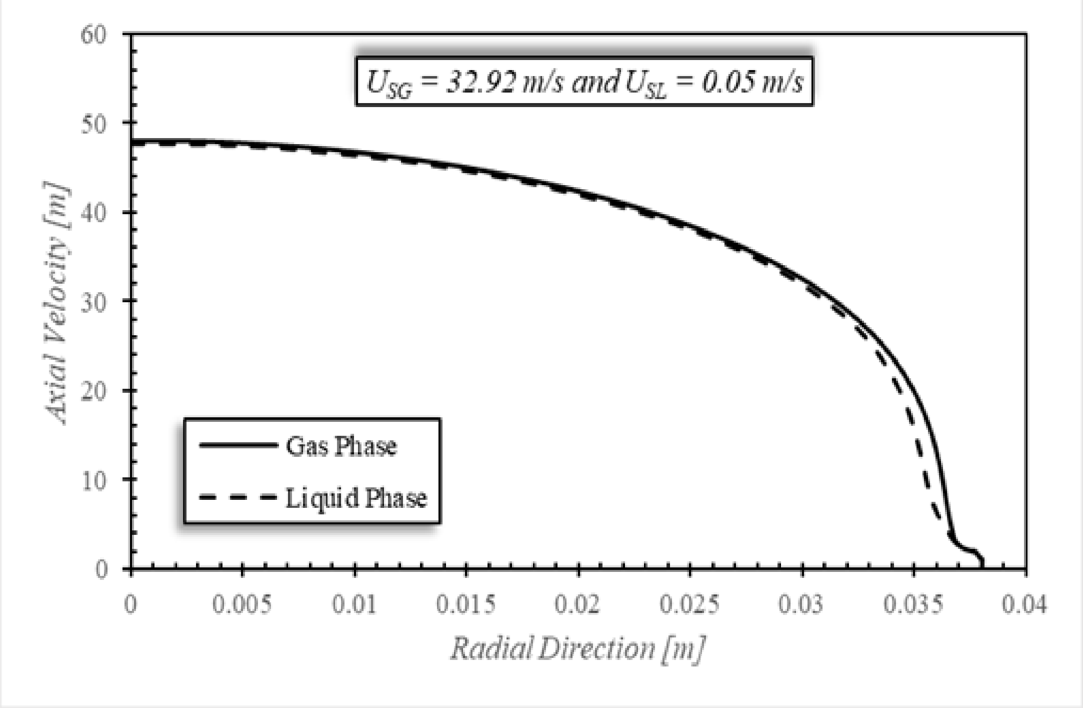

Figure 4.27: Slip velocity between the gas and liquid phases ($U_{SG} = 32.92$ m/s and $U_{SL} = 0.05$ m/s)

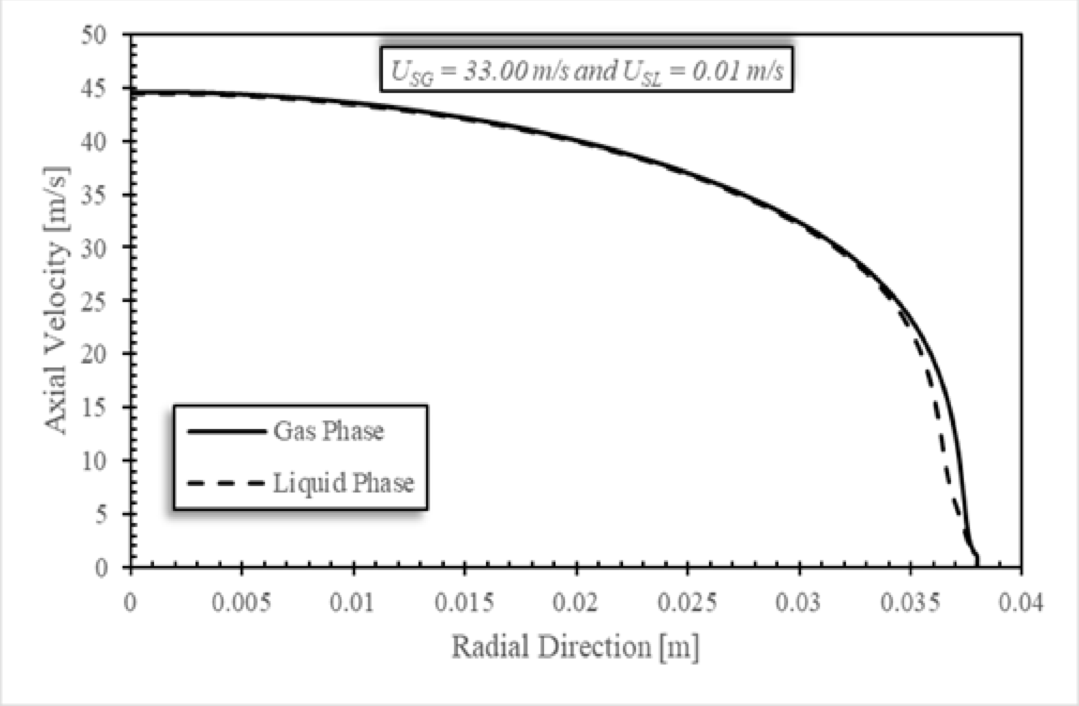

Figure 4.28: Slip velocity between the gas and liquid phases ($U_{SG} = 33.00$ m/s and $U_{SL} = 0.01$ m/s)

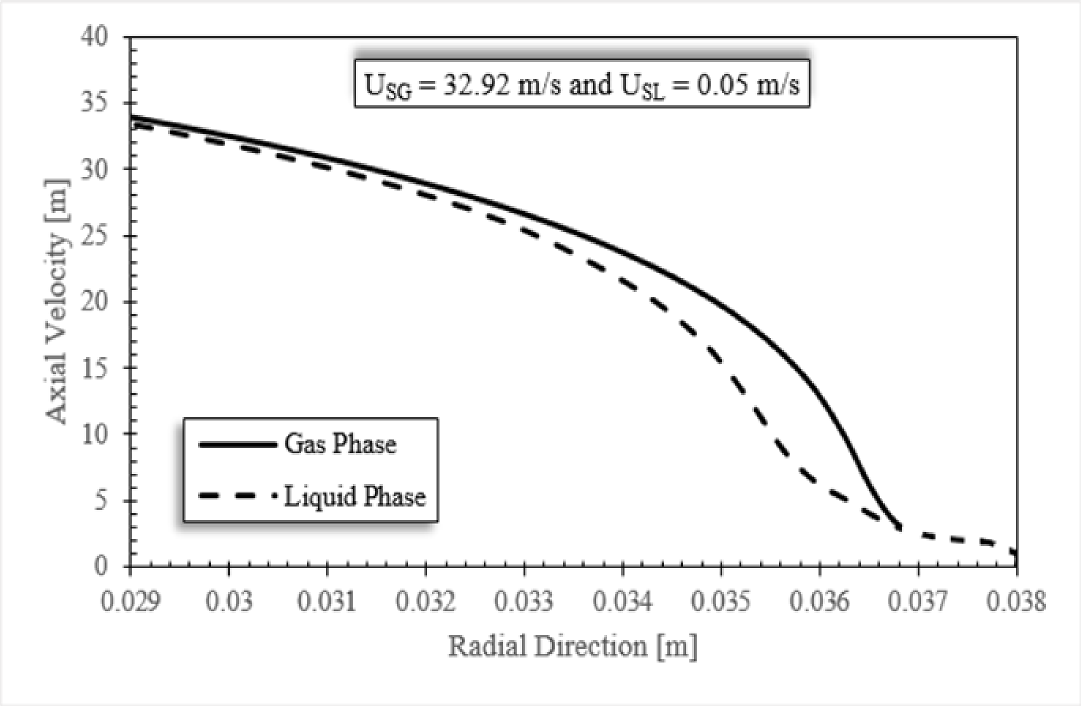

Figure 4.29: Detailed view of the slip near the liquid film section

4.9 Shear Stress Distribution

The radial variation of the shear stress at the pipe outlet section was computed and presented in Figures 4.30, 4.31 and 4.32 for the cases of $U_{SL} = 0.10$ m/s, $U_{SL} = 0.05$ m/s and $U_{SL} = 0.01$ m/s respectively. For all the cases simulated, the absolute shear stress is found to decrease radially towards the pipe axis. As the superficial gas velocity decreases (from case 1 to case 6), the absolute value of the shear stress also tends to decrease as well as the amplitude of the fluctuations.

Figure 4.33 shows both flow velocity and shear stress distributions presented for case 1 ($U_{SG} = 36.77$ m/s and $U_{SL} = 0.05$ m/s). In the region close to the pipe wall (where the liquid film dominates) with comparatively low velocities, the absolute shear stress fluctuates with the maximum value found in the vicinity of the pipe wall and decreases linearly to zero towards the pipe axis. An expanded detailed view of the shear stress is provided in Figure 4.34 for the case of $U_{SL} = 0.05$ m/s with varying superficial gas velocities. From Figure 4.34, it can be seen that for all the cases, the maximum amplitude of the wall shear stress occurs close to the wall. This could be due to the presence of the viscous sublayer where high velocity gradients are usually encountered. Further away from the pipe wall, the fluctuations could be due to turbulence but with decreasing amplitudes. The mass transfer at the interface (entrainment and deposition of liquid droplets) may also affect the shear stress and its space and time variations.

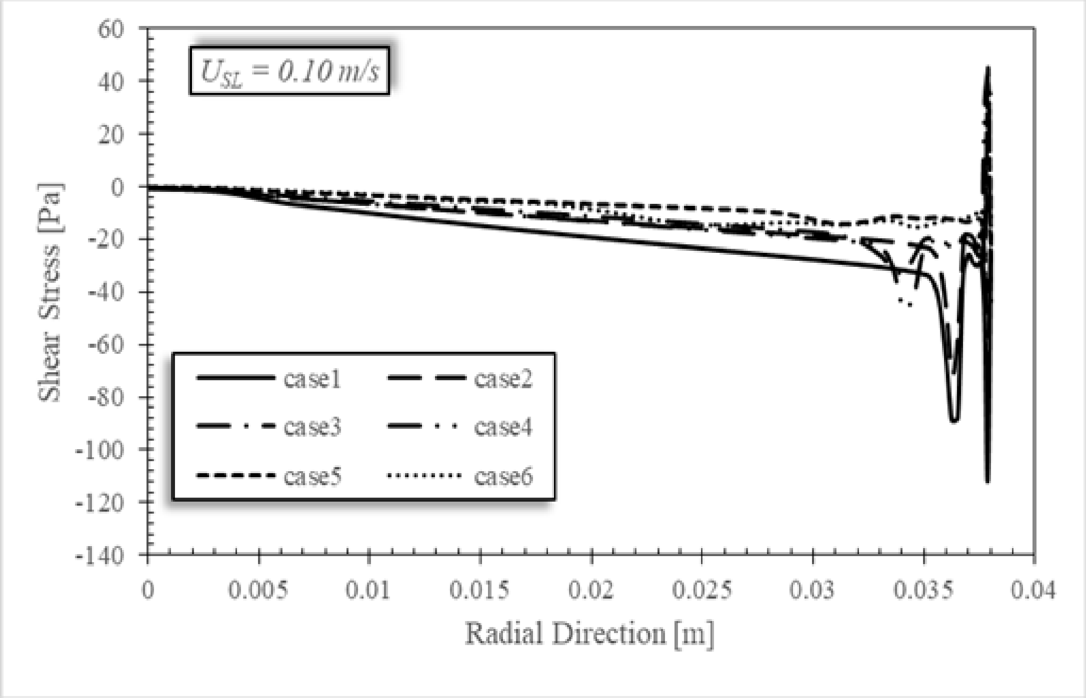

Figure 4.30: Shear stress distribution for $U_{SL} = 0.10$ m/s and varying U_{SG}

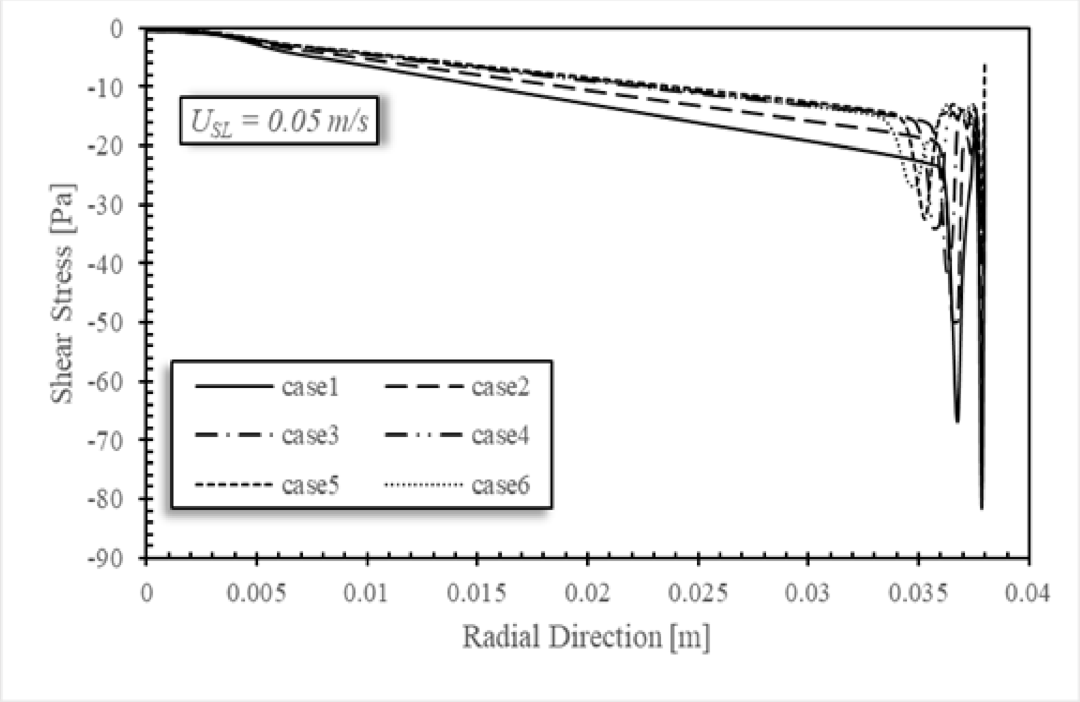

Figure 4.31: Shear stress distribution for $U_{SL} = 0.05$ m/s and varying U_{SG}

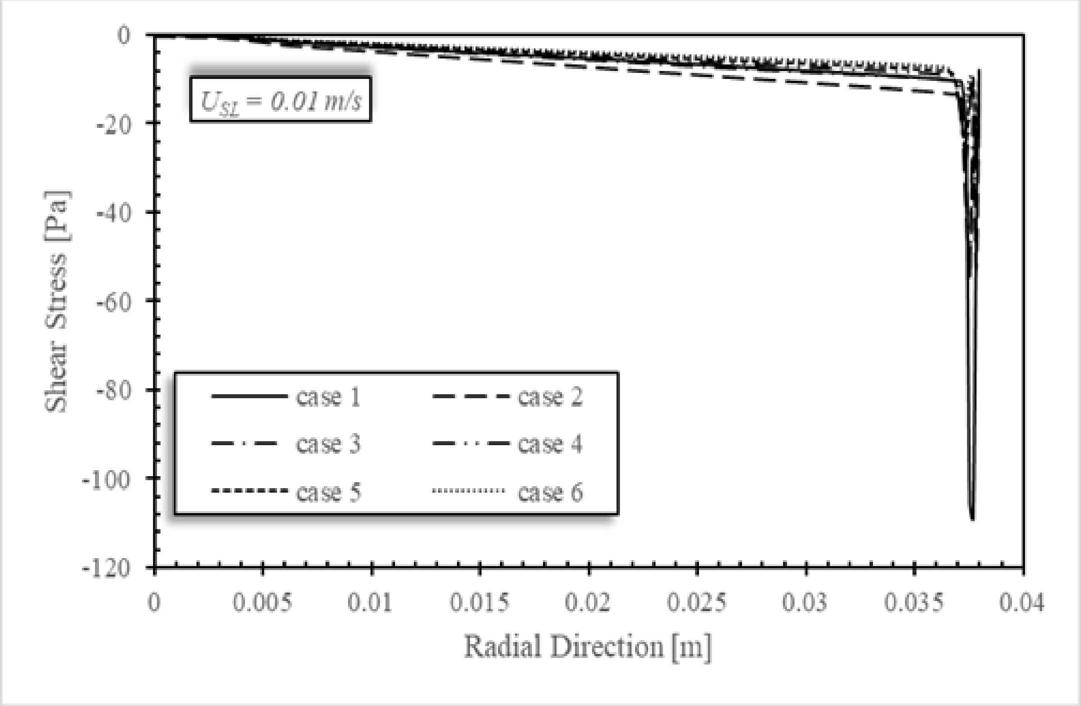

Figure 4.32: Shear stress distribution for $U_{SL} = 0.05$ m/s and varying U_{SG}

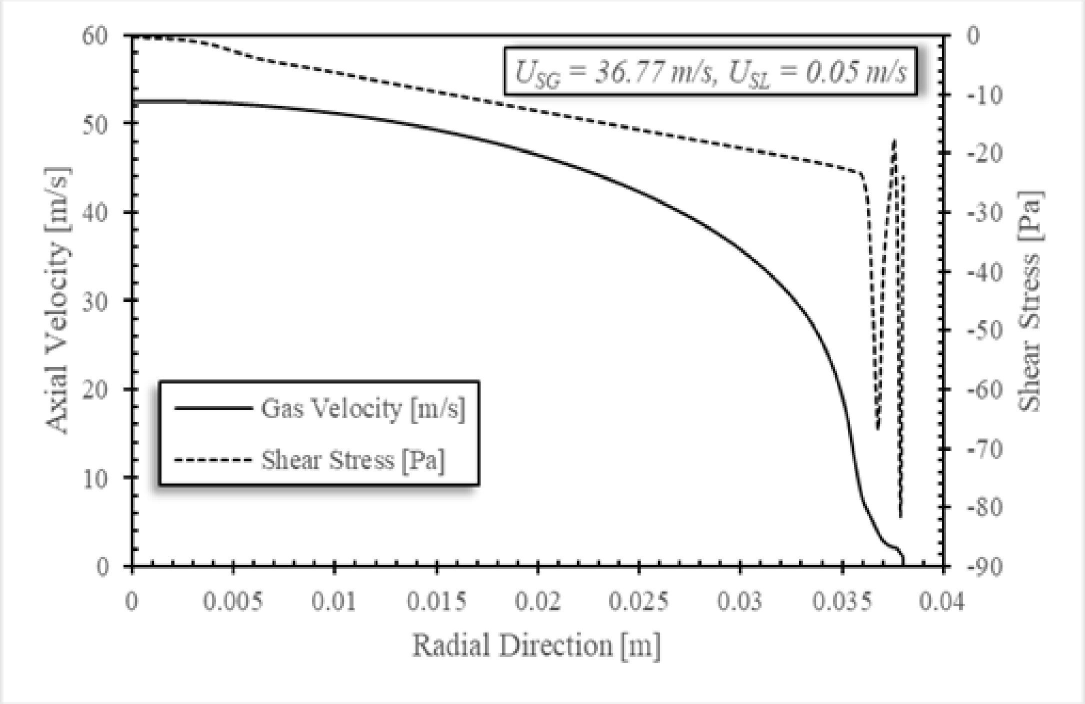

Figure 4.33: Axial gas velocity with shear stress variation for $U_{SG} = 36.77$ m/s and $U_{SL} = 0.05$ m/s

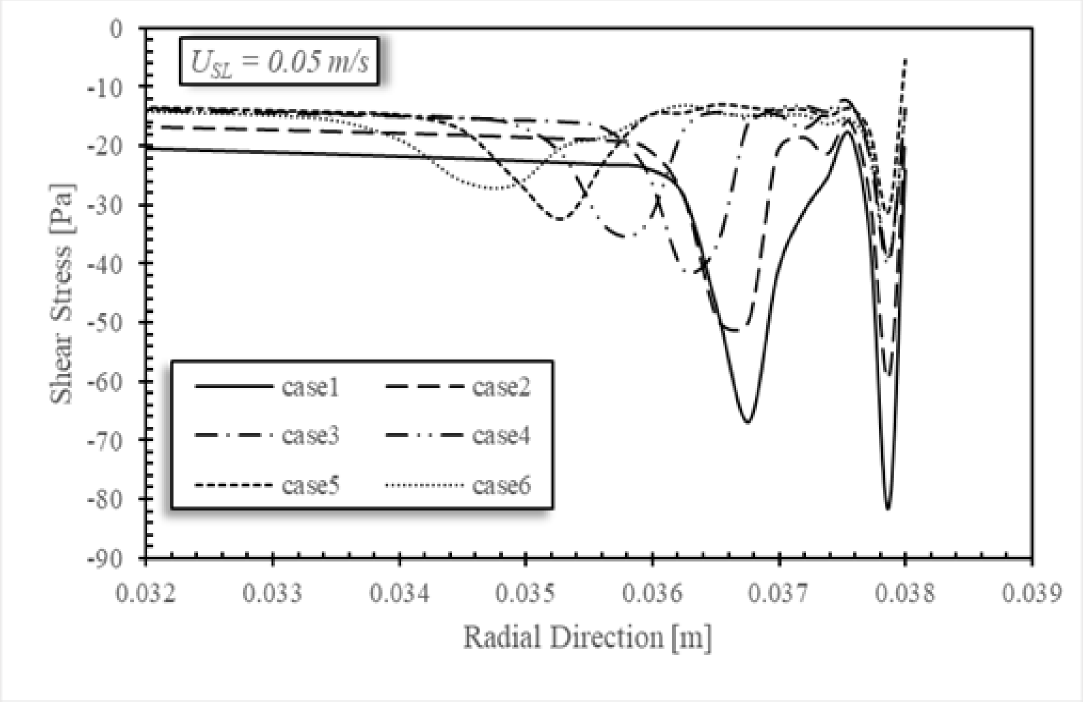

Figure 4.34: Near-wall behaviour of the shear stress

4.9.1 Variation of Wall Shear Stress with Superficial Gas Velocity

The variation of the average wall shear stress with the superficial gas velocity is plotted in Figure 4.35. The figure shows a decrease in the average wall shear stress with the decrease in the superficial gas velocity. Also for reducing superficial liquid velocity, the wall shear stress is again seen to be decreasing (for all the three superficial liquid velocities). For onset of complete film reversal, the wall shear stress must be approximately zero or change sign[3].

However, in this study, no such observation was made and since the focus is to predict the onset of film reversal, physically observing change in film flow direction through stream traces and phase distributions diagrams was adopted to estimate the critical velocity corresponding to film reversal as stated earlier. It was observed by Guner[17] that the wall shear stress never approaches zero and it behaves asymptotic towards zero. Hence, this criteria was not adopted in the present study.

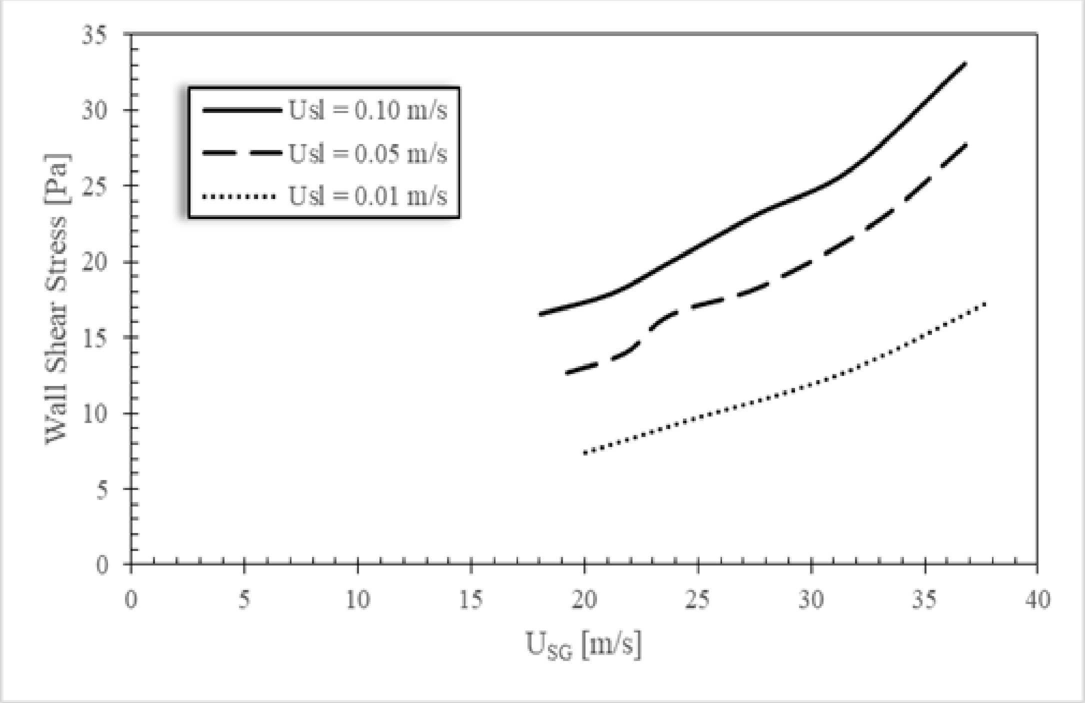

Figure 4.35: Wall shear stress variation with input superficial gas velocity

CHAPTER 5

CONCLUSIONS AND RECOMMENDATIONS

5.1 Conclusions

The current study presents numerical simulation of annular two-phase air-water flow in a vertical pipe of constant diameter for investigating the onset of film reversal. The study is performed using the Multi-Fluid VOF model available in ANSYS Fluent® commercial code. The geometry development was achieved using Gambit software. The models utilized for the current computations include; continuum surface force for the effects of surface tension, standard $k-\varepsilon$ turbulence model with enhanced wall treatment for turbulence effects, modified HRIC model for the interface tracking and the interfacial drag was modeled using Schiller and Naumann's model. The study adopts a 2D axisymmetric type domain where the liquid phase enters the vertical pipe laterally through the side of the pipe wall 1 m above the gas inlet. All the transport and conservations equations were discretized accurately using the finite-volume method and solutions were considered to be converged when all the residuals were less than 10^{-3} with mass imbalances less than 5%. Conclusions made from the study include:

- The numerical simulations satisfactorily captured the main characteristics of annular flow and churn flow regarding the formation of liquid film on the pipe wall, formation of roll waves, instabilities between the liquid film and the gas core.

- There was a satisfactory agreement between the numerical results and the experimental data regarding pressure gradient distributions and the critical superficial gas velocities corresponding to the onset of film reversal. In all of the three superficial liquid velocity simulations, the pressure gradient decreases with decreasing superficial gas velocity. A similar agreement is observed in the critical superficial gas velocity corresponding to the onset of film reversal.

- As the superficial gas velocity decreases, it is observed that there is intermittent up and down liquid film flow with large amplitude waves at the pipe wall. Thus, with decreasing superficial gas velocities for a given superficial liquid velocity, there is an increase in the formation of flooding waves which results in an increase in the liquid film thickness adherent to the pipe wall and becomes much more disturbed.

- Velocity profiles show that lower velocities are observed in the liquid film near the pipe wall while the maximum velocities are observed in the pipe center. Slip between the gas phase and liquid phase can be neglected in the regions close to the pipe axis. This is not the case for regions close to the liquid film near the pipe wall. There is significant slip between the phases around the wave and entrained droplet area close to the liquid film.

- Due to the presence of the viscous sublayer and the turbulent nature of the flow in its vicinity, the shear stress due to turbulence reaches its maximum in the near-wall region (due to Reynold stresses) and then decreases again towards the pipe center. The shear stress fluctuations in the liquid film occur as a result of the unsteadiness of the liquid-gas interface as well as the mass transfer during the liquid droplet entrainment and deposition.
- For a given superficial liquid velocity, the wall shear stress is seen to decrease with decreasing superficial gas velocities.

5.2 Recommendations

A 2D computational domain was utilized for the current study and as a result detailed information regarding the formation of roller waves was limited. It is therefore recommended that a 3D domain (by considering a sector of the pipe) be utilized. This would improve the visualization and understanding of the roller and disturbance wave formations of the flow phenomena.

In addition, it is recommended that the grid around the wave region be improved to be able to capture the droplet entrainment and deposition mechanisms. Also, utilizing the geo-reconstruction scheme for interface tracking can help achieve this purpose. However, utilizing this feature requires explicit time integration and limited to smaller time steps resulting in more computational time requirements.

REFERENCES

[1] C. E. Brennen, *Flow Patterns.* Cambridge University Press, 2005, pp. 127–154.

[2] A. Faghri and Y. Zhang, *Transport phenomena in multiphase systems.* Academic Press, 2006.

[3] G. Hewitt, *Annular two-phase flow.* Elsevier, 2013.

[4] J. M. Rodriguez, “Numerical simulation of two-phase annular flow,” Ph.D. dissertation, 2009. [Online]. Available: https://search.proquest.com/docview/304988102?accountid=27795

[5] J. M. C. Van't Westende, “Droplets in annular-dispersed gas-liquid pipe-flows,” 2008.

[6] G. F. Hewitt, C. J. Martin, and N. S. Wilkes, “Experimental and modelling studies of annular flow in the region between flow reversal and the pressure drop minimum,” *Physico-Chemical Hydrodynamics*, vol. 6, pp. 43–50, 1985.

[7] G. B. Wallis, “One-dimensional two-phase flow,” 1969.

[8] H.-Y. Park, G. Falcone, and C. Teodoriu, “Decision matrix for liquid loading in gas wells for cost/benefit analyses of lifting options,” *Journal of Natural Gas Science and Engineering*, vol. 1, no. 3, pp. 72–83, 2009.

[9] Y. Taitel, D. Bornea, and A. E. Dukler, “Modelling flow pattern transitions for steady upward gas-liquid flow in vertical tubes,” *AIChE Journal*, vol. 26, no. 3, pp. 345–354, 1980.

[10] G. B. Wallis, “The transition from flooding to upwards cocurrent annular flow in a vertical pipe,” United Kingdom Atomic Energy Authority, Tech. Rep., 1962.

[11] J. Vieiro, M. Asuaje, and G. Polanco, “Study of the two-phase liquid loading phenomenon by applying CFD techniques,” *The International Journal of Multiphysics*, vol. 7, no. 4, 2016.

[12] A. M. Ansari, N. D. Sylvester, O. Shoham, and J. P. Brill, “A comprehensive mechanistic model for upward two-phase flow in wellbores,” in *SPE Annual Technical Conference and Exhibition.* Society of Petroleum Engineers, 1990.

[13] O. Shoham, “Mechanistic modeling of gas-liquid two-phase flow in pipes,” 2006.

[14] J. R. Barbosa Jr, A. H. Govan, and G. F. Hewitt, “Visualisation and modelling studies of churn flow in a vertical pipe,” *International Journal of Multiphase Flow*, vol. 27, no. 12, pp. 2105–2127, 2001.

[15] E. Viana Pagan, “Modeling churn and annular flow regimes in vertical and near-vertical pipes with small and large diameters,” 2016.

[16] H. Han and K. Gabriel, “Flow physics of upward cocurrent gas-liquid annular flow in a vertical small diameter tube,” *Microgravity Science and Technology*, vol. 18, no. 2, pp. 27–38, 2006.

[17] M. Guner, “Liquid Loading of Gas Wells with Deviations from 0 to 45,” Master’s thesis, University of Tulsa, 2012.

[18] S. Jayanti and G. Hewitt, “Hydrodynamics and heat transfer in wavy annular gas-liquid flow: a computational fluid dynamics study,” *International Journal of Heat and Mass Transfer*, vol. 40, no. 10, pp. 2445–2460, 1997.

[19] H. Han, “A study of Entrainment in Two-Phase Upward Cocurrent Annular Flow in a Vertical Tube,” Ph.D. dissertation, University of Saskachewan, 2005.

[20] H. Han and K. Gabriel, “A numerical study of entrainment mechanism in axisymmetric annular gas-liquid flow,” *Journal of Fluids Engineering*, vol. 129, no. 3, pp. 293–301, 2007.

[21] Z. Zhu and K. Gabriel, “A Study of the interfacial features of gas-liquid annular two-phase flow,” *Master’s thesis, University of Saskatchewan, Saskatoon, Saskatchewan, Canada*, 2004.

[22] B. Kishore and S. Jayanti, “A multidimensional model for annular gas–liquid flow,” *Chemical Engineering Science*, vol. 59, no. 17, pp. 3577–3589, 2004.

[23] P. B. Whalley, “Boiling, condensation, and gas-liquid flow,” 1987.

[24] Y. Liu, W. Li, and S. Quan, “A self-standing two-fluid CFD model for vertical upward two-phase annular flow,” *Nuclear Engineering and Design*, vol. 241, no. 5, pp. 1636–1642, 2011.

[25] E. Da Riva and D. Del Col, “Numerical simulation of churn flow in a vertical pipe,” *Chemical Engineering Science*, vol. 64, no. 17, pp. 3753–3765, 2009.

[26] M. Parsi, M. Agrawal, V. Srinivasan, R. E. Vieira, C. F. Torres, B. S. McLaury, S. A. Shirazi, E. Schleicher, and U. Hampel, “Assessment of a hybrid CFD model for simulation of complex vertical upward gas–liquid churn flow,” *Chemical Engineering Research and Design*, vol. 105, pp. 71–84, 2016.

[27] V. Stevanovic and M. Studovic, “A simple model for vertical annular and horizontal stratified two-phase flows with liquid entrainment and phase transitions: one-dimensional steady state conditions,” *Nuclear Engineering and Design*, vol. 154, no. 3, pp. 357–379, 1995.

[28] V. Alipchenkov, R. Nigmatulin, S. Soloviev, O. Stonik, L. Zaichik, and Y. Zeigarnik, “A three-fluid model of two-phase dispersed-annular flow,” *International journal of heat and mass transfer*, vol. 47, no. 24, pp. 5323–5338, 2004.

[29] W. H. Henstock and T. J. Hanratty, “The interfacial drag and the height of the wall layer in annular flows,” *AIChE Journal*, vol. 22, no. 6, pp. 990–1000, 1976.

[30] J. Asali, T. t. Hanratty, and P. Andreussi, "Interfacial drag and film height for vertical annular flow," *AIChE Journal*, vol. 31, no. 6, pp. 895–902, 1985.

[31] W. Ambrosini, P. Andreussi, and B. Azzopardi, "A physically based correlation for drop size in annular flow," *International Journal of Multiphase Flow*, vol. 17, no. 4, pp. 497–507, 1991.

[32] N. Brauner and D. M. Maron, "The role of interfacial shear modelling in predicting the stability of stratified two-phase flow," *Chemical engineering science*, vol. 48, no. 16, pp. 2867–2879, 1993.

[33] T. Fukano and T. Furukawa, "Prediction of the effects of liquid viscosity on interfacial shear stress and frictional pressure drop in vertical upward gas–liquid annular flow," *International journal of multiphase flow*, vol. 24, no. 4, pp. 587–603, 1998.

[34] L. Fore, S. Beus, and R. Bauer, "Interfacial friction in gas–liquid annular flow: analogies to full and transition roughness," *International journal of multiphase flow*, vol. 26, no. 11, pp. 1755–1769, 2000.

[35] M. Ishii and K. Mishima, "Two-fluid model and hydrodynamic constitutive relations," *Nuclear Engineering and design*, vol. 82, no. 2-3, pp. 107–126, 1984.

[36] F. Dobran, "Hydrodynamic and heat transfer analysis of two-phase annular flow with a new liquid film model of turbulence," *International Journal of Heat and Mass Transfer*, vol. 26, no. 8, pp. 1159–1171, 1983.

[37] R. Kumar and D. P. Edwards, “Interfacial shear modeling in two-phase annular flow,” Knolls Atomic Power Lab., Schenectady, NY (United States), Tech. Rep., 1996.

[38] P. Kosky, “Thin liquid films under simultaneous shear and gravity forces,” *International Journal of Heat and Mass Transfer*, vol. 14, no. 8, pp. 1220–1224, 1971.

[39] R. G. Turner, M. G. Hubbard, and A. E. Dukler, “Analysis and prediction of minimum flow rate for the continuous removal of liquids from gas wells,” *Journal of Petroleum Technology*, vol. 21, no. 11, pp. 1–475, 1969.

[40] A. E. Dukler, *Fluid mechanics and heat transfer in falling film systems*, 1959.

[41] G. F. Hewitt, “Analysis of annular two-phase flow: Application of the Dukler analysis to vertical upward flow in a tube,” United Kingdom Atomic Energy Authority. Research Group. Atomic Energy Research Establishment, Harwell, Berks, England, Tech. Rep., 1961.

[42] S. B. Coleman, H. B. Clay, D. G. McCurdy, and L. H. Norris III, “A new look at predicting gas-well load-up,” *Journal of Petroleum Technology*, vol. 43, no. 03, pp. 329–333, 1991.

[43] M. A. Nosseir, T. A. Darwich, M. H. Sayyouh, and M. El Sallaly, “A new approach for accurate prediction of loading in gas wells under different flowing conditions,” in *SPE Production Operations Symposium.* Society of Petroleum Engineers, 1997.

[44] M. Li, S. Lei, and S. Li, "New view on continuous-removal liquids from gas wells," in *SPE Permian Basin Oil and Gas Recovery Conference.* Society of Petroleum Engineers, 2001.

[45] X.-H. Tan, X.-P. Li, and J.-Y. Liu, "Model of continuous liquid removal from gas wells by droplet diameter estimation," *Journal of Natural Gas Science and Engineering*, vol. 15, pp. 8–13, 2013.

[46] G. Zabaras, A. E. Dukler, and D. Moalem-Maron, "Vertical upward cocurrent gas-liquid annular flow," *AIChE journal*, vol. 32, no. 5, pp. 829–843, 1986.

[47] R. Belt, "On the liquid film in inclined annular flow," Ph.D. dissertation, TU Delft, Delft University of Technology, 2007.

[48] G. Yuan, "Liquid loading of gas wells," Ph.D. dissertation, University of Tulsa, 2011.

[49] N. Dousi, C. A. Veeken, and P. K. Currie, "Numerical and Analytical Modelling of the Gas Well Liquid Loading Process," *SPE Production & Operations*, vol. 21, no. 04, pp. 475–482, 2006.

[50] *ANSYS Fluent (version 16.1) user guide: multiphase flows*, ANSYS, 2012.

[51] J. Chen, Y. Tang, W. Zhang, Y. Wang, L. Qiu, and X. Zhang, "Computational fluid dynamic simulations on liquid film behaviors at flooding in an inclined pipe," *Chinese Journal of Chemical Engineering*, vol. 23, no. 9, pp. 1460–1468, 2015.

[52] M. Parsi, R. E. Vieira, C. F. Torres, N. R. Kesana, B. S. McLaury, S. A. Shirazi, E. Schleicher, and U. Hampel, “On the effect of liquid viscosity on interfacial structures within churn flow: experimental study using wire mesh sensor,” *Chemical Engineering Science*, vol. 130, pp. 221–238, 2015.

[53] L. Schiller and Z. Naumann, “Z,” *Ver. Deutsch. Ing*, vol. 77, p. 318, 1935.

[54] S. Morsi and A. Alexander, “An investigation of particle trajectories in two-phase flow systems,” *Journal of Fluid Mechanics*, vol. 55, no. 2, pp. 193–208, 1972.

[55] R. Clift, J. R. Grace, and M. E. Weber, *Bubbles, drops, and particles.* Courier Corporation, 2005.

[56] T. Takamasa and A. Tomiyama, “Three-dimensional gas–liquid two-phase bubbly flow in a C-shaped tube,” in *Proceedings of the 1999 NURETH-9 Conference*, 1999, pp. 1–17.

[57] M. Ishii, “Two-fluid model for two-phase flow,” *Multiphase science and technology*, vol. 5, no. 1-4, 1990.

[58] F. M. White and I. Corfield, *Viscous fluid flow.* McGraw-Hill Higher Education Boston, 2006, vol. 3.

[59] H. Karami, C. F. Torres, M. Parsi, E. Pereyra, and C. Sarica, “CFD Simulations of Low Liquid Loading Multiphase Flow in Horizontal Pipelines,” in *ASME 2014 4th Joint US-European Fluids Engineering Division Summer*

Meeting collocated with the ASME 2014 12th International Conference on Nanochannels, Microchannels, and Minichannels. American Society of Mechanical Engineers, 2014, pp. V002T06A011–V002T06A011.

[60] B. Launder and D. Spalding, "Lectures in mathematical models of turbulence," 1972.

[61] T.-H. Shin, W. W. Liou, A. Shabbir, Z. Yang, and J. Zhu, "A new $k - \varepsilon$ eddy viscosity model for high reynolds number turbulent flows," *Computers & Fluids*, vol. 24, no. 3, pp. 227–238, 1995.

[62] S.-E. Kim, D. Choudhury, and B. Patel, "Computations of complex turbulent flows using the commercial code FLUENT," in *Modeling complex turbulent flows.* Springer, 1999, pp. 259–276.

[63] V. Yakhot and S. A. Orszag, "Renormalization-group analysis of turbulence," *Physical review letters*, vol. 57, no. 14, p. 1722, 1986.

[64] D. Choudhury, *Introduction to the renormalization group method and turbulence modeling.* Fluent incorporated, 1993.

[65] J. U. Brackbill, D. B. Kothe, and C. Zemach, "A continuum method for modeling surface tension," *Journal of computational physics*, vol. 100, no. 2, pp. 335–354, 1992.

[66] S. B. Pope, "Turbulent flows," 2001.

[67] F. Chen and H. Hagen, "A survey of interface tracking methods in multi-phase fluid visualization," in *OASIcs-OpenAccess Series in Informatics*, vol. 19. Schloss Dagstuhl-Leibniz-Zentrum fuer Informatik, 2011.

[68] S. Osher and J. A. Sethian, "Fronts propagating with curvature-dependent speed: algorithms based on Hamilton-Jacobi formulations," *Journal of computational physics*, vol. 79, no. 1, pp. 12–49, 1988.

[69] C. W. Hirt and B. D. Nichols, "Volume of fluid (VOF) method for the dynamics of free boundaries," *Journal of computational physics*, vol. 39, no. 1, pp. 201–225, 1981.

[70] S. O. Unverdi and G. Tryggvason, "A front-tracking method for viscous, incompressible, multi-fluid flows," *Journal of computational physics*, vol. 100, no. 1, pp. 25–37, 1992.

[71] D. Lakehal, M. Meier, and M. Fulgosi, "Interface tracking towards the direct simulation of heat and mass transfer in multiphase flows," *International Journal of Heat and Fluid Flow*, vol. 23, no. 3, pp. 242–257, 2002.

[72] O. Gloth, D. Hänel, L. Tran, and R. Vilsmeier, "A front tracking method on unstructured grids," *Computers & fluids*, vol. 32, no. 4, pp. 547–570, 2003.

[73] H. Terashima and G. Tryggvason, "A front-tracking/ghost-fluid method for fluid interfaces in compressible flows," *Journal of Computational Physics*, vol. 228, no. 11, pp. 4012–4037, 2009.

[74] S. Osher and R. P. Fedkiw, "Level set methods: an overview and some recent results," *Journal of Computational physics*, vol. 169, no. 2, pp. 463–502, 2001.

[75] S. O. R. Fedkiw and S. Osher, "Level set methods and dynamic implicit surfaces," *Surfaces*, vol. 44, p. 77, 2002.

[76] J. A. Sethian and P. Smereka, "Level set methods for fluid interfaces," *Annual review of fluid mechanics*, vol. 35, no. 1, pp. 341–372, 2003.

[77] D. Enright, R. Fedkiw, J. Ferziger, and I. Mitchell, "A hybrid particle level set method for improved interface capturing," *Journal of Computational physics*, vol. 183, no. 1, pp. 83–116, 2002.

[78] M. Müller, "Fast and robust tracking of fluid surfaces," in *Proceedings of the 2009 ACM SIGGRAPH/Eurographics Symposium on Computer Animation.* ACM, 2009, pp. 237–245.

[79] R. V. Garimella, V. Dyadechko, B. K. Swartz, and M. J. Shashkov, "Interface reconstruction in multi-fluid, multi-phase flow simulations," in *Proceedings of the 14th international meshing roundtable.* Springer, 2005, pp. 19–32.

[80] M. Sussman and E. G. Puckett, "A coupled level set and volume-of-fluid method for computing 3D and axisymmetric incompressible two-phase flows," *Journal of computational physics*, vol. 162, no. 2, pp. 301–337, 2000.

[81] M. Marek, W. Aniszewski, and A. Boguslawski, "Simplified volume of fluid method for two-phase flows," *Task Quarterly*, vol. 3, no. 255-265, p. 41, 2008.

[82] W. F. Noh and P. Woodward, "SLIC (simple line interface calculation)," in *Proceedings of the Fifth International Conference on Numerical Methods in Fluid Dynamics June 28âĂŞJuly 2, 1976 Twente University, Enschede.* Springer, 1976, pp. 330–340.

[83] W. J. Rider and D. B. Kothe, "Reconstructing volume tracking," *Journal of computational physics*, vol. 141, no. 2, pp. 112–152, 1998.

[84] S. V. Patankar, "Numerical heat transfer and fluid flow,(1980)," *Hemisphere, New York*, pp. 25–73, 1980.

[85] J. M. Thomas and D. Trujillo, "Analysis of finite volume methods," *Mathematical Modelling of Flow Through Porous Media*, pp. 318–336, 1995.

[86] J. N. Reddy, *An introduction to the finite element method.* McGraw-Hill New York, 1993, vol. 2, no. 2.2.

[87] M. Kuron, "3 Criteria for Assessing CFD Convergence," 2015. [Online]. Available: http://www.engineering.com/DesignSoftware/DesignSoftwareArticles/ArticleID/9296/3-Criteria-for-Assessing-CFD-Convergence.aspx

[88] G. Besagni, G. Guédon, and F. Inzoli, "Experimental and numerical study of counter-current flow in a vertical pipe," *ASME Paper No. ESDA2014-20053*, 2014.

[89] P. Kabanda and M. Wang, "Numerical Simulation of Barite Sag in Pipe and Annular Flow," *Advances in Numerical Analysis*, vol. 2017, 2017.

[90] D. Barnea, “A unified model for predicting flow-pattern transitions for the whole range of pipe inclinations,” *International Journal of Multiphase Flow*, vol. 13, no. 1, pp. 1–12, 1987.

[91] A. H. Govan, G. F. Hewitt, H. J. Richter, and A. Scott, “Flooding and churn flow in vertical pipes,” *International journal of multiphase flow*, vol. 17, no. 1, pp. 27–44, 1991.

[92] L. Yan, Y. Wang, Z. Wu, Z. Dai, G. Yu, and F. Wang, “Research of vertical falling film behavior in scrubbing-cooling tube,” *Chemical Engineering Research and Design*, vol. 117, pp. 627–636, 2017.

Vitae

Name: Ernest Adaze

Nationality: Ghanaian

Date of Birth: 8th March, 1987

Email: *ernestadaze@yahoo.com*

Permanent Address: C/o P. O. Box 1156, Sunyani-B/A, Ghana-W/A

Academic Background: **Master of Science in Mechanical Engineering**,
King Fahd University of Petroleum and Minerals,
Dhahran, Kingdom of Saudi Arabia.

Bachelor of Science in Mechanical Engineering,
University of Mines and Technology,
Tarkwa, Ghana, West Africa.

Publications: A. L. Benson Lamidi, C. A. Dziwornu and **E. Adaze**. "Optimizing of Spacing of Horizontal Wells in Gas and Gas-Condensate Reservoirs." In *SPE Russian Petroleum Technology Conference*, pp. 1-10. 2015.

A. Simons, I. Owusu and **E. Adaze**. "Modification of the Gratis Firewood Dryer for Agricultural Produce." *Journal of the Ghana Institute of Engineers*, Vol. 10, 2013.

Fellowships/Awards:

Saudi Arabian Government Scholarship |2014-2017, King Fahd University of Petroleum and Minerals, Dhahran 31261, Saudi Arabia.

Best Graduating Mechanical Engineering Student | 2012, Department of Mechanical Engineering, University of Mines and Technology, Tarkwa, Western Region, Ghana.

Northern Ghana Scholarship | 2003-2006, Tamale Secondary School, Tamale, Northern Region, Ghana.

Best Pupil in Basic Education Certificate Examination | 2003, Junior Secondary School (Public Schools Category), The Methodist Church Ghana, Sunyani Diocese Educational Unit.

Professional Experience:

Vehicle Assessor (Consultant) | 2012-2014, Vanguard Assurance Company Limited, Tarkwa/Takoradi, Western Region, Ghana.

Duties:

1. Assessing the extent of damage of insured vehicles during accident
2. Estimating the exact cost of repair for accident vehicles
3. Preparing survey reports on the accident vehicles

Intern | June-August, 2011, Mantrac Ghana Limited, Tarkwa, Ghana.

Duties:

1. Joined a team of engineers who undertook contract maintenance work in several mining companies in Tarkwa and its neighbouring towns
2. Prepared service reports after every task performed

Pupil Teacher | 2006-2008, His Grace International School, Sunyani, Brong Ahafo Region, Ghana.

Duties:

1. Taught subjects like Mathematics, Natural Science, English and other subjects to grade six pupils